PHOTONIC CRYSTAL FIBER AS A ROBUST RAMAN SENSOR

ALTAF KHETANI

Thesis submitted to the
Faculty of Graduate and Postdoctoral Studies
in partial fulfillment of the requirements degree of
for the Doctorate in Philosophy degree in Electrical and Computer Engineering

School of Electrical Engineering and Computer Science
Faculty of Engineering
University of Ottawa

Abstract

This thesis focuses on the investigation and development of an integrated optical biosensor based on enhanced Raman techniques that will provide label-free detection of biomolecules. This is achieved by using hollow core photonic crystal fibers (HC-PCF), nanoparticles, or both. HC-PCF is a unique type of optical fiber, with continuous 'channels' of air (typically) running the entire length. The channels serve to confine electromagnetic waves in the core of the fiber, and tailor its transmission properties. Using HC-PCF as a biosensor requires development of a robust technique to fill hollow-core photonic crystal fibers. Though several groups have reported selective filling of HC-PCF's core, the processes are cumbersome and limit the choice of liquid to avoid multimode behavior. In my Master's thesis, I presented a simple technique to non-selectively fill all the HC-PCF channels with samples. The non-selective filling preserves the photonic bandgap property of the fiber, and yields an extremely strong interaction of light and the sample that produces considerable enhancement of the Raman signal from the analyte. Up to now, non-selective filling was accomplished through capillary action and it delivered a Raman signal enhancement of approximately 30-fold, which is not sensitive enough to detect biomolecules at the clinical level. Moreover, there were issues of reliability and reproducibility, due to evaporation, filling and coupling light into the fiber.

The objective of this PhD research was to overcome these problems by developing a robust optical fiber platform based on Raman spectroscopy that can be used in a clinical setting. I initially focused on heparin, an important blood anti-coagulant that requires precise monitoring and control in patients undergoing cardiac surgery or dialysis. Since the Raman spectra of heparin-serum mixtures exhibits Raman peaks of heparin with poor signal-to-noise ratios, I concentrated on enhancing the heparin Raman signal and filtering out the spectral background of

the serum to improve detection sensitivity. Reaching maximum enhancement of the Raman signal required a strong interaction of light and analyte, which can be achieved by using hollow core photonic crystal fiber as I had used in my Master's research. Using a small piece of HC-PCF I was able to reach an enhancement in the heparin Raman signal of greater than 90-fold. With this degree of enhancement, I was able to successfully detect and monitor heparin in serum at clinical levels, something that had never been accomplished previously.

After developing HC-PCF as a Raman signal enhancer, I focused on making the HC-PCF sensor robust, reliable and reusable. This was achieved by integrating the HC-PCF with a differential pressure system that allowed effective filling, draining and refilling of the samples in an HC-PCF, under identical optical conditions. To demonstrate the device's detection capabilities, various concentrations of aqueous ethanol and isopropanol, followed by different concentrations of heparin and adenosine in serum, were successfully monitored.

To further improve the sensitivity of the HC-PCF based Raman sensor, I incorporated surface enhanced Raman scattering (SERS), by introducing nanoparticles into the HC-PCF fibers. The research focused on determining the optimal volume and size of silver nanoparticles to achieve maximum enhancement of the Raman signal in the HC-PCF. The HC-PCF enhanced the Raman signal of Rhodamine 6G (R6G) approximately 90-fold. In addition, the optimal size and volume of AgNP enhanced the Raman signal of R6G approximately 40-fold, leading to a total enhancement of approximately 4,000 in HC-PCF. This was then used to demonstrate the application of a SERS based HC-PCF sensing platform in monitoring adenosine (a clinically important molecule), as well as malignant cells such as leukemia.

Finally, I used hollow core crystal fibers to significantly enhance the efficiency of two-photon photochemistry. Although two-photon photochemical reactions are difficult to achieve with a small volume, I accomplished it by using a novel platform of HC-PCF to efficiently execute the two-photon induced photodecarbonylation

reaction of cyclopropenone 1, and its conversion to the corresponding acetylene. The simple optical design configuration involved coupling an 800-nm tsunami laser to a short piece of HC-PCF filled with the sample. This allowed me to increase the efficiency of two-photon induced photochemistry by 80-fold, compared to a conventional spectrophotometer cuvette. Thus, this work leads to the use of HC-PCFs to more effectively study two-photon induced photochemistry processes, which was limited due to the difficulty of detecting photochemical events with a small excitation volume.

Acknowledgments

I would like to thank many individuals who during the course of my research offered great support and guidance. Within this period I met many nice people and enjoyed many beneficial conversations. I would like to thank everyone with whom I had a chance to work with during my studies at University of Ottawa.

Firstly, I would like to express my sincere gratitude to my advisor Dr. Hanan Anis with whom I have worked since my master's program and continued throughout my PhD. I have been amazingly fortunate to have an advisor who gave me the freedom to explore on my own, and at the same time the guidance to recover when my steps faltered. Her guidance and immense knowledge helped me all the time during my research and writing the thesis. I could not have imagined having a better advisor and mentor for my Ph.D study.

Besides my advisor, I would like to thank the rest of my thesis committee: Dr. Trevor Hall, Dr. Hans Peter Loock, Dr. Maria C. DeRosa, Dr. Pierre Berini, and Dr. Sangeeta Murugkar, for their insightful comments and encouragement, but also for the suggestion and feedback which incented me to widen my research from various perspectives.

The work presented in this thesis has been done in a close collaboration with research teams from other laboratories. My sincere thanks go to Dr. Michel Godin at the Department of Physics for guiding in developing H-shaped pressure driven system for HC-PCF biosensor. I also would like to thank Dr. Tito Scaiano from Department of Chemistry who provided me an opportunity to work in the laboratory and research facilities.

I would like to express my gratitude towards all the members of the group. Their valuable suggestions and discussions contributed to my research. I would like to

especially thank Dr. Vidhu Tiwari, and Dr. Majid Naji for providing all the support and for fruitful discussions.

My research work has been made possible by many blessings I receive in my personal life. I would also like to thank my family who have always trusted and showed unconditional love and support throughout my life and in particular, I must acknowledge my wife without whose love, and encouragement, I would not have finished this thesis.

Lastly, I recognize that this research would not have been possible without the financial assistance of NSERC CREATE, the School of Electrical Engineering and Computer Science and Graduate Studies at the University of Ottawa (Teaching Assistantships, Graduate Research Scholarships), and express my gratitude to those agencies.

Table of Contents

List of Figures

List of Tables

Number *Page*

Glossary

A1AT: Alpha-1-antitrypsin

ACT: Activated clotting time

AFP: Alpha fetoprotein

AgNP: Silver nanoparticles

AML: Acute Myeloid Leukemia

APTT: Activated partial thromboplastin time

ATP: Adenosine triphosphate

BP: Bandpass filter

CARS: Coherent anti-Stokes Raman scattering

CCD: Charge-coupled device

COPD: Chronic obstructive pulmonary disease

DNNS: Dinonylnaphthalenesulfonate

DNA: Deoxyribonucleic acid

EF: Enhancement factor

EM: Electromagnetic

FCV: Full cross validation

FEM: Finite element method

FOM: Figure of merit

GNP: Gold nanoparticles

HCC: Hepatocellular carcinoma

HC-OF: Hollow core optical fiber

HC-PCF: Hollow Core Photonic Crystal Fiber

HPLC: High performance liquid chromatography

HSW: Hollow core silica wave guides

IR: Infrared

LSPR: Localized surface plasmon resonance

LOD: Limit of detection

MEMS: Microelectromechanical systems

MPA: Multi-photon absorption

MRD: Minimal residual diseases

NA: Numerical aperture

NIR: Near Infrared

NOA: Norland Optical Adhesive

NP: Nanoparticle

OSA: Optical spectrum analyzer

PBF: Photonic bandgap fibers

PBS: Phosphate buffer solution

PC: Principal components

PCA: Partial component analysis

PCF: Photonic crystal fiber

PDE: partial differential equations

PDMS: Polydimethylsiloxane

PDT: Photodynamic therapy

PLS: Partial least square

R6G: Rhodamine 6G

RMSE: Root mean square error

RS: Raman scattering

SERS: Surface enhance Raman scattering

SPR: Surface plasmon resonance

SRS: Stimulated Raman scattering

TIR: Total internal reflection

TPA: Two-photon absorption

TPE: Two-photon excitation

TSV: Test set validation

USP: United States Pharmacopeia

Symbols

A_{eff}: effective cross-sectional area

d: diameter of the nanoparticles

E_0 : electric field

E: transition energy of the excited atom or molecule

f_0: frequency

f_m: frequency of the vibrational mode

h: Planck constant

I_0**:** intensity of the input light source

I_{RS}: intensity of the Raman scattering

k: absorption coefficient of the nanoparticles

L**:** interaction length between the laser and the sample

l: channel length of the fiber

L_{int}: effective constant interaction length

n_{air}**:** refractive index of air

n_{sil}**:** refractive index of silica

n_{liq} **:** refractive index of the liquid or gas

n_{core} : refractive index of the HC-PCF core

n_{clad} : refractive index of the HC-PCF cladding channels

N: standard deviation of the spectral background noise

p: molecular polarizability

ΔP: pressure difference across the HC-PCF

p_0: polarizability of the molecular mode at the equilibrium position

P: dipole moment

P_{fwd}: Raman signal collected in the forward direction

P_{bkwd}: Raman signal collected in the backward direction

q_0: amplitude of the vibration

r: radius of the HC-PCF channels

S: slope of the calibration curve

v_i: frequency of the i-th absorbed photon

w_0: half the beam at the focus

Δw: wavelength shift (Raman)

Z_R: Rayleigh length

ε: dielectric constant

α: optical loss of the fiber

ρ: number of scattering centers per unit length

σ: Raman sample cross-section

μ: viscosity of the sample

λ_{exc}: wavelength of the excitation light

λ^0: wavelength at which the bandgap originally occurs

λ: wavelength of the laser light in the vacuum

λ': wavelength of the shifted bandgap

Chapter 1. Thesis Objective and Contributions

This chapter presents the objective and contributions made by this thesis.

1.1 Background

Raman spectroscopy is based on a light scattering phenomenon known as the 'Raman Effect', discovered by Sir C.V. Raman and K.S Krishnan in 1928 [1]. The Raman Effect occurs when a light is incident on an atom or molecule, and some of the light is scattered while the rest is absorbed. Most of the scattered light is elastically scattered, which is known as Rayleigh scattering, and has the same wavelength and frequency as the incident light. However, a small fraction of the photons (approximately one in a million) are scattered at a different frequency, which is usually lower than that of the incident light. The amount of energy corresponding to the shift in wavelength is due to the vibrational and rotational energy level of the molecules in the sample. The spectrum created by the shift in frequency is known as the Raman spectrum, and the phenomenon is called the Raman Effect [2-3].

Raman spectra typically have many sharp peaks that correspond to specific molecular vibrational frequencies, and these clearly identify the presence of specific molecules in the sample. Thus, Raman spectra can be used to differentiate between chemical species in materials, and can be used in qualitative and quantitative analysis [4]. However, despite its distinct capabilities, a key limitation of the Raman Effect is its extremely weak signal, which means that longer acquisition times and more powerful lasers are required. Higher powered lasers can damage samples and limit the biological applications of Raman spectroscopy. Fortunately, there are other ways to increase a weak Raman signal,

such as surface-enhanced Raman scattering (SERS), stimulated Raman scattering (SRS) and coherent anti-Stokes Raman scattering (CARS). In general, the Raman signal intensity depends on various parameters, including interaction length and input laser power, which can be obtained from the following equation:

$$I_{RS} = I_o \sigma \rho L \tag{1.1}$$

where I_0 is the intensity of the input light source, σ is the Raman sample cross-section (cm^2/molecule), ρ is the number density of scatters (molecule per cubic centimeter) and *L* is the interaction length between the laser and the sample (cm) [5,6]. Since Raman intensity (I_{RS}) is directly proportional to interaction length, I concentrated my Ph.D research on enhancing the Raman signal of biological samples by increasing the interaction length with hollow core photonic crystal fiber (HC-PCF).

To further improve the sensitivity of the HC-PCF based Raman sensor, nanoparticles were incorporated inside the HC-PCF resulting in surface enhanced Raman scattering (SERS). This provided three orders of enhancement of the Raman signal. The enhancement through SERS is given by equation:

$$I_{SERS} = I_o \sigma_{ads}^{R} \rho' |G|^2 L \tag{1.2}$$

where σ_{ads}^{R} is the Raman sample cross-section of the adsorbed molecule (cm^2/molecule), ρ' is the number density of scatters that are involved in SERS (molecule per cubic centimeter), L is the interaction length between the laser and the sample (cm) and G is the gain coefficient [7].

1.2 Objective

The objective of my research is to develop a robust, optical fiber-based Raman biosensor platform that can be used in a variety of applications. This was accomplished by integrating hollow core photonic crystal fiber with differential pressure systems to provide effective filling, draining and refilling of samples in the fiber. With this technique I was able to demonstrate the device's detection

capabilities by monitoring different concentrations of heparin and adenosine in serum. In order to further improve the detection sensitivity of the system, nanoparticles were incorporated inside the HC-PCF to achieve an enhanced Raman signal through surface enhanced Raman scattering (SERS).

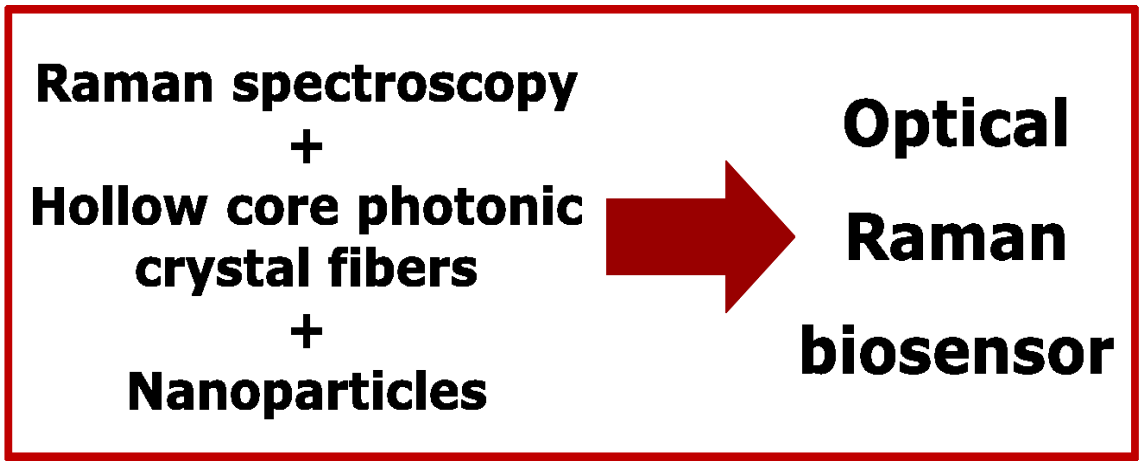

Figure 1-1 Optical Raman biosensor

The combination of HC-PCF and the SERS platform offers several advantages:

- It can be used simultaneously for light guiding and as a fluidic channel. This leads to a strong light/sample overlap over a large interaction length, which provides the potential for the development of simple, compact and sensitive biosensors.
- The volume of the samples consumed is in the range of nano to picoliter, which significantly decreases the sample consumption rate. When investigated using a test tube or cuvette, a sample under analysis typically requires at least a milliliter.

1.3 Contribution

The results of this thesis were achieved in the Innovation Photonics Lab from 2010 to 2015. Some of the work is due to collaboration with research groups in the Department of Physics, the Department of Chemistry and the Heart Institute at the

University of Ottawa. The research has generated four journal papers, one to be submitted journal papers, one book chapter, one granted patent and four conference proceedings. The results have also been presented at several international conferences. P11 was awarded the IEEE best paper at the sensor conference in New Zealand, while P3 was awarded first prize at the University of Ottawa graduate studies and research day.

1.3.1 Journal articles

P1. V. S. Tiwari, **A. Khetani**, A. Momenpour, and H. Anis: “Optimum size and volume of nanoparticles within hollow core photonic crystal fiber.” IEEE Journal of selected topics in Quantum Electronics 20, 3, 7300608 (2014).

P2. **A. Khetani**, A. Momenpour, J. Riordon, V. S. Tiwari, M. Godin and H. Anis: “Hollow core photonic crystal fiber as a re-usable Raman biosensor.” Optics Express 21, 12340-12350 (2013).

P3. **A. Khetani**, V. S. Tiwari, A. Harb and H. Anis: “Monitoring of heparin concentration in serum by Raman spectroscopy within hollow core photonic crystal fiber.” Optics Express 19, 15244-15254 (2011).

P4. **A. Khetani**, A. Momenpour, E.Alarcon and H. Anis: “Hollow core photonic crystal fiber for monitoring leukemia cells using surface enhanced Raman scattering (SERS).” Biomedical Optics Express 6, 4599-4609 (2015).

P5. **A. Khetani**, S. Impellizzeri, J.C. Scaiano and H. Anis: “Hollow core Photonic Bandgap Fiber for efficient two photon induced photo-chemistry.” (to be submitted)

1.3.2 Book chapters

P6. **A. Khetani**, V. Tiwari, A. Momenpour and H. Anis: “Silver nanoparticles in SERS based (micro)devices” in “Silver Nanoparticles From Surface

Resonance to Biomedical Applications." edited by Klas Udekwu, May Griffith and Emilio Alarcon, published by Springer (2015)

1.3.3 Patents

P7. **A. Khetani**, M. Naji, N. Lagali, R. Munger and H. Anis: "A method for using photonic crystal fiber as a Raman biosensor." US patent 7,738,097 (2010)

1.3.4 Conference proceedings

P8. **A. Khetani**, A. Momenpour, J. Riordon, V. S. Tiwari, M. Godin and H. Anis: "Hollow core photonic crystal fiber as a robust Raman biosensor." SPIE Photonics West 8576-14 (2013).

P9. V. S. Tiwari, **A. Khetani**, A. Momenpour, H. Anis and V. Trudeau: "Detection of neurotransmitters by surface enhanced Raman scattering (SERS) within hollow-core photonic crystal fiber." SPIE Photonics West 8233-28 (2012).

P10. **A. Khetani**, V. S. Tiwari, A. Momenpour and H. Anis: "Monitoring of adenosine within hollow core photonic crystal fiber by surface enhanced Raman scattering (SERS)." In: 2011 11th IEEE Conference on Nanotechnology (IEEE-NANO), 973 (2011).

P11. V. S. Tiwari, **A. Khetani**, M. Naji and H. Anis: "Study of Surface Enhanced Raman Scattering (SERS) within hollow core photonic crystal fiber." IEEE Sensors conference, 5404 (2009).

In this thesis, I personally planned the measurement setups, carried out the majority of the measurements and performed the main aspects of the analysis of the results while the statistical analysis was performed by Ali Momenpour, PhD student in our lab. I also wrote the manuscript of 2, 3, 4, 5, 6, 7, 8 and 10, contributed to papers 1, 9 and 11, and conducted the measurements in paper 2 in the Department of Physics at the University of Ottawa.

In order to create a robust Raman sensor using HC-PCF, several reservoir configurations were implemented. The pressure driven system common to micro-electromechanical systems (MEMS) microfluidic flow control, proposed by Michel Godin's group, was found to be the most robust. For paper 1, I constructed the measurement setup, carried out most of the measurements and contributed to the analysis of the results. I also participated in the experiments and contributed to the analysis of the results in papers 1 and 9. For paper 4, leukemia cell samples were cultured at University of Ottawa Heart Institute, and for paper 5, the two photon photoreactor samples were prepared in the Chemistry Department at the University of Ottawa. For papers 10 and 11, I was involved in the experiments and analysis of the measurement results. Throughout the thesis, I learned various techniques and implemented diverse strategies, including:

- implementation of an experimental setup for monitoring various chemicals through Raman spectroscopy;
- evaluation of the best Raman configurations (backward and forward);
- study of various hollow optical fibers for Raman signal enhancement;
- implementation of various reservoirs in order to perform tests to ensure the sensor platform was stable and robust, and to achieve reproducible Raman results for statistical analysis;
- optimization of the size and volume of nanoparticles in the hollow-core photonic crystal fibers for the enhancement of a Raman signal;
- design of a compact and portable Raman measurement unit; and,
- implementation of an experimental setup to study two photon inducing photochemistry using a tsunami laser.

1.4 Thesis outline

The balance of the thesis is organized as follows:

Chapter 2 introduces Raman spectroscopy and photonic crystal fibers. Raman scattering is discussed, as well as figures of merit to evaluate different geometries to increase the interaction length between light and analyte. This is followed by an introduction to hollow core photonic crystal fibers, different filling methods for PCF, bandgap shift properties and simulation results. Surface enhanced Raman scattering mechanisms and their applications are also covered in this chapter.

Chapter 3 discusses the optimization of the Raman setup and the experimental configuration. It covers HC-PCF and Raman spectroscopy for analysing different chemicals, and the use of Heparin as the sample of interest to prove HC-PCF sensor capabilities. The chapter includes a literature review of the methods to monitor heparin concentration, followed by the optical characterizations of sample mixtures (heparin-serum). The spectral results and analysis are also presented.

Chapter 4 focuses on making HC-PCF a robust sensor platform by using differential pressure systems common to microfluidic flow control. It presents our findings on optimal pressure differences, sample filling times into HC-PCF and stability tests. The chapter also provides the results of the multivariate calibration model's predictions of the sensor response to other chemicals, including ethanol, isopropanol, heparin and adenosine.

Chapter 5 examines achieving surface enhanced Raman scattering In HC-PCF. The purpose of the chapter is to discuss further enhancement of the Raman signal by combining HC-PCF and nanoparticles. The actual contribution of HC-PCF and nanoparticles to the overall enhancement of Raman signals—determined by analyzing different sizes and volumes of nanoparticles in sample mixtures—is discussed, as well as the performance of the SERS based HC-PCF sensing platform for monitoring malignant leukemia cells and adenosine, a clinically important molecule.

Chapter 6 focuses on studying two photon induced photochemistry in hollow core photonic crystal fibers. Although two photon photochemical reactions are difficult to achieve in a small volume, this was overcome by simply coupling an 800 nm fs pulsed laser into a short piece of HC-PCF filled with the sample. This technique increased the efficiency of two-photon induced photochemistry by two orders of magnitude, compared to a conventional spectrophotometer cuvette.

Chapter 2. Introduction to Raman spectroscopy and Hollow Core Photonic Crystal Fibers

2.1 Introduction

In this chapter, we first present a brief overview of Raman spectroscopy, then in section 2.3, we discuss the figure of merit, which is used to theoretically evaluate enhancement factors for cuvette and hollow core optical fiber (HC-OF). Section 2.4 provides the background of hollow core photonic crystal fiber, including the bandgap shift property of the fiber and different filling techniques. Section 2.4 also discusses the different reservoir systems used to achieve consistent HC-PCF filling for spectral reproducibility that allow statistical analysis of clinical samples. Section 2.5 explains the enhancement in the Raman signal from using nanoparticles known as Surface Enhanced Raman Scattering (SERS), followed by literature review.

2.2 Raman spectroscopy

Raman spectroscopy is an interesting technique, as it provides unique 'molecular fingerprints' of chemicals that correspond to the vibrational frequencies of molecular bonds. It is also a powerful molecular fingerprinting technique that enables analysis of materials through the interaction of the material's molecules with an incident laser beam [5]. Raman spectroscopy applications are extremely diverse, and include the study of minerals, the characterization of polymers and pharmaceuticals compounds [6, 8-10]. Raman spectroscopy has been used for the chemical characterization of different materials for many years, and lately it has been applied to the study of biological samples to provide rapid and accurate

identification of biomolecules [11]. One of the reasons for the surge in interest is the availability of increasingly sophisticated, powerful, fast and portable Raman spectroscopy instrumentation, as well as improved statistical techniques to analyze the data. The need for a robust platform has also become very important, due to the need for rapid analysis and diagnosis [11-15]. For example, in 2012 23% of annual deaths worldwide were caused by infectious diseases [16].

The Raman effect has been accepted for decades, and the physics behind it are well understood [17]. In 1923, Smekal theoretically predicted inelastic scattering, and in 1928 Raman and Krishnan reported observation of the effect, which is known as Raman scattering" [18-19]. Widespread Raman spectroscopy applications began to emerge after the invention of lasers in the 1960s, and when highly sensitive detectors and optical components became available in the 1980s it was successfully applied to materials characterization [20]. The effect is caused by the inelastic scattering that occurs when incident light (assume monochromatic laser radiation) of wavelength λ_0 and frequency f_0 is scattered by the vibrating molecules of a sample. The electric field of the laser beam oscillates with time (t), as given by equation 2.1,

$$E = \mathrm{E}_0 \cos(2\pi \cdot \mathrm{f}_0 \mathrm{t}) \tag{2.1}$$

where E_0 is the amplitude of the oscillating electric field that will induce an electric dipole moment P in the molecule given by $P = pE$. The proportionality constant *p* is known as molecular polarizability, and is a material property that depends on the material structure and bond nature. *p* can be expanded around the normal coordinates of the vibrating molecule for small amplitudes of vibration, as given by equation 2.2,

$$p = p_0 + \left(\frac{\partial p}{\partial q}\right)\Delta \mathrm{q} + \ldots\ldots \tag{2.2}$$

Where p_0 is the polarizability of the molecular mode at the equilibrium position. The displacement of the normal coordinates of the molecules about their equilibrium position due to a specific vibrational modes can be expressed as,

$$\Delta q = q_0 \cos(2\pi f_m t) \tag{2.2a}$$

where f_m is the frequency of the vibrational mode and q_0 is the vibrational amplitude. Based on equations 2.1 and 2.2, the dipole moment becomes

$$P = p_0 E_0 \cos(2\pi f_0 t) + \frac{1}{2}\left(\frac{\partial p}{\partial q}\right) q_0 E_0 \left[\cos(2\pi\{f_0 + f_m\}\, t) + \cos(2\pi\{f_0 - f_m\}\, t)\right] \tag{2.3}$$

This equation represents an oscillating dipole which radiates photons with three different frequencies: f_0 (elastic scattering) in the first term, (f_0+f_m) (inelastic scattering with shorter wavelength – anti-stokes) in the second term, and (f_0-f_m) (inelastic scattering with longer wavelength – stokes) in the third term.

The theoretical value of Raman scattering intensity depends on the molecular composition of the sample, the molecule's specific vibrational modes, the power of the excitation source (typically a laser), and the laser wavelength (since the intensity is proportional to the fourth power of the laser frequency). The experimentally measured Raman intensity will not depend on the Raman scattering intensity only, but also on the experimental instrumentation, such as the detector and optics efficiency.

The change in wavelength shift between the incident and emitted light (Δw) is called the Raman shift, and the magnitude of the change is determined by the vibrational modes of the molecules in the sample. Though Raman shift is typically measured in units of cm^{-1}, it is actually a measurement of a wavelength shift. Equation 2.4 gives the value of the Raman shift, in terms of the incident and scattered photon wavelength.

$$\Delta w(cm^{-1}) = \left(\frac{1}{\lambda_{incident}(nm)} - \frac{1}{\lambda_{scattered}(nm)}\right) \times 10^{-7} \tag{2.4}$$

While most incident photons will scatter elastically with no change in frequency (Rayleigh scattering), a small portion of light (~10^{-8} of the incident beam) will scatter inelastically (Raman scattering) [17]. Since Raman scattering is a weak signal, researchers have attempted to improve the signal through various

configurations, including hollow fibers and integration with nanoparticles for SERS [21-28].

2.3 Figure of merit in cuvette and hollow core optical fiber

The figure of merit (FOM) is an important parameter when determining the different configurations to be used to achieve high sensitivity with Raman spectroscopy. The FOM is used to predict the relative intensity enhancement provided by hollow core optical fibers (HC-OF) with different core diameters and loss characteristics. FOM is defined as:

$$FOM = \frac{L_{int}\lambda_{exc}}{A_{eff}} \tag{2.6}$$

where λ_{exc} is the excitation light wavelength, L_{int} is effective constant interaction length and A_{eff} is the effective cross-section area of the laser beam and analyte [29].

Raman measurements are typically performed by exciting a sample in a cuvette with monochromatic laser light. Cuvettes can be circular, square or rectangular, and are usually made of quartz as it will transmit both incident and emitted Raman light. In cuvette based geometry, the free-space laser beam is tightly focused on the sample by an objective lens, resulting in high intensity near the focal point in the cuvette in the sample solution, as shown in Figure 2-1.

For a Gaussian laser beam focused inside an analyte (Figure 2.1) using a conventional optical setup, L_{int} and A_{eff} are [30,31]:

$$L_{\text{int}} = 2\,Z_{\text{R}} \tag{2.7}$$

$$A_{eff} = \pi\, w_0^2 \tag{2.8}$$

where Z_R is the Rayleigh length defined as $Z_R = \frac{\pi\, w_0^2}{\lambda}$, w_0 is half the laser beam at the focus and λ is the wavelength of the laser light in the vacuum.

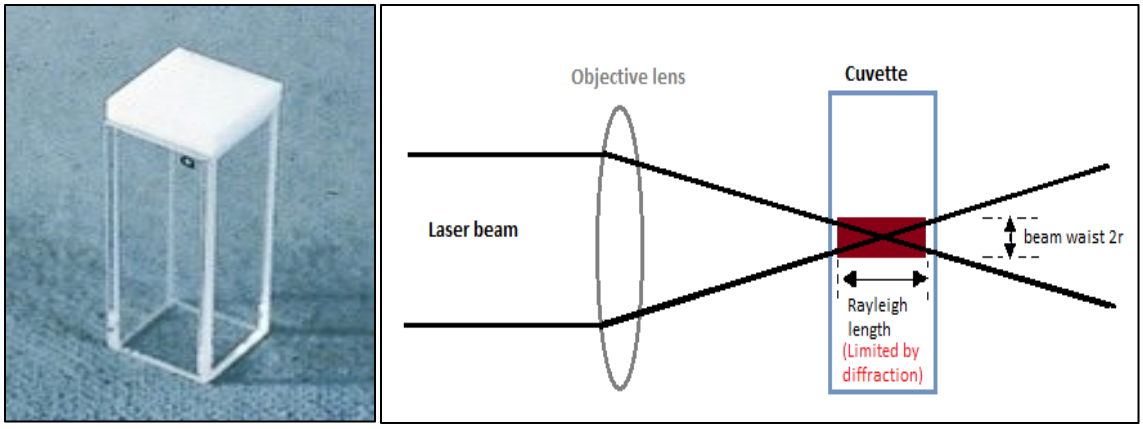

Figure 2-1 Cuvette based geometry
with L_{int} limited by the Rayleigh length in a focused free-space laser

By substituting (2.7) and (2.8) in (2.6), the FOM for the Gaussian beam focused on the sample in cuvette is:

$$FOM_{Gaussian} \cong 2 \tag{2.9}$$

It is evident from the above equations that the effective cross-sectional area is smaller (or has a higher focus intensity), which results in a shorter effective interaction length L_{int}, and allows each to counterbalance the effect of the other. Thus the FOM of 2 with cuvette geometry, which is diffraction limited for a tighter laser beam focus, is inefficient to increase the effect of matter-light interaction for recording Raman spectra. To achieve greater FOM, hollow core glass capillaries can be used as they guide light by total internal reflection and increase the effective interaction length; however, their high propagation loss is a key disadvantage. The ideal configuration for effective interaction requires a diffraction-free, lossless (α~0dB/m), single-mode waveguide, with a core diameter equal to the focused laser beam waist (~ μm), and HC-PCF comes close to achieving this [32]. Hence, the effective interaction length is approximated by the length of the fiber L_{HcPCF}, and the normalized FOM of HC-PCF becomes:

$$FOM_{HCPCF} = \frac{L_{HCPCF}\lambda}{A_{eff}} \cong L_{HCPCF}\frac{\lambda}{\pi w_{HCPCF}^2} \tag{2.14}$$

$$Enhancment\ factor_{HCPCF} \cong \frac{FOM_{HCPCF}}{FOM_{Gaussian}} \cong \frac{L_{HCPCF}}{2}\frac{\lambda}{\pi w_{HCPCF}^2} \quad (2.15)$$

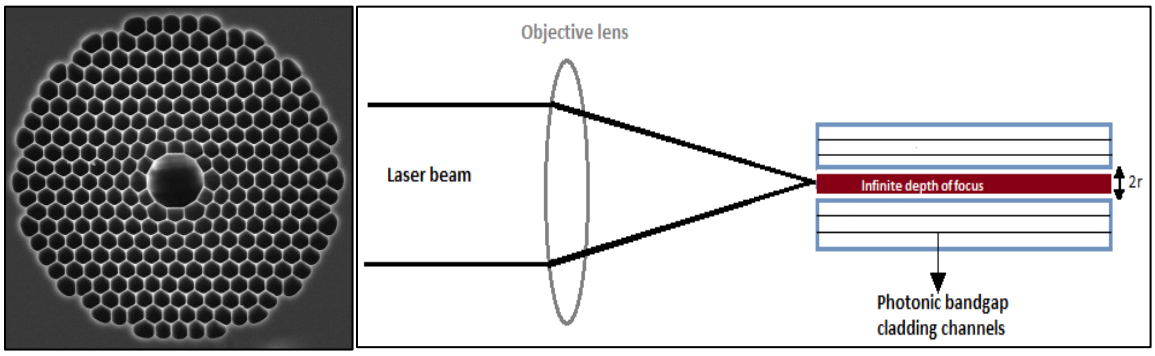

Figure 2-2 HC-PCF guiding mechanism

where high interaction length can be obtained due to the photonic bandgap that confines the light to propagate inside the core, thereby limiting loss.

Eq. 2.15 shows that the FOM of HC-PCF increases rapidly with a decrease of the core radius. Light is confined tightly (i.e. high intensity) along the entire length of the fiber. For example, in an ideal case for L=0.08 (m), w_{eff} = 10 μm, single mode transmission condition, and λ=1 μm and negligible loss, the enhancement factor will be approximately a factor of 110.

2.4 Hollow Core Photonic Crystal Fibers

In 1991, Russell *et al.* invented microstructure optical fibers. The fibers were silica, and had a cross-sectional periodic arrangement of air-channels running along their full length. Russell was awarded the Fraunhofer Award / Burley Prize of the Optical Society of America in 2000, for recognition of *"his invention of the photonic crystal fiber, an array of micron-spaced sub-micron holes allowing extremely large mode area single-mode fibers offering solid-core fibers with better power handling [33]."*

Photonic crystal fiber (PCF) geometry is characterized by a microstructured air hole cladding running along the entire length of the fiber, surrounding a solid or hollow core. Thus, PCF can be divided in two types: solid core and hollow core. In this thesis, we concentrate on hollow core PCF (HC-PCF) which guide light in a

hollow core instead of solid core, as is the case for conventional fibers. In this type of fibers, light is guided by a two-dimensional photonic bandgap in a hollow core or in a core made of a material with the refractive index lower than the effective index of the cladding.

HC-PCF has several major advantages over conventional sample cells [34-37], including:

- Low-waveguide losses (a few dB/m) allow the use of long optical-path lengths, and greatly enhance the effective light-matter interaction, as shown in Figure 2-3.

- A sample under analysis typically requires at least a milliliter of volume when examined by test tube or cuvette, while HC-PCF uses samples in the nano to pico-liter range which significantly decreases the sample consumption rate.

- The small required sample volume and large overlap of the propagating laser mode field with the sample in HC-PCF provide the potential to develop simple, compact and sensitive biosensors. At comparable input power, the intensity in a hollow core is five orders of magnitude higher than with cuvette-based approaches.

- PCFs are fabricated from chemically inert, high-quality silica glass, with negligible scattering, absorbance or fluorescence.

Despite the advantages with HC-PCF, complex manufacturing process and high price are the main disadvantages of using HC-PCF over conventional fibers. In addition, problems with coupling and possibility to connect them with other waveguides and devices are the few more drawbacks of HC-PCF.

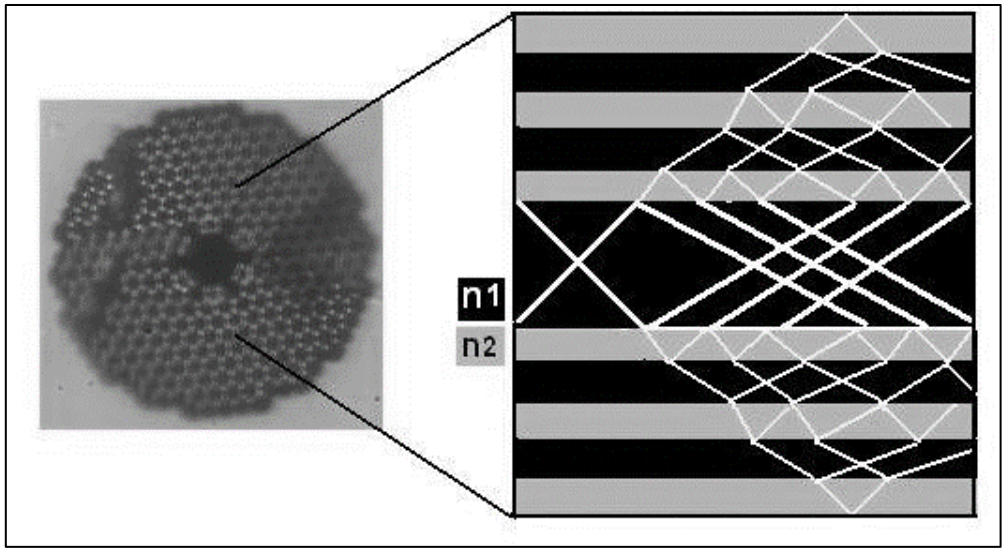

Figure 2-3 Guiding mechanism in HC-PCF

The guiding mechanism in bandgap-guiding fibers is unlike that of ‘step-index’ guiding fibers, due to the lower refractive index of the core. Due to the bandgap effect, certain light frequencies are unable to escape from the core and are reflected, leading to wavelength dependent on the light transmission. HC-PCFs guide the light by consecutive, constructive reflection interference from several air-silica interfaces. This type of periodic air-silica cladding creates a bandgap for photons in the radial direction, forcing the photons to propagate inside the core.

HC-PCFs can be filled in two ways: selective and non-selective. Selective filling only fills the core of the PCF, which is a complicated process because it has both a core and cladding channels. At the end of the process the core is readily accessible to be filled by a sample. The guiding occurs by total internal reflection (TIR), because the refractive index of the sample is lower than silica surrounded by cladding holes [38].

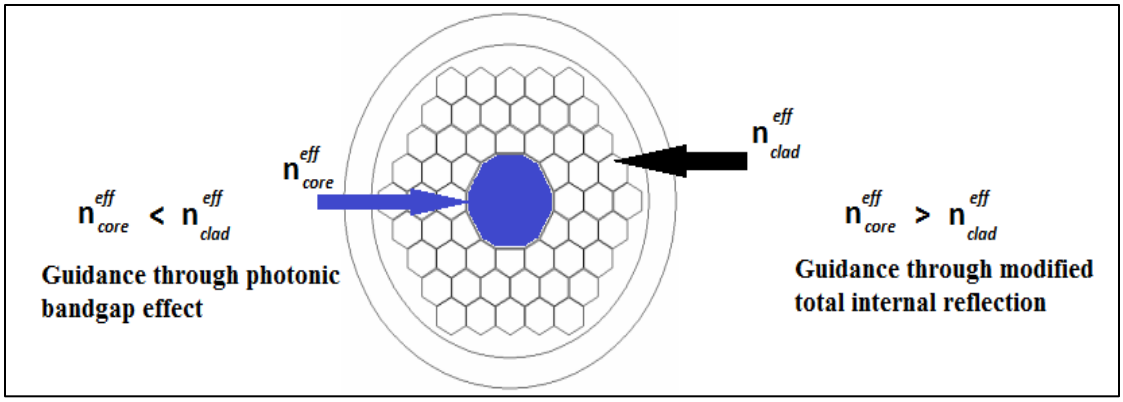

Figure 2-4 Light guidance when HC-PCF is filled selectively and non-selectively

One of the selective methods demonstrated by Huang *et al*. was filling the fiber with Norland Optical Adhesive (NOA) in multiple steps using a syringe. This approach allows the core to be filled with liquid that achieves guiding through total internal reflection [39]. In another method, demonstrated by Kristian *et al*., overhead pressure was applied to fill the core of the fiber selectively. This is a very detailed approach to fill a fiber, which is why complex steps are involved in the process. The method provides a model for calculating the time necessary to fill one or more specific channels with a polymer and water in a photonic crystal fiber [38]. The photonic band gap is not preserved with the selective filling approach, which makes filling HC-PCF with the sample quite difficult. Such time consuming sample filling procedures are not useful in clinical environments, which require simple and timely processes. The selective filling approach was also demonstrated by Zhang *et al*. by combining SERS and HC-PCF. In their experiment, the chosen test molecule rhodamine (R6G) was mixed with a silver nanoparticle colloidal solution, and a 10 mM concentration of NaCl was added to aggregate the nanoparticles for optimal SERS performance. With a 10 cm HC-PCF, an enhancement factor of ~100 was reported in the SERS experiment, with a lowest detectable concentration of 10^{-5} M [40]. Selective filling by laterally accessing the core channel of HC-PCF was demonstrates by Wang *et al.,* Zhang *et al.,* Hoo *et al.,* in which micromachining was done through femtosecond laser pulses while Hydrogen Fluoride was used for etching [41-43] .

In non-selective filling techniques, both the core and the cladding channels of a HC-PCF are filled with the sensing material. The advantages of this technique are that it is easy to do, simpler to implement, and it solves the problem of evaporation by inserting a reservoir of the liquid. Moreover, the photonic bandgap property of the fiber is preserved, which provides a greater increase in interaction length.

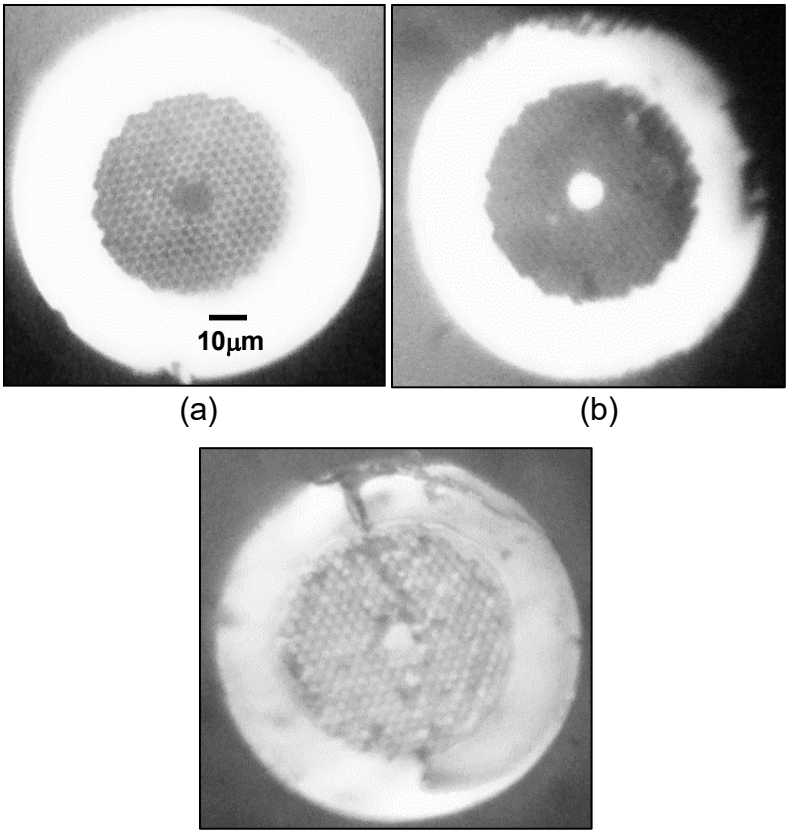

Figure 2-5 Cross-sectional view of HC-PCF when (a) empty, (b) selectively filled and (c) non-selectively filled

2.4.1 Band-gap shift property of the HC-PCF

The light guiding property of a non-selectively filled HC-PCF changes, depending on the refractive index of the filling sample. In this case, the guiding principle is still the bandgap effect, but the transmission band supported by the fiber is shifted. This shift in the transmission wavelength of HC-PCF can be determined from the

equation given by Antonopoulos *et al*. [44]. Due to the shift in the bandgap, the center wavelength of the shifted fiber is given by the formula

$$\lambda' = \lambda_0 \left[\frac{1 - \left(\frac{n_{liq}}{n_{sil}} \right)^2}{1 - \left(\frac{n_{air}}{n_{sil}} \right)^2} \right]^{1/2} \tag{2.16}$$

where λ_0 is the wavelength at which the bandgap originally occurred, λ' is the wavelength of the shifted bandgap, n_{air} is the refractive index of air, n_{sil} is the refractive index of silica and n_{liq} is the refractive index of the liquid or gas. In order to effectively use bandgap shift property requires a fiber that can guide the source wavelength when filled with liquid, such as experimental conditions when the source wavelength is 785 nm corresponding to the wavelength shift (λ'), and the liquid under examination is ethanol (n_{liq} = 1.36). By substituting the value λ', n_{liq}, n_{air} (=1) n_{sil}(=1.46) in the above equation, we can find λ_0 (the wavelength of the fiber when empty) to be 1550 nm, which indicates choosing the HC-1550 fiber [45].

Modeling a photonic bandgap fiber can be achieved in different ways, including the effective index method, the plane wave expansion method, the finite difference time domain method, the multipole method, and the finite element method (FEM). In this work, the HC-PBF modeling was done with COMSOL Multiphysics 3.3 commercial software, which follows a finite element approach [46]. COMSOL is FEM modeling software that describes partial differential equations (PDE's) by simulating a structure. It consists of unique modules, which enables users to solve a specific application or a combination of multi-physics. Electromagnetic field simulation of photonic components can be solved with an electromagnetic module. In order to model HC-PCFs such as HC-1550, the core diameter and pitch was scaled according to the manufacturer/supplier specifications.

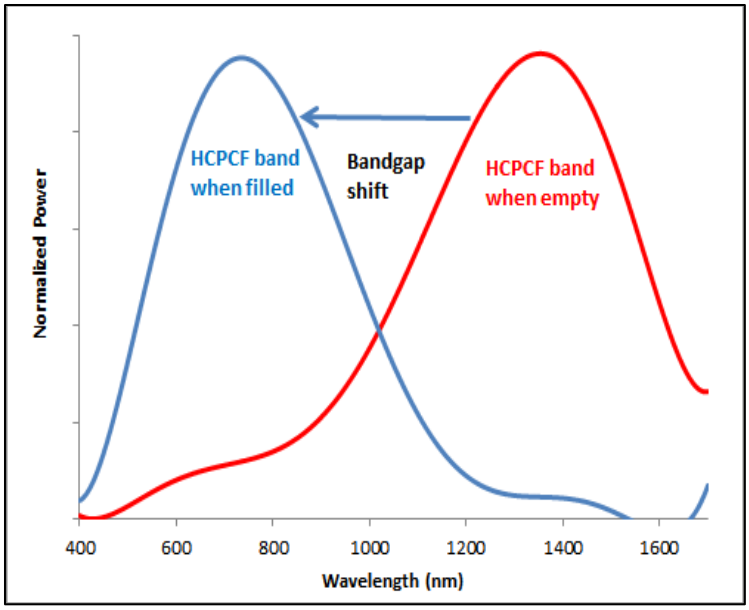

Figure 2-6 HC-PCF bandgap shift when empty, and filled with liquid samples

First, the geometry of the HC-1550 fiber was defined in the Matlab program, with specifications of core diameter 10 μm and cladding pitch 3.8 μm, and a separate code was written to define the hexagonal cladding structure. The geometry was exported using COMSOL script, as shown in Figure 2-7.

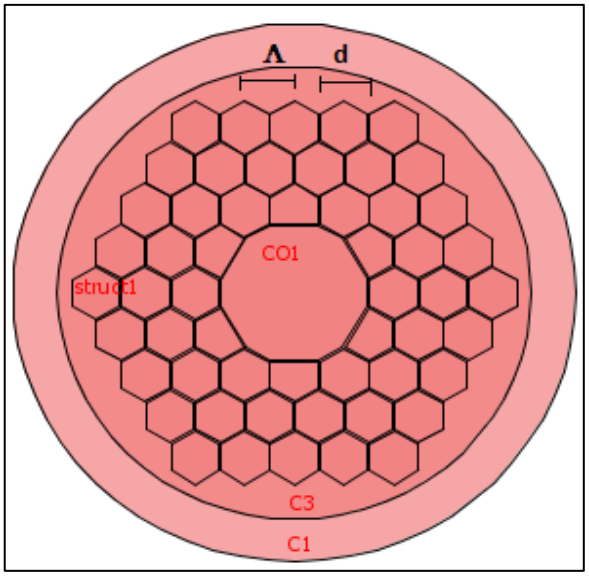

Figure 2-7 Geometry of the fiber HC-1550

Next, the COMSOL parameters were established as follows: The application mode is the PDE coefficient form, and the constants k (propagation constant 2*pi/λ), n_1 (RI of core), n_2 (RI of silica), n_3 (RI of cladding holes) are defined. Then the mesh is initialized as shown in Figure 2-8. The mesh consists of 44,869 elements with 89,796 degrees of freedom.

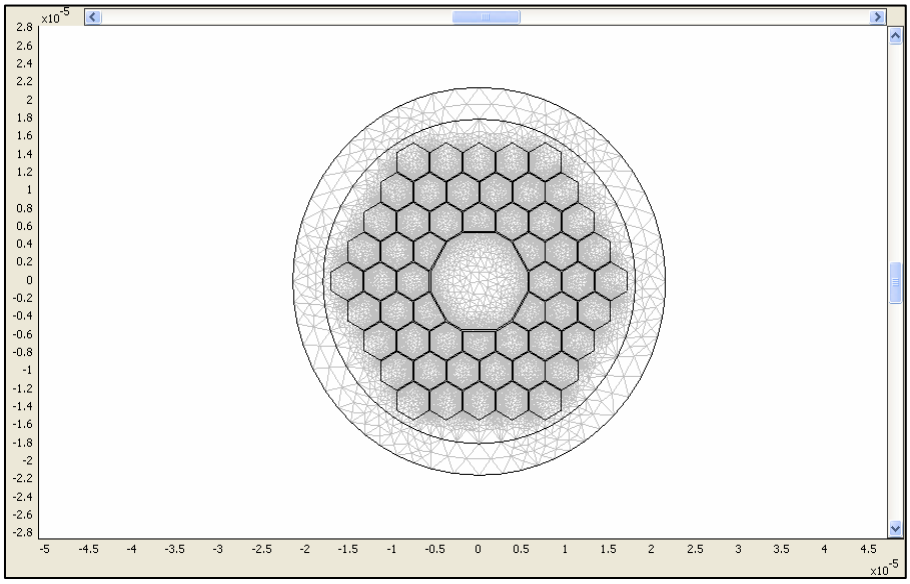

Figure 2-8 Mesh of the fiber HC-1550

Solving the geometry reveals many eigen value modes supported by the fiber. Since the effective refractive index of the fiber is close to 1, different eigenvalues are determined. For a particular eigen value of (0.996998 - $4.095091e^{-5}$i), the fiber would support single mode operation, as shown in Figure 2-9.

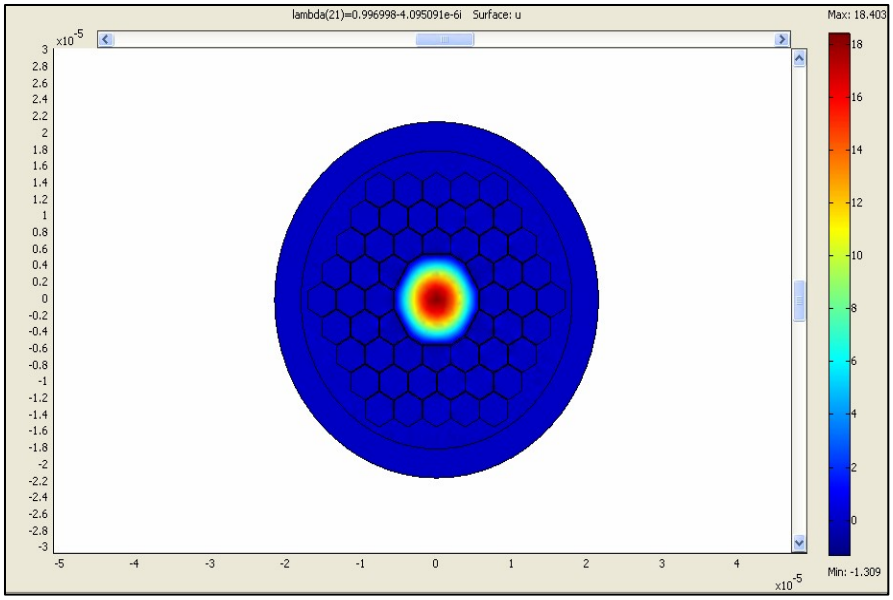

Figure 2-9 Simulation of empty HC-1550 supporting single mode

Finally, we fill all the holes of the fiber non-selectively by changing the refractive index parameter to the value that corresponded to the refractive index of the sample (e.g. ethanol n=1.36). According to the bandgap shift property of the fiber, it should guide 785nm. Different eigenvalues are generated by the software, and each has a mode associated with it. Searching for eigenmodes at eigenvalues closer to 1.84 ($n_{liquid}{}^2$ =1.84), revealed that eigenvalues of 1.838085 -1.981346e^{-5}i support the signal mode The simulated mode profile suggested that the fiber would guide 785 nm excitation light when filled ethanol, as shown in (Fig. 2.10); this was later confirmed by applying 785-nm laser light and observing the far-field pattern. The single mode pattern of the filled HC-1550 fiber is required to obtain maximum overlap of the sample and the excitation light, which results in strong Raman scattering from the sample.

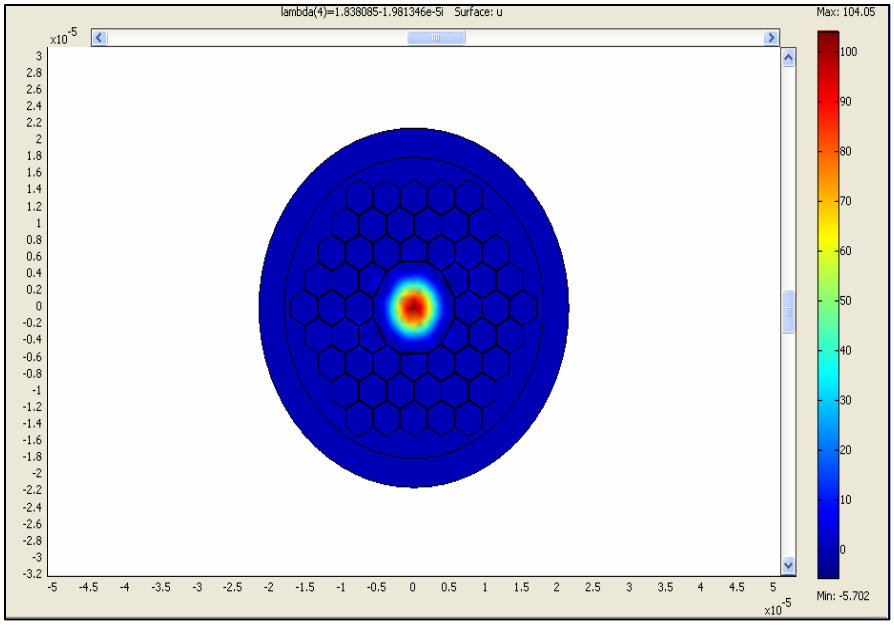

Figure 2-10 Simulation results of HC-1550 showing fundamental mode supported when filled with liquid samples

2.4.2 Statistical analysis

As discussed earlier, Raman scattering is a weak signal, and requires statistical analysis to correlate the weak Raman bands with the analyte concentration. Statistical analysis is important in Raman spectroscopy since it is used for quantitative analysis, particularly when there is an overlap of the Raman bands of interest with those of the sampling media (e.g. serum, blood). It provides a simple calibration curve between the Raman signal intensity and the sample concentration. Traditional analysis of Raman signals is univariate in nature, as the intensity of scattering at a given wavelength is used to monitor the analyte of interest. This analysis focuses on the variance of a single parameter (wavelength), and does not take full advantage of the information content of a complete spectrum, which means potentially useful data is excluded. As a result, several interfering factors contribute to univariate data, and quantitative information is difficult or impossible to obtain. Examples of interference in univariate analysis include fluorescence, blackbody radiation, laser power fluctuations, loss of focus, sample opacity, sample decomposition, optical alignment, overlapping peaks,

sample birefringence and samples outside the calibration sets. These problems are successfully addressed by multivariate analysis, as it has several features not available in traditional Raman analysis, such as greater selectivity, improved signal to noise ratio, enhanced visualization of complex data and consideration data reductions. Partial least square (PLS) and principal component analysis (PCA) were used in my thesis work.

Multivariate methods such as PLS perform quantitative analysis of spectral data by constructing models in which the response Y-variable (analytical data) depends on more than one explanatory X-variable (Raman shift wave number). Only linear combinations of the explanatory X-variables that are related to the response Y-variable are considered during the formulation of the calibration model. PLS has been successfully applied to determine bio-chemicals, tissues and cells [47].

2.4.3 Different reservoir configurations

One of the requirements of the statistical analysis is obtaining reproducible Raman spectra of samples under identical optical and filling conditions. The practical difficulties associated with implementing HC-PCFs for real-time monitoring of samples are as follows:

- Light coupling and guidance are affected by frequent formation of air gaps or discontinuities in sample distribution in the micro-channels. This results in poor quality spectra that do not correlate well with chemical concentrations.

- HC-PCFs are typically used once and replaced, which is time-consuming and influences the light coupling conditions. HC-PCF based sensors are traditionally filled through capillary action, a slow technique that cannot meet the high throughput demands of clinical instrumentation.

- Lack of a means of evacuation prevents their reuse, and impedes real-time sensing.

- Variability in the light launching conditions from one HC-PCF to another alters the propagation properties. This makes it difficult to ensure spectral reproducibility, a key requirement for statistical analysis.

In order to achieve reproducible Raman signals, different reservoir schemes to consistently fill the fiber are discussed. Figure 2-11 (a) and (b) show a needle reservoir that is simple to implement. A glass coverslip is glued to a 22g size needle with a small piece of HC-PCF inserted in it, and the filling is done by capillary action. However, the high light power density in the HC-PCF evaporates the sample in the reservoir, resulting in the formation of air gaps or non-uniform sample distribution in the HC-PCF channels. The light is only partially guided within the HC-PCF, which leads to an overall decline in the Raman signal of the chemical of interest. Thus, an aluminum-based, in-house sample reservoir that continuously replenishes the sample in the HC-PCF channels was designed (Figure 2-11 (c)). Though this reservoir has the advantage of pumping the sample to the fiber, there was no way to keep the fiber straight. In addition, drops of liquid formed on the end of the fiber, which changed the launching conditions of light into the fiber. A new reservoir was designed to overcome these drawbacks (Figure 2-11 (d)). It consisted of two Swagelock Tee fittings, connected through a glass capillary with an inner diameter of 250 μm, which is large enough to hold the HC-PCF tightly. One end of the tee was glued to a glass cover-slip which formed the optical window, and the other was connected to the syringe sample pump. One of the tee connectors of the Swagelock-capillary reservoir was used to pump the sample in, and the other to flush out the sample. Though this new reservoir overcame the problems of the previous, sample flushing took a long time as the dead volume inside the fittings had to flush out through the small HC-PCF channels.

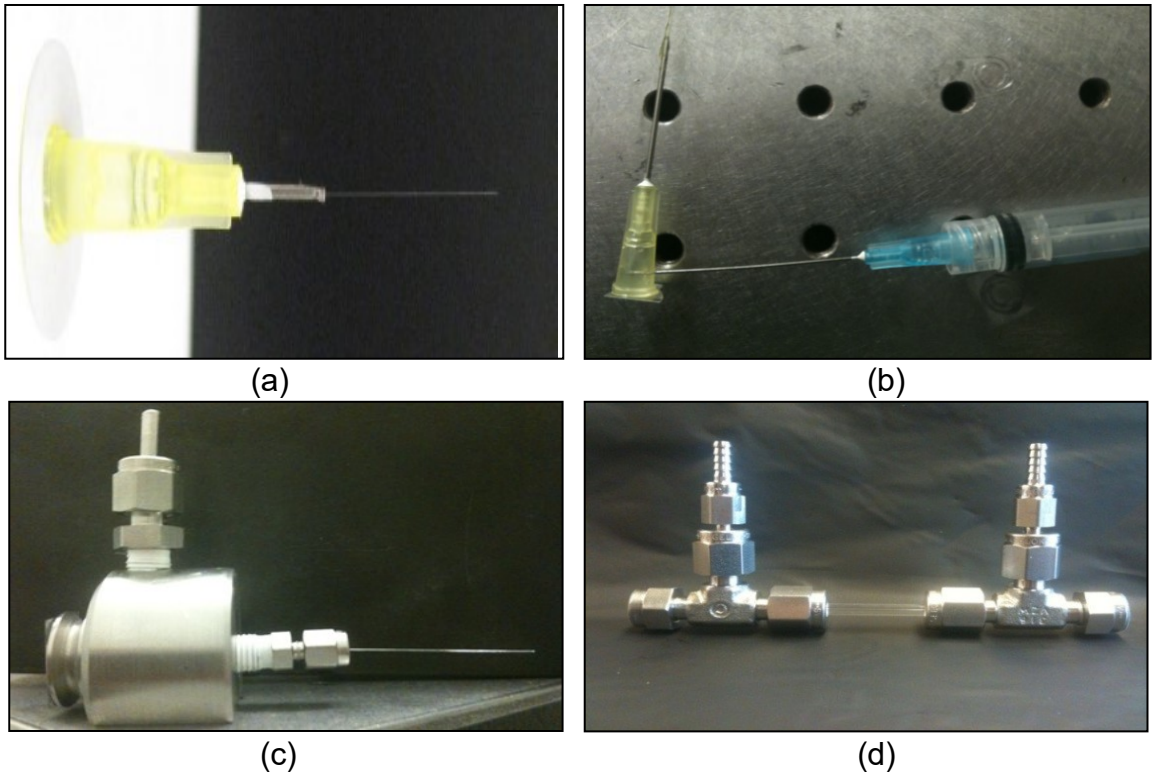

Figure 2-11 Various reservoir design approaches
(a) needle reservoir, (b) needle reservoir with a syringe for pumping a sample, (c) aluminum based reservoir connected to a syringe pump and (d) Swagelok-capillary reservoir for HC-PCF fiber.

2.5 Surface Enhanced Raman Scattering (SERS)

A key limitation of the Raman effect is its weak signal strength, which requires longer acquisition times and high power lasers that can damage samples and limit the biological applications of Raman spectroscopy. A common technique to increase weak Raman signals is surface enhanced Raman scattering (SERS) [48], a powerful analytical method for the detection and identification of extremely low concentrations of molecular species. It overcomes the low Raman cross section barrier by exploiting the large field enhancement due to the electromagnetic coupling between nanoparticles. Under such conditions, the Raman signal of the target molecule is enhanced by several orders of magnitude, which allows detection down to a single molecule [49-52]. In general, SERS is performed on a

gold (Au), silver (Ag) or copper (Cu) colloid or substrate. Most applications use Au and Ag, as they are air stable and absorbance is mainly in the visible and near IR wavelengths. Researchers have attempted to obtain maximum enhancement of SERS signals by optimizing the structure, shape, volume ratio and configuration. The increasing interest in SERS is evident by the growing number of related articles published over last three decades, as shown in Figure 2-12. Though different metallic nanoparticles have been used in SERS studies, my work is largely focused on using silver nanoparticles (AgNPs) for SERS and its applications.

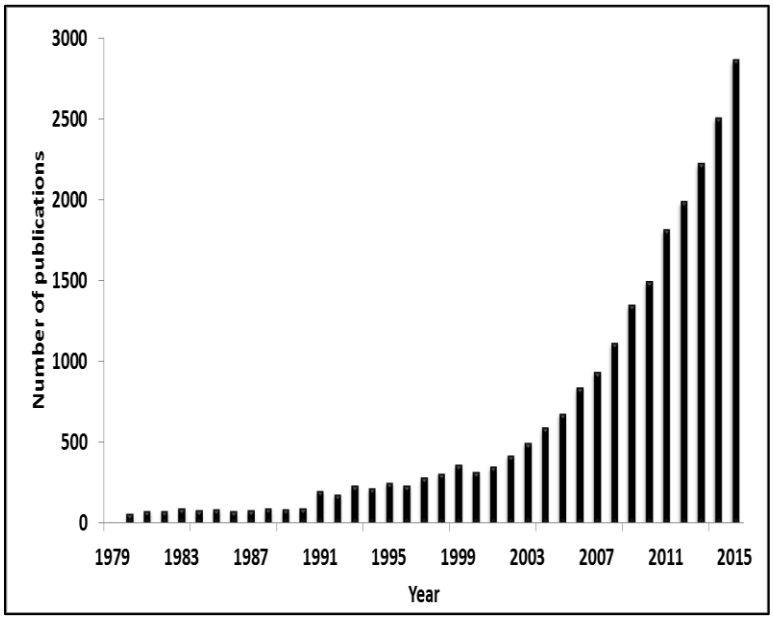

Figure 2-12 Representation of the number of research articles regarding SERS published from 1979 to 2015 (data obtained from a Web of Science search on "surface enhanced Raman").

Enhancements of the Raman signal on the order of 10^6 to 10^8 has been achieved with highly optimized configurations [53, 54]. SERS has been used primarily as an analytical technique in the fields of biochemistry, forensics, food safety, threat detection and medical diagnostics [55-57]. SERS is popular because it offers: (i) molecular fingerprints down to the level of single molecule detection, (ii) label-free detection rather than fluorescence spectroscopy, (iii) multiplex detection, (iv)

minimal sample requirements, and (v) in-situ and in-vitro characterization of biological samples.

The capability of SERS applications is due to its ability to identify chemical species and obtain structural information over a wide variety of applications. SERS has played a major role in detecting several molecules, and achieved high detection sensitivity to the point of detection at the single-molecule level, which is required in research areas such as biosensing, analytical chemistry and biomedicine. Some of the relevant SERS applications have been revised in this work. SERS has become a widely used technique for the detection of biological substances, including biomolecules (DNA and proteins) and cancer cells [58-60]. Another important application of SERS is detecting highly toxic molecules, such as chemical warfare agents and dangerous industrial chemicals [61]. Recently, Granger *et al.*, has reviewed the tremendous impact of SERS in pathogen diagnostics both in a traditional clinical setting and in the point of care (POC) arena [62]. SERS high sensitivity has also been demonstrated by several research groups in the detection of pathogenic bacteria, such as Salmonella and Listeria [63] and [64]. Single molecule identification and detection arguably represents the ultimate limit in biochemical analyses, and as a single molecule tool SERS offers exciting possibilities compared to traditional fluorescence, which is often applied in single molecule research [65]. Over the past decade, there has been considerable interest in SERS single molecule detection of biomolecules such as hemoglobin, glucose, biological toxins and viruses [66-68].

2.5.1 SERS mechanism

SERS was discovered in 1974 by Fleischmann *et al.*, who observed an intense Raman signal from adsorbed pyridine on a roughened silver electrode surface in aqueous solution [69]. The abnormally strong signal was first attributed to the increased surface area allowing more pyridine molecules to be adsorbed. However, in 1977, Van Duyne [70] and Creighton [71] independently stated that

the observed effect could not be accounted for the increased surface area, and proposed that Raman enhancement occurred in the adsorbed state. Two primary theories have been developed to explain SERS. Jeanmaire and Van Duyne first suggested an electric field enhancement mechanism generated by strong interactions of analyte molecules with the surface plasmon field, while Albrecht and Creighton proposed a chemical enhancement from the interaction between a molecule and the metal surface. SERS research has accelerated since the early 1980s with respect to chemistry, physics and engineering. And though its two mechanisms have been extensively investigated, some questions still remain.

Electromagnetic enhancement is the major contributor to SERS, and can give up to a 10^{14} enhancement from the excitation of surface plasmons in a metal nanostructure [72]. As shown in Figure 2.13, surface plasmons are collective oscillations of conduction electrons on the nanosphere, and excitation of the plasmons leads to the enhancement of the local field experienced by an adsorbed molecule [73]. The enhancement of the Raman scattered light intensity is highly localized, and decays rapidly as the distance between the analyte and metal surface increases. Thus, SERS is a surface-sensitive phenomenon.

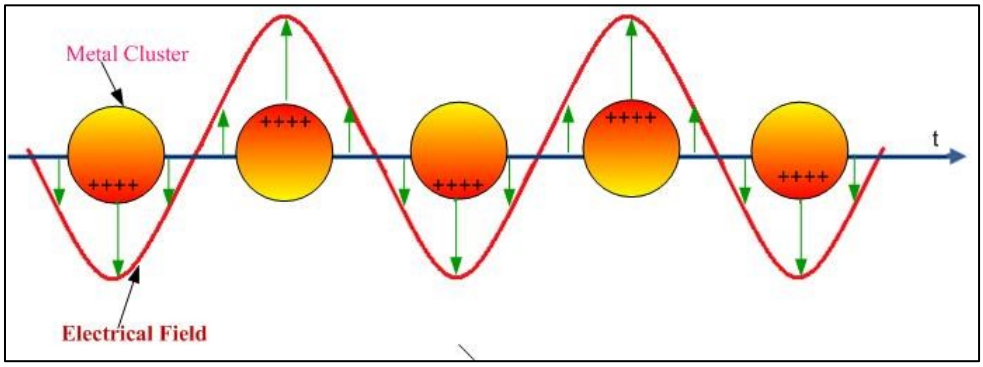

Figure 2-13 Schematic illustration of surface plasmon on a metal nanosphere (Courtesy: “Application of Surface Plasmon Resonance (SPR) Based on a Metal Nanoparticle” [73])

As discussed, the EM mechanism enhancement is due to surface plasmon resonance produced near the nanoparticle and the molecule of interest. Free electron charges of metallic nanoparticles respond to external electromagnetic fields (laser light), and oscillate at resonance wavelengths.

Localized surface plasmon resonance (LSPR) depends on the optical properties of metallic nanoparticles, which are described by a complex dielectric constant (ε) or a complex refractive index ($m=\sqrt{\varepsilon}$):

$$\epsilon(\lambda) = \epsilon_r(\lambda) + i\epsilon_i(\lambda) \tag{2.21}$$

$$m = n + ik \tag{2.22}$$

where *n* is the refractive index and *k* is the absorption coefficient of the nanoparticles. LSPR is also governed by the wavelength of incident light due to the wavelength dependency of the dielectric constant of nanoparticles. Maxwell's equations for a metallic sphere in the presence of an external field prove that LSPR can be viewed when the nanoparticle diameter (d) is much smaller than the laser light ($d \ll \lambda$). In this case, the electric field of the light can be considered uniform and electrostatic equations can be solved. Maxwell's equations for a spheroid metallic particle lead to an expression for the extinction $E(\lambda)$ (the sum of absorption and scattering) of a nanoparticle:

$$E(\lambda) \propto \frac{\epsilon_i(\lambda)}{(\epsilon_r(\lambda)+\chi\epsilon_{med})^2+\epsilon_i(\lambda)^2} \tag{2.23}$$

This relation shows that the electric field depends on the dielectric constants of nanoparticles. The three metals (i.e. silver, gold and copper) and their diverse optical constants produce different enhancements. For example, silver nanoparticles are more efficient than gold by factors of 10 to 100 [74].

Another mechanism, chemical enhancement, should be considered in SERS research, as it can contribute an enhancement factor of up to 10^2. This effect arises from the interaction between a molecule and the metal surface [75]. One explanation is that the metal-adsorbate proximity causes electronic coupling in resonant intermediate states via a charge-transfer mechanism, thus enhancing Raman scattering. Another possibility is that the molecular orbitals of the adsorbate expand into the conducting electrons of the metal, altering the analyte's chemistry. Chemical enhancement is independent of metal nanostructure, but it does depend on the chemical nature or structure of the analyte molecule. In most cases, electromagnetic and chemical contributions coexist, though the 10^{14} electromagnetic enhancement factor is typically reported only for single molecule measurements. While there is a consensus on the existence and nature of chemical enhancement, the magnitude remains unclear. For example, recent numerical and experimental results suggest possible contributions from chemical enhancement as high as 10^5 to 10^7 [76,77].

2.5.2 HC-PCF integrated with nanoparticles

Here we review the integration of HC-PCF with nanoparticles to achieve SERS. In most studies, rhodamine was used as the molecule of interest, as it is well-known and has proven effective for proof-of-concept experiments, particularly in molecular and fluorescence experiments. Rhodamine belongs to a family of fluorine dyes used extensively in biotechnology applications such as fluorescence microscopy, flow cytometry and the detection of analytes. Two techniques are typically used to prove the detection efficiency of rhodamine: fluorescence based and SERS. One demonstration used HC-PCF to excite and detect the fluorescence of a R6G dye gelatin sample, and showed enhanced detection efficiency. Another demonstration subjected a highly sensitive gold coated side-polished PCF to the excitation of surface plasmon resonance technology, and the plasmonic fluorescence emission of Rhodamine B using PCF was also enhanced [78].

Yan *et al*. presented an HC-PCF probe with a layer of gold nanoparticles (GNPs) coating the inner wall of the air holes [79]. The sample solution entered the air holes due to the capillary effect, and was then dried with a heating procedure. The excitation light was coupled to one end of the fiber, and the substrate and sample to the other end. HC-PCF guiding at 800 nm (empty) was used to guide a laser at 785 nm wavelength when filled with the sample [80]. However, the photonic band gap (i.e. transmission wavelength) of the sample filled HC-PCF shifted significantly compared to the empty HC-PCF, and the shifted transmission wavelength did not match the excitation wavelength. Thus, light was guided into the HC-PCF weakly and was not totally confined to the sample-filled core region, which resulted in weak light-matter interaction.

In another demonstration, an HC-PCF was used as a SERS probe by coating the inner wall of the core and cladding with AgNPs, and non-selectively filling the sample into HC-PCFs [81]. In this approach, R6G was the analyte molecule, and two types of silver nanoparticles were used as double SERS substrates. The inner wall coated with the second layer of the substrate exhibited higher sensitivity than the one with single substrate layer. Han *et al*. showed SERS measurement in HC-PCF by functionalizing AgNPs in both a hollow and solid core PCF [82]. They found that the combination of a liquid core HC-PCF and SERS was a sensitive platform for detecting and monitoring R6G. Irizar *et al*. selectively filled an HC-PCF core, and obtained enhancement in the Raman signal to study different stages in the synthesis of nanoparticles [83].

The non-selective filling approach was used by Gu's group to demonstrate various samples, such as R6G, human insulin and tryptophan (concentrations in the range of 10^{-10} M) [84]. Cox *et al*. used kagome lattice HC-PCF to detect Rhodamine 6G at a concentration of 210 nM with SERS [85]. Dinish *et al*. demonstrated a practical approach to detect cancer cells, using an ultrasensitive platform for the multiplex detection of cancer biomarkers by combining the SERS technique with HCPCF [86]. The biomarkers were immobilized in the HCPCF using antibody-conjugated SERS-active nanoparticles (SERS nanotags). As proof-of-concept for targeted

multiplex detection, hepatocellular carcinoma (HCC) biomarkers, alpha fetoprotein (AFP) and alpha-1-antitrypsin (A1AT) were simultaneously detected successfully using HC-PCF and SERS. Recently, Calcerrada *et al.*, has comprehensively reviewed sensing application of HC-PCF including SERS in the last decade [87]. Gong et al., demonstrated HC-PCF SERS platform to accurately monitor lipid peroxidation derived protein modifications in cells. The demonstrated method uses HepG2 liver cancer cells treated with linoleamide alkyne (LAA) and different concentrations of CH. Upon lipid peroxidation, LAA is oxidized in cells with alkyne group. By measuring the signature Raman peak of the alkyne group, lipid peroxidation state was successfully monitored [88].

Chapter 3. HC-PCF as biosensing tool for monitoring bio-chemicals

3.1 Introduction

This chapter explores the feasibility of using hollow core optical fiber and Raman spectroscopy for real time monitoring of clinically relevant molecules. The optical design configuration involves a 785 nm laser diode coupled into a hollow core optical fiber filled with ethanol. Of all the hollow core optical fibers considered, enhancement with HC-PCF was more than 90 times greater that of bulk samples in cuvettes; thus, HC-PCF was chosen as the 'Raman signal enhancer'. Heparin, a highly important blood anti-coagulant requiring precise monitoring and control for patients undergoing cardiac surgery and dialysis, was used as the sample to prove HC-PCF sensor capabilities. The method of heparin monitoring presented here is a novel and improved alternative to existing clinical procedures, in terms of accuracy, response time and sample volume. This technique has the potential to be a 'generic biosensing tool' for diagnosing a wide range of biological samples.

The chapter begins with an evaluation of different hollow core optical fiber configurations for enhancing Raman signals, followed by optimization of the Raman setup and experimental configuration. As discussed in Section 3.2, various chemicals were analyzed using HC-PCF and Raman spectroscopy. In the next section we examine different methods to monitor heparin concentration and the optical characterization of sample mixtures (heparin-serum). The spectral results and analysis are presented in the section 3.4.

3.1.1 Comparative study of hollow core optical fibers (HC-OF)

Various types of hollow core optical fibers (HC-OF) were evaluated to determine their capability to enhance Raman signals and support strong modal field interaction with the analyte of interest. This procedure is necessary to obtain high quality Raman signals from micro-litre volumes of samples in clinical diagnosis. Four kinds of hollow core optical fibers were evaluated: glass (capillaries), Teflon, hollow core silica wave guides (HSW) and hollow core photonic crystal fibers (HC-PCF).

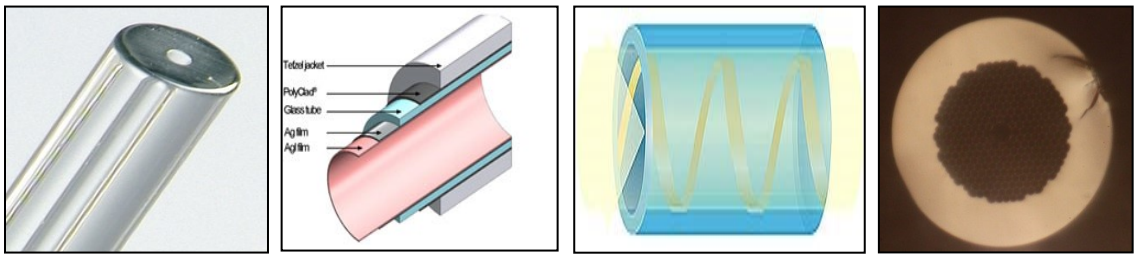

(a) (b) (c) (d)

Figure 3-1 Different types of hollow core optical fibers
(a) glass capillaries (Fiber Optic Center Inc.), (b) Teflon (Biogeneral Inc.), (c) hollow core silica wave guides (HSW) (Polymicro Technologies) and (d) hollow core photonic crystal fibers (HC-PCF) (NKT Photonics)

The theoretical evaluations of the figure of merit for hollow core optical fibers were presented in Chapter 2. Here, we experimentally evaluate the Raman signal enhancement achieved by different hollow core optical fibers using a fixed length of 8cm, and determined the losses in each case. Figure 3-2 shows the Raman spectra of ethanol in different HC-OF, and their enhancement (calculated at the Raman peak ~880 cm^{-1} corresponding to the C-O-C symmetrical stretch mode) with respect to a bulk ethanol sample in a cuvette [89]. In practice, the enhancement factor is less than the theoretical value, due to losses in the coupling of the excitation light to the fiber, material and waveguide loss, and single mode transmission throughout the length of the fiber.

The enhancement effect in all HC-OF platforms is mainly due to its use as a waveguide to confine both the liquid and the optical field over a long distance, in order to obtain a larger light-matter interaction length. As a result, Raman scattering can be efficiently excited along the fiber's entire length, and the Raman modes are guided by the fiber and can be collected with the same waveguide. Of all the HC-OF tested, we found that HC-PCF provided >30% better coupling efficiency in single mode operation. In HC-PCF, the mode overlap between the sample and excitation light is >99% with propagation loss of <1 dB/m, compared to other HC-OF where losses are >10 dB/m. The enhancement of the Raman signal with HC-PCF was >90 times better than the bulk cuvette technique, and in agreement with the results reported by Altkorn *et al*. and Eftekhari *et al.* [23,90]. Therefore, HC-PCF was chosen for screening samples throughout this thesis.

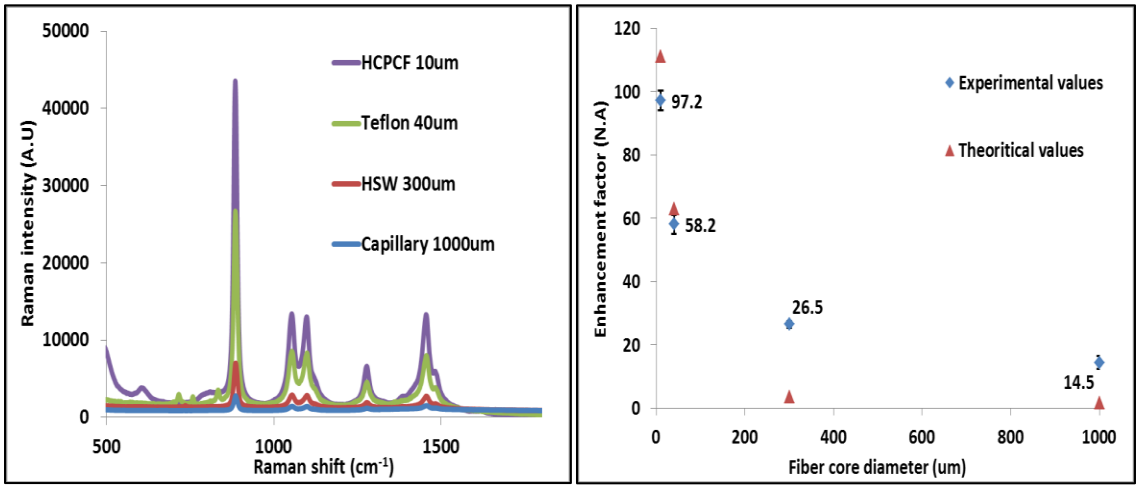

(a) (b)

Figure 3-2 (a) Raman signal of ethanol with different hollow core optical fibers (HC-OF) and (b) the enhancement factor with different HC-OF

3.1.2 Optimization of Raman setup

Once the HC-PCF that provides the maximum enhancement was determined, we focused on optimizing the Raman setup with respect to geometry and coupling lenses. We used ethanol as the analyte, as it produces a strong Raman signal. To optimize the setup we recorded the Raman signal of the analyte in forward and backward configurations. The geometry is shown in Figure 3-3.

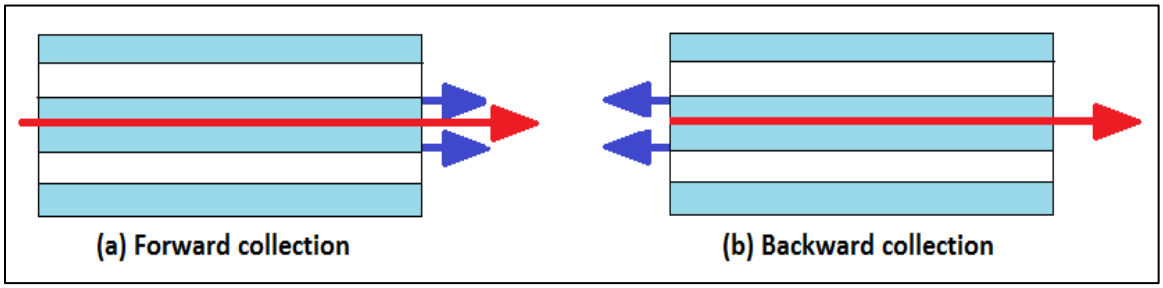

Figure 3-3 Raman collection geometry (a) forward (b) backward

Theoretically, a Raman signal collected in the forward direction is $P_{fwd} = Le^{-\alpha L}$, and in the backward configuration it is $P_{bkwd} = \frac{1}{2\alpha}[e^{-2\alpha L} - 1]$[21] where α is the loss of the fiber. Several important conclusions can be drawn from the method of power collection. Backward collection efficiency in an HC-PCF with finite loss is more efficient than forward collection, because the pump light is strongest at the input end when it enters the fiber. Thus, the strongest Raman signals are generated at the end closest to the pump-light entrance. Due to transmission loss, the strength of the differentially-generated Raman signal decreases when moving toward the back-end of the waveguide. The Raman light that is produced near the front (pump-input) end of the waveguide and travels in the backward-wave direction, experiences no loss as it exits the guide directly. The Stokes light emitted near the back-end (pump output) has loss over the entire length as it travels back through the waveguide for collection. In the forward-scattering direction the largest Stokes signal has the most loss, as it travels the length of the waveguide before exiting. The smaller portion of the Stokes signal generated near the back-end of the waveguide has the least loss, as it exits directly. Thus, investigation in both configurations determined that backward configuration yields a Raman signal that is at least two times more efficient, as shown in Figure 3-4.

Effort was then focused on selecting the microscope objective lens that matches the numerical aperture (NA) of the filled HC-PCF fiber. The NA can be described in terms of the refractive index contrast between the core and the cladding, as

$\sqrt{(n_{core}^{eff})^2 - (n_{clad}^{eff})^2}$. In order to match the NA of the lens with the filled HC-PCF, the Raman spectra of ethanol filled HC-PCF with different lens NA (0.07, 0.25 and 0.65) were recorded; the results are shown in Figure 3.4. It was determined that the lens with NA=0.65 and f=4.5mm yields the best Raman signal, because the NA of HC-PCF is considerably larger when it is filled with liquid samples. Due to the complex periodic voids in the cladding of HC-PCFs, defining n_{clad}^{eff} is not straightforward. Several methods have been developed to do this, including a fully analytical vectorial approach, as discussed by Midrio *et al.* [91]. From the simulation results discussed in Section 2.4, we calculated$(n_{core}^{eff})^2 = 1.838$, while $(n_{clad}^{eff})^2 = 1.39$ was obtained from Midrio *et al.* These resulted in an NA of 0.67, and hence lens with NA=0.65 was used for all the experiments discussed in this thesis.

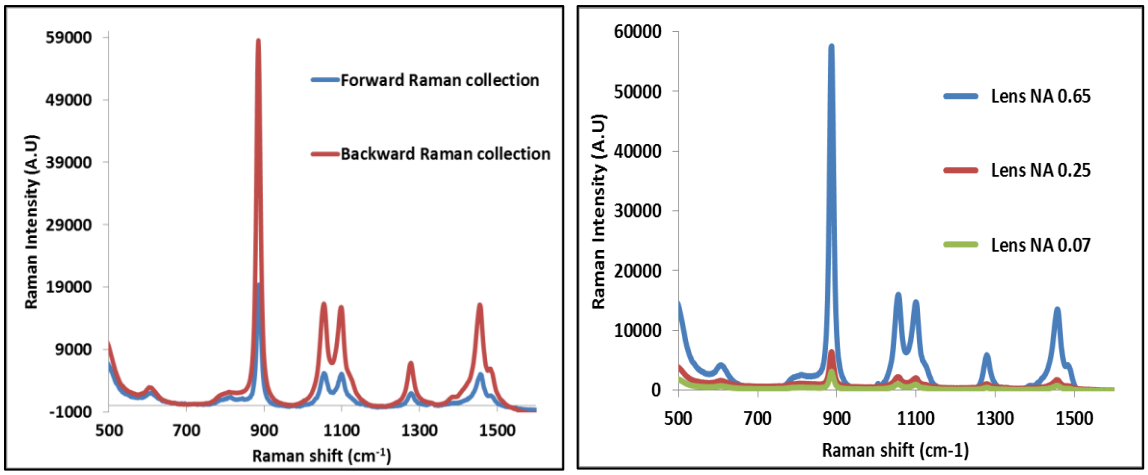

(a) (b)

Figure 3-4 Raman spectra in different configuration

(a) Raman spectra of ethanol in HC-PCF backward and forward geometry. (b) Raman spectra of ethanol in HC-PCF with different coupling lens

3.1.3 Experimental configuration

A schematic of the experimental setup is presented in Figure 3-5. A single mode 100mW, 14 pin butterfly pin laser was acquired from Innovative Photonic Solutions (I0785SB0100B), and coupled to the HC-PCF. The laser beam passed through a

band pass filter (BP) centered at 785 nm (+/- 2 nm) to filter out other wavelength components near 785 nm from the laser diode. The beam was directed through a dichroic filter (R785RDC, Chroma Technologies Corp.), which reflected 785 nm (+/-5 nm) at an angle of 45^0, transmitted 790-1000 nm band, then further focused on the tip of the HC-PCF with a 40x microscopic objective lens (L1) with an NA of ~0.65. The channels of the fiber were filled from a reservoir, as explained in Section 2.3, and the light coupling efficiency for the sample filled HC-PCF was ~30%. Furthermore, the dichroic filter acted as a high pass filter for the light scattered backward from the sample-filled HC-PCF, and allowed only the Raman wavelength to pass through. The filtered Raman light was then imaged onto a fiber bundle (Fiberoptic System Inc., 26 multimode fiber, NA=0.22) by a 6.3x microscopic objective lens (L2) with an NA of ~0.20. The output of the fiber bundle was interfaced with a Kaiser f/18i Spectrograph using a TE-cooled Andor CCD camera. Andor SOLIS software was used for spectral data acquisition, and the spectra were monitored on the data acquisition computer. This well-optimized, self-configured optical configuration achieved high signal-to-noise Raman signals from the samples.

The high laser light power density in the HC-PCF causes the filled sample to evaporate, which creates air gaps or non-uniform sample distribution in the HC-PCF channels. Under these circumstances light is partially guided within the HC-PCF, leading to an overall decline in the Raman signal of the chemical of interest. Therefore, an in-house, aluminum-based sample reservoir was designed to continuously replenish the heparin-serum mixture sample in the HC-PCF channels, as shown in Figure 3.6. The reservoir was mounted on a XYZ translation stage (Thorlabs Inc.). One end was sealed with a glass slide and water resistant epoxy, while the other was used for HC-PCF fiber insertion. The fiber was fixed in place with a Teflon tube and Swagelok connectors.

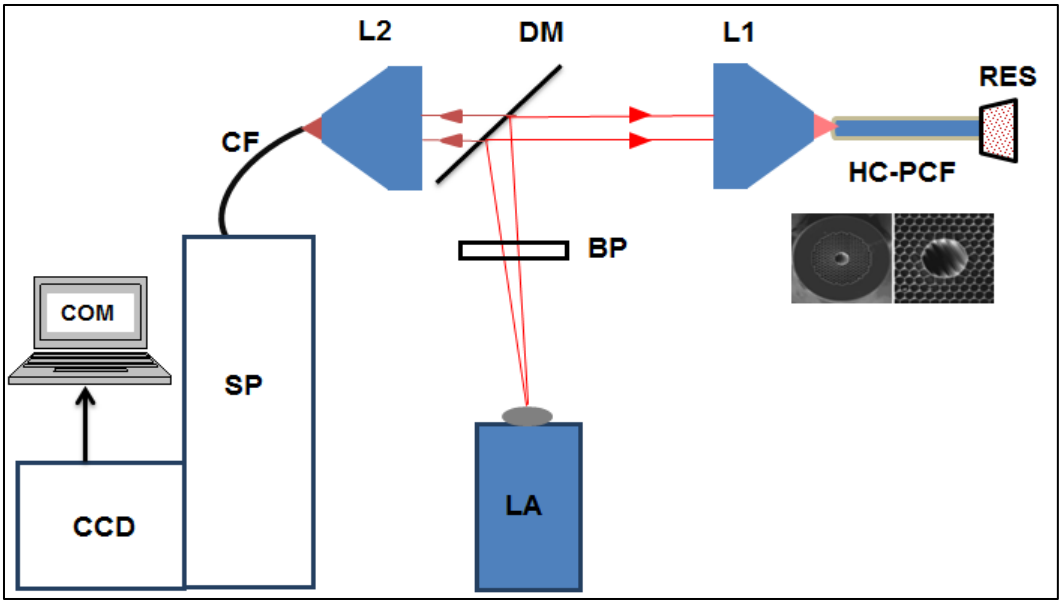

Figure 3-5 Schematic of the HC-PCF setup.

LA represents the Laser; BP the band pass filter; DM the dichroic mirror; L1 the microscope objective lens for light coupling; HC-PCF the hollow core photonic crystal fiber; RES the reservoir; L2 the microscope objective lens for backward light collection; CF the collection fiber; SP the spectrograph; CCD the CCD camera; and COM the computer.

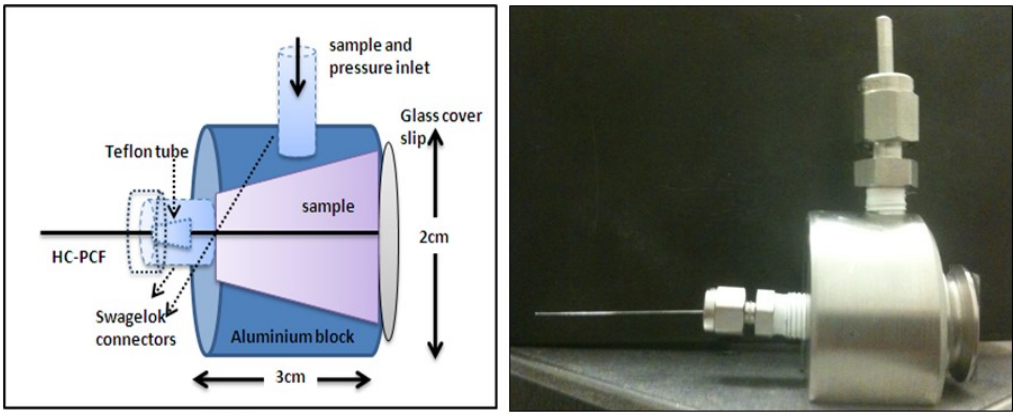

Figure 3-6 (a) Design of the reservoir for HC-PCF fiber (b) reservoir with the HC-PCF fiber

Manual filling of the HC-PCF with sample solution was accomplished as follows: First, a collection of sample solution in a clinical syringe was connected to the

reservoir inlet with a Teflon tube (length ~6 cm). Then, using the syringe, the sample solution was transferred to the reservoir until it was filled to capacity. The light guiding end of HC-PCF was examined under the microscope to cross-validate the complete loading of the HC-PCF with the sample. After a few iterations of the filling procedure, the optimal pressure on the syringe piston to prevent the sample solution from leaking out of the light guiding end of the HC-PCF was qualitatively determined. Thus, the light was coupled to the sample filled HC-PCF efficiently, and unaffected by the formation of sample droplets at the light guiding end of the HC-PCF.

3.2 HC-PCF for detecting bioanlytes

Rapid and accurate detection of analytes in small concentrations (e.g. proteins, pathological markers, toxins) is critical in fields such as medical diagnosis, environmental monitoring and quality control in the food industry. The use of HC-PCF as a sensor offers many recognised benefits (e.g. size, cost, light path control, small volume consumption, ease of use). HC-PCF sensors can be inserted into the media to be sensed, rather than requiring that samples be inside an instrument. This can be done with either a hand-held probe, or a set of remotely operated devices, for applications such as environmental monitoring.

To this end, various biochemicals, including lactic acid, urea, creatinine, ascorbic acid and heparin, were evaluated. Lactic acid is one of the significant metabolites in blood, and is accumulated intercellularly when tissues do not have sufficient oxygen to support the aerobic oxidation of glucose [92]. Urea and creatinine are the two most important biochemicals monitored for kidney patients [93,182]. Monitoring creatinine, a molecule which is a waste product of the liberation of adenosine triphosphate (ATP) from phosphocreatine in skeletal muscles, is regarded as the most useful way to determine the efficiency of the kidneys, and to diagnose renal failure.

Figure 3-7 shows the Raman spectra of biochemicals exhibiting Raman peaks: for urea it was 1001 cm^{-1} of C-N symmetrical stretching, for lactic acid 830 cm^{-1} of C-COOH, for ascorbic acid (vitamin C) 820 cm^{-1} of C=C ring-stretching, and for heparin ~1005 cm^{-1} of C-N stretching [94-95, 182]. Through discussions with physicians at the University of Ottawa Heart Institute, it was determined that the potential for life threating complications due to difficulty and errors is highest when monitoring heparin. Thus, this research focused on developing a better, faster and more efficient way of monitoring heparin during surgery, using HC-PCF and Raman spectroscopy.

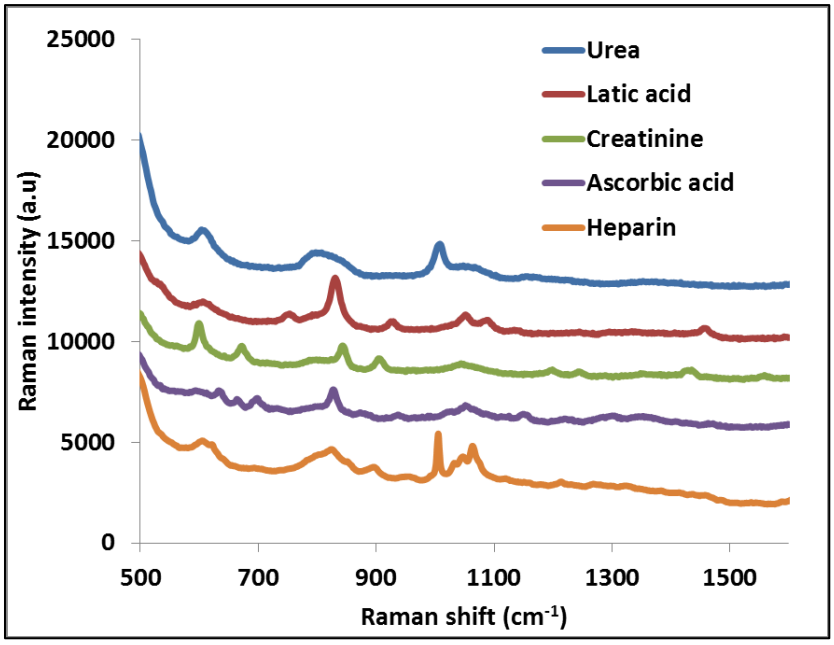

Figure 3-7 (a) Raman spectra of different biochemicals in HC-PCF

3.3 Heparin monitoring review

Heparin is a blood anti-coagulant that, uncontrolled, can pose life-threatening risks to patients undergoing surgery. Thus, it is crucial that physicians are able to rapidly monitor the amount of heparin in blood with utmost precision. The conventional methods used to quantify heparin levels in surgical environments include activated clotting time (ACT), Anti-Xa and activated partial thromboplastin time (APTT) [96-99], and, of these, ACT has been the most commonly used. ACT is a measure of

the anticoagulation effects of heparin, obtained by determining the time for blood with heparin to clot when induced by activators. However, due to the slow response time and qualitative nature of heparin, faster and more accurate methods are required [99,100]. Such techniques must not only be capable of real-time, quantitative heparin monitoring, but also use minimal amounts of a patient's blood.

In-lab techniques for monitoring heparin are as follows: Szelka *et al*. demonstrated an optical method of quantifying heparin in serum samples. It involves detection and neutralisation of heparin by a fluorescent ruthenium compound, which is applicable to the quantification of heparin by monitoring 630 nm fluorescence [101]. In a recent study, "heparin red" fluorescent probe assay that emits 615 nm was used for the direct and sensitive detection of heparin in plasma, independent of any anticoagulant activity [102]. Surface plasmon resonance (SPR) was demonstrated for monitoring heparin by Gaus *et al*. They modified gold films with protamine, which interacts electrostatically with heparin, and determined the absolute concentration of heparin depending on the adsorption. The 'thickness' of the immobilized protamine layer gives the linear range of the sensor's response and its sensitivity [103].

A silicon field-effect sensor for the direct detection of heparin in a phosphate buffer solution (PBS) was also developed by Milovic *et al.* [104]. This sensor consists of a simple, micro fabricated electrolyte-insulator-silicon structure, encapsulated in microfluidic channels. The clinical heparin antagonist protamine, or the physiological partner antithrombin III, was used as heparin-specific surface probes [104]. Ramamurthy *et al.* proposed an improved protamine-sensitive electrode for monitoring heparin concentrations in whole blood, based on a polymeric membrane doped with the charged ion exchanger dinonylnaphthalenesulfonate (DNNS). The electrode exhibited significant non-equilibrium potentiometric responses to polycationic protamine over different concentration ranges of heparin in undiluted whole-blood samples. This sensor was compared with other protamine titration-based methods, including the commercial Hepcon HMS assay and the commercial chromogenic anti-Xa heparin assay, with corresponding plasma

samples [105]. Wang *et al.*, demonstrated a photoacoustic imaging technique to monitor heparin concentration using methylene blue as a simple and Federal Drug Administration-approved contrast agent. The study was also used to create a nanoparticle-based hybrid material that can immobilize methylene blue for potential applications as a wearable/implantable heparin sensor to maintain drug levels in the therapeutic window [106].

Though the above in-lab methods were capable of monitoring heparin, they required indirect detection with heparin probes such as protamine or synthetic cationic polymers. Moreover, they are complicated and based on surface affinity capture or automated heparin protamine titration, which limits the system's sensitivity to lower concentrations of heparin in blood. In addition, the accuracy of such methods depends on the cross reaction of heparin with the labeling agent, which could give false results. Due to these drawbacks, we combined Raman spectroscopy with a hollow core photonic crystal fiber (HC-PCF) to monitor heparin in blood-derived serum.

This present research builds on our previous work that involved HC-PCF-based sensing platform [107,108]. The novelty of the current work is the stronger sensing potential of HC-PCF to detect a weak Raman scatterer (like heparin), which is difficult to detect in a complex biological material, such as serum. It is achieved by exploiting the photonic band gap property of HC-PCF, and efficient collection of the Raman signal. This is the first case of monitoring a clinically important molecule in serum with an HC-PCF-based Raman sensor.

The high sensitivity, accuracy and minimal test sample volume requirements (microlitre) make this new optical sensing scheme an attractive candidate for heparin monitoring in clinical settings. Furthermore, as Raman spectroscopy has an inherent advantage of molecular specificity, it is more appropriate for clinical diagnosis where sample screening is performed on body fluids (e.g. blood, serum) characterized by multi-species biological components.

3.3.1 Samples and their refractive index measurement

MiniHep was purchased from Leo Pharmaceuticals in a vial of 25,000 USP/ml concentrations. USP stands for United States Pharmacopeia, and denotes the potency of a drug in clinical applications. Blood samples were obtained from a local bovine slaughterhouse, and serum was extracted by centrifuging the blood at 2,000 rpm for 30 minutes. Various concentrations of heparin in serum with a total volume of 2 ml were accurately prepared.

As mentioned in Sec 2.4, the light guiding property of HC-PCF depends on the refractive index, which is related to the concentration of the sample mixture. The in-lab refractive index values of heparin-serum mixtures needed to be determined experimentally, because they were only available for the individual constituents (heparin and serum), not for mixtures with varying volume ratios. The refractive index values, shown in the second column of Table 3.1, were determined from a Reichert AR200 Digital Handheld Refractometer that measured the refractive index of heparin-serum mixtures at a wavelength of 588 nm. Ideally, the refractive index values of the sample(s) in the HC-PCF must be measured at the excitation light wavelength (785 nm in our case) to calculate the HC-PCF transmission band. However, the choice of refractometer depended on availability. Moreover, the sample refractive index values measured at the wavelength of 588 nm was believed to be comparable to those measured at 785 nm. For example, the refractive index of one of the sample mixtures (with heparin concentration in serum ~0.5 [vol./vol.]) was found to be 1.3509.

Sample	**Refractive Index**	**HC-1550-04 transmission band (nm)**
Air	1.0000	1430-1610
Water	1.3333	776-884
Serum	1.3486	725-816

Heparin-serum mixture (ratio 1:1)	1.3509	717-808
Heparin	1.3528	710-800

Table 3-1: Refractive Index of samples

3.4 Results and Discussions

3.4.1 HC-PCF for heparin monitoring

The objective of our study was to monitor the concentration of heparin in serum, using HC-PCF and Raman spectroscopy. The initial phase focused on recording the Raman spectrum of pure heparin in a cuvette, with an IR-785 nm light as the excitation source. The Raman spectrum of heparin was found to be similar to that reported previously by Atha *et al.* [109]. The choice of 785 nm for excitation was clear, due to the minimal absorption of blood/serum in the NIR wavelength region. The Raman peak of heparin of approximately 1,005 cm^{-1} was considered suitable for quantifying heparin in serum. The sample mixtures were prepared with different concentration ratios of heparin and serum, and it was soon determined that the Raman spectra of heparin-serum mixtures had Raman peaks of heparin with poor signal-to-noise ratios. This is because the spectral background of the serum and silica completely dominated the Raman signal of heparin. The challenge then was to enhance the Raman signal of heparin and filter out the spectral background of the serum, to improve the detection sensitivity.

To evaluate the potential of HC-PCF as a 'Raman signal enhancer', it was first filled with pure heparin and carefully monitored microscopically. Figures 3-8 (a) and (b) show the microscopic view of empty and heparin filled HC-PCF. The brighter patches in cross sectional view (b) indicate that almost all the micro-channels are filled with heparin, while the few dark spots are unfilled or partially filled channels. The fiber was then carefully inserted into a reservoir, as shown in Figure 3-6 (b). A reservoir at one end of the fiber was required to manage evaporation of the samples inside the fiber channels, which can consequently

affect light guidance within the fiber. The fiber was then mounted on a 5-axis flexure stage (Thorlabs Inc.), and the experimental set-up was optimized with respect to maximum light coupling efficiency (~30%) within the HC-PCF.

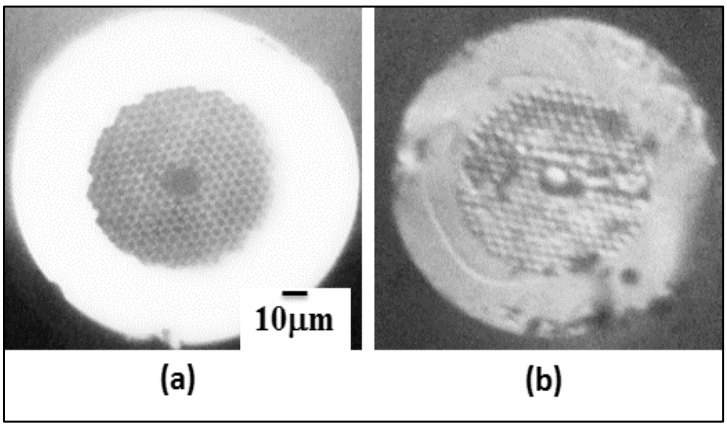

Figure 3-8 Cross-sectional view of HC-1550-04 when (a) empty (b) filled with heparin.

3.4.2 Polynomial background subtraction

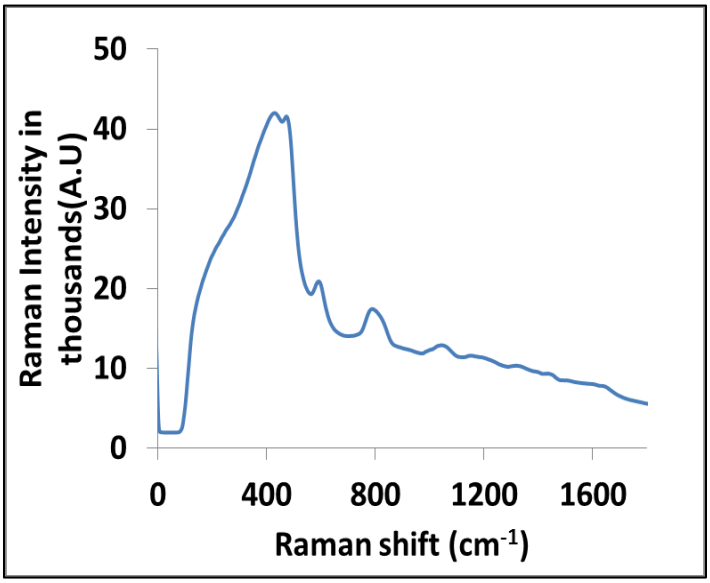

Figure 3-9 Raman spectra of serum in HC-PCF

As a first step, Raman spectra of serum in HC-PCF were recorded which is shown in Figure 3-9. Largely due to the serum, the Raman spectra of heparin and serum mixtures exhibited strong spectral backgrounds. These were fitted to a third-order

polynomial and subtracted from the spectra, as shown in Figure 3-10 (a) and (b). For post processing the data we selected a range of 900 to 1,150 cm^{-1}, as this had prominent Raman peaks of heparin that could be used for quantifying heparin in serum. Similar data processing was applied to filter out the Raman peaks of heparin from the spectral data of the heparin-serum mixtures in subsequent steps.

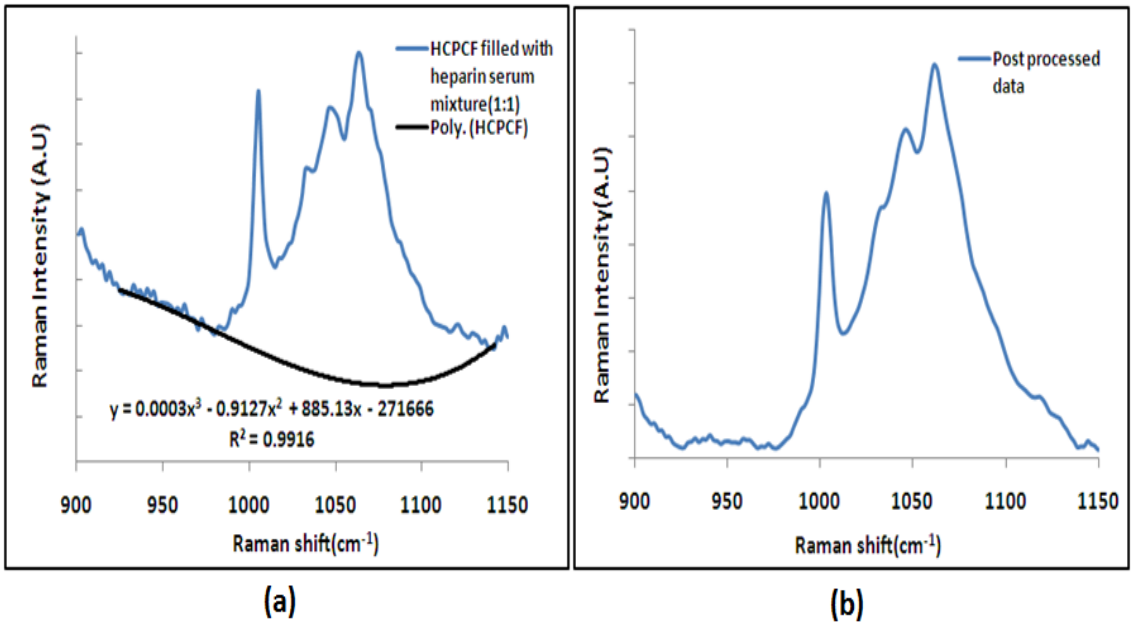

Figure 3-10 Polynomial background subtraction

(a) Pre-processed Raman spectra of heparin serum mixture in HC-PCF with a third-order polynomial fit, and (b) post processed data after polynomial subtraction

3.4.3 Raman signal enhancement of heparin-serum mixture in HC-PCF

We recorded the Raman spectra of 1:1 sample mixtures of heparin-serum in different lengths of HC-PCF. The major challenges were to maintain the same power of light, and to ensure homogeneous distribution of the sample mixture in different lengths of HC-PCF. Figure 3-11 (a) shows the gradual increase in the intensity of the Raman peaks of heparin (within the wave number range of 910 to 1,120 cm^{-1}) as the length of HC-PCF increases from 3 to 10 cm at a regular interval of 1 cm. For clarity, only three Raman spectra at 3, 6 and 9 cm lengths are shown in Figure 3-11 (a). The peak Raman intensity of heparin of approximately 1,005 cm^{-1} was calculated for different lengths of HC-PCF. Figure 3-11 (a) also

shows the Raman signal of 1:1 heparin-serum in bulk (i.e. cuvette), which is weak compared to that from a sample-filled HC-PCF. In conventional cuvette-based Raman spectroscopy, the maximum Raman light is generated at the focal point of the beam in the sample. The focal point is where the laser light strongly overlaps/confines the sample. A similar condition of strong light-sample interaction is achievable along the entire length of the sample-filled HC-PCFs, due to their capability to strongly confine light via the photonic bandgap. Hence, samples in HC-PCFs give several orders of magnitude higher Raman signals than samples in a cuvette, which means that HC-PCFs can act as a Raman signal enhancer. An enhancement factor of the ratio of the Raman signal obtained from HC-PCF to that from a cuvette was determined for different lengths of HC-PCF. Finally, a calibration curve of enhancement factors versus HC-PCF lengths was calculated, as shown in Figure 3-11 (b). It is notable that this comparison takes similar throughput sample power into account, while leaving other experimental parameters unchanged.

Based on these results, two points can be considered valid: The enhancement factor is directly proportional to the sample volume in the core region, which is ultimately related to the HC-PCF length. And the enhancement factor increases linearly according to the HC-PCF length in the range of 3 to 8 cm, and tends to saturate with longer HC-PCF lengths. There are a number of reasons for the saturation of the Raman signal of heparin (or enhancement factor) beyond a certain length of HC-PCF such as 8 cm, including light absorption, viscosity, sample surface tension and fiber bend loss. Thus, the optimal HC-PCF length for heparin detection ranges from 5 to 8 cm. Figure 3-11 (b) shows the enhancement of ~90 times the Raman signal of heparin at ~1,005 cm^{-1} from the mixture in the HC-PCF, compared to that obtained from the cuvette. This demonstrates that HC-PCFs have inherent potential to enhance Raman signals, and that their length can be suitably optimized for sensitive detection of bio-analytes.

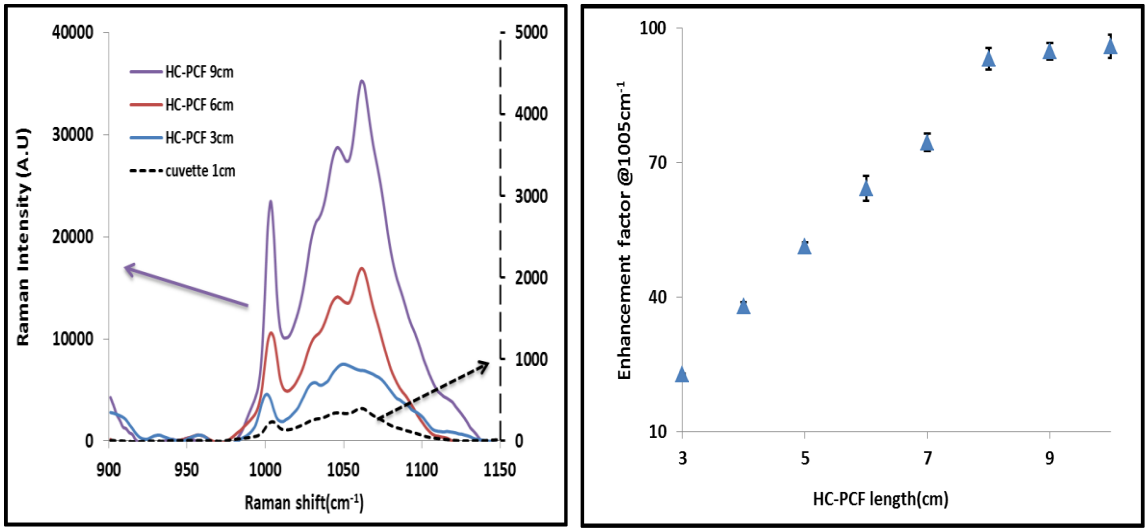

(a) (b)

Figure 3-11 Enhancement with different length of HC-PCF

(a) Different lengths of HC-1550-04 fiber filled with heparin-serum concentration, and (b) Enhancement curve for different lengths of fiber filled with heparin-serum concentration.

3.4.4 Raman spectra of heparin-serum mixtures

This research primarily focused on the quantitative measurement of heparin in sample mixtures of heparin and serum. A variety of sets of heparin-serum mixtures, with different ratios of heparin in the range of 12-20000 USP/ml, were prepared and injected into a 5 cm HC-PCF. This length was selected to obtain significant enhancement and avoid saturation effects. As shown in Figure 3-12 (a), the Raman spectra of the heparin-serum mixtures showed prominent Raman peaks in the spectral range of 900 to 1,070 cm^{-1}, which correlated well with the Raman bands of commercial-grade heparin found by Atha *et al.* [109]. The clinical-grade heparin employed in this study exhibited a well resolved Raman peak at 1,005 cm^{-1} (C-N stretching). The overlapped Raman bands due to symmetric SO_3 vibration were at ~1,035 cm^{-1} (N-SO_3 vibration), 1,045 cm^{-1} (6-O-SO_3 vibration) and 1,060 cm^{-1} (2-O-SO_3 vibration). Thus, the intensity of the Raman peak at ~1,005 cm^{-1} was the parameter used to evaluate the quantity of heparin in serum, and it varied with increased concentrations of heparin as shown in the inset of

Figure 3-12 (a). The spectral band intensity of the Raman peak of heparin at ~1,005 cm^{-1} was calculated for all sets of spectra corresponding to a particular concentration ratio of heparin and serum, and averaged to obtain a single data point. As a result, error due to fluctuations of the Raman peak intensity was minimized. Finally, a calibration curve of the averaged spectral band intensity of the Raman peak as a function of the corresponding percentage composition of heparin was produced, as shown in Figure 3-12(b).

The following conclusions were drawn from the experimental results. First, the HC-PCF based sensor system is capable of successfully monitoring the heparin concentration in a heparin-serum mixture. Second, the Raman peak intensity of heparin varies linearly according to the heparin concentration, which indicates that the sensor has high detection sensitivity over a broad range of concentrations, and can measure heparin concentration as low as 12 USP/ml in a serum sample mixture.

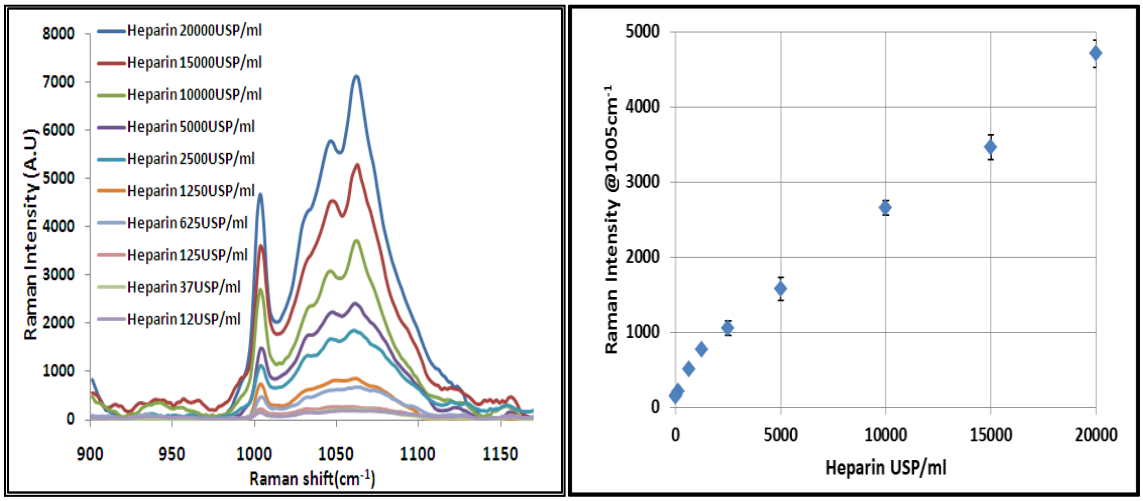

(a) (b)

Figure 3-12 Raman spectra of heparin-serum mixtures

(a) Different concentrations of heparin in serum filled in HC-1550-04 fiber, and (b) Raman peak intensity @1005cm^{-1} with different concentrations.

The predicted concentration of the replicate samples was used to estimate the linearity [110, 111]. Linearity is the capability of the method to show whether there

is proportionality between the predicted and nominal concentrations, within a specific range. This parameter was determined by constructing a curve from solutions of different concentrations. We calculated the curve slope (m), which determines the proportionality of the analytical function, the linear coefficient (h) and the correlation coefficient (r). The criterion for acceptance was r = 0.99.

As shown by the error bars on the calibration curve in Figure 3-12 (b), the intensity data points fluctuated minimally, further indicating a high degree of accuracy in the measurement. The linear calibration data for the heparin-serum mixture demonstrates that the HC-PCF-based Raman sensor has significant potential for qualitative and quantitative monitoring of heparin in serum.

The lowest concentration of heparin detected was 12USP/ml, which falls within the clinical detection range of heparin for patients during surgery. The reason that a weak Raman scatterer (such as heparin) can be detected at such low concentrations in a complex matrix is due to the HC-PCF, because it supports strong light-matter interaction. However, we are also exploring other methods to improve the detection limit of the HC-PCF-based sensor system. The inclusion of nanoparticles to further enhance the heparin Raman signal could be beneficial, though synthesizing nanoparticles that have an affinity for complex/bulky molecules (like heparin) and the robustness to retain their optical property in a serum environment will be challenging. Another method could be determining how to estimate the heparin concentration directly from blood samples rather than serum. Perhaps a porous membrane could be added to the sample reservoir, to filter the hemoglobin from the blood and allow only the heparin-serum solution to penetrate the HC-PCF micro-channels [112].

3.5 Conclusion

This work demonstrates using Raman spectroscopy and hollow core photonic crystal fibers to monitor the quantity of heparin in serum. It examines a simple procedure of filling the holes of HC-PCF with a sample mixture whose molecular constituents (heparin in this case) can be determined quantitatively by measuring

the corresponding Raman peak intensity. HC-PCF supported strong modal field overlap with the heparin-serum mixture, which resulted in ~90 times enhancement of the heparin Raman signal. Consequently, we were able to detect compositions of heparin in serum as low as 12 USP/ml. This detection technique has the benefit of high detection sensitivity with minimal sample volumes, as well as the molecular specificity capability of Raman spectroscopy. Hence, it is appropriate for clinical diagnoses requiring extraction of microlitre amounts of bodily fluids and precise assessment of the component(s).

Publications from this work:

P1. **A. Khetani**, V. S. Tiwari, A. Harb and H. Anis: "Monitoring of heparin concentration in serum by Raman spectroscopy within hollow core photonic crystal fiber." Optics Express 19, 15244-15254 (2011).

Novelty: The feasibility of using hollow core photonic crystal fiber (HC-PCF) in conjunction with Raman spectroscopy for real time monitoring of heparin concentration in serum is explored here. The novelty of the work is extending the strong sensing potential of HC-PCF in order to detect a weak Raman scatterer (like heparin), which is difficult in a complex biological material (such as serum). It is achieved by exploiting the photonic band gap property of HC-PCF, and efficient collection of the Raman signal. This is the first demonstration of monitoring a clinically important molecule in serum using an HC-PCF-based Raman sensor. Our method of monitoring heparin is a novel alternative to existing clinical procedures in terms of accuracy, response time and sample volume. Non-selectively filling HC-PCF creates a strong modal field overlap and, consequently, an enhanced Raman signal (>90 times) from HC-PCFs filled with various heparin-serum mixtures, compared to the bulk counterpart (cuvette). This method has the potential to become a generic biosensing tool for diagnosing a wide range of biological samples.

Chapter 4. HC-PCF as a robust Raman biosensor

4.1 Introduction

This chapter demonstrates a method that enables HC-PCF to be used for repetitive characterization of multiple samples by Raman spectroscopy. It was achieved by integrating HC-PCF with a differential pressure system, to allow effective filling, draining and refilling of samples into an HC-PCF under identical optical conditions. As a result, high-quality, reliable spectral data suitable for multivariate analysis (partial least squares (PLS)) were acquired. With this method, we can accurately predict different concentrations of heparin and adenosine in serum, which could lead to the adoption of HC-PCFs for point-of-care technologies and environmental monitoring, where rapid sample characterization is crucial.

The chapter begins with the challenges with HC-PCF. In section 4.2, we propose a layout with an 'H' shaped differential pressure system common to microelectromechanical systems (MEMS) microfluidic flow control [113], and benchmarked it using ethanol. Subsequent sections summarize our findings with respect to optimal pressure difference, sample filling time into HC-PCF, and stability tests. A multivariate calibration model was then applied to accurately predict the sensor's response to other chemicals, such as isopropanol, heparin and adenosine.

4.2 Challenges with HC-PCF

Though PCFs were successfully used as a Raman signal enhancer, it is still not clear whether the results can be replicated and are stable enough under identical optical conditions to apply HC-PCFs for point-of-care technologies and environmental monitoring. As in Figure 3-12, Figure 4-1 displays different

concentrations of heparin samples, with an inset showing the linear relationship between the heparin sample at lower concentrations and the Raman signal. In addition, when PLS was applied to different concentrations of heparin samples, the R^2 at lower concentrations was 0.771 and the Raman spectra of heparin and PLS predictions were not well correlated, as shown in Table 4.1. This led to the development of a robust platform that can yield high quality, reliable spectral data suitable for PLS.

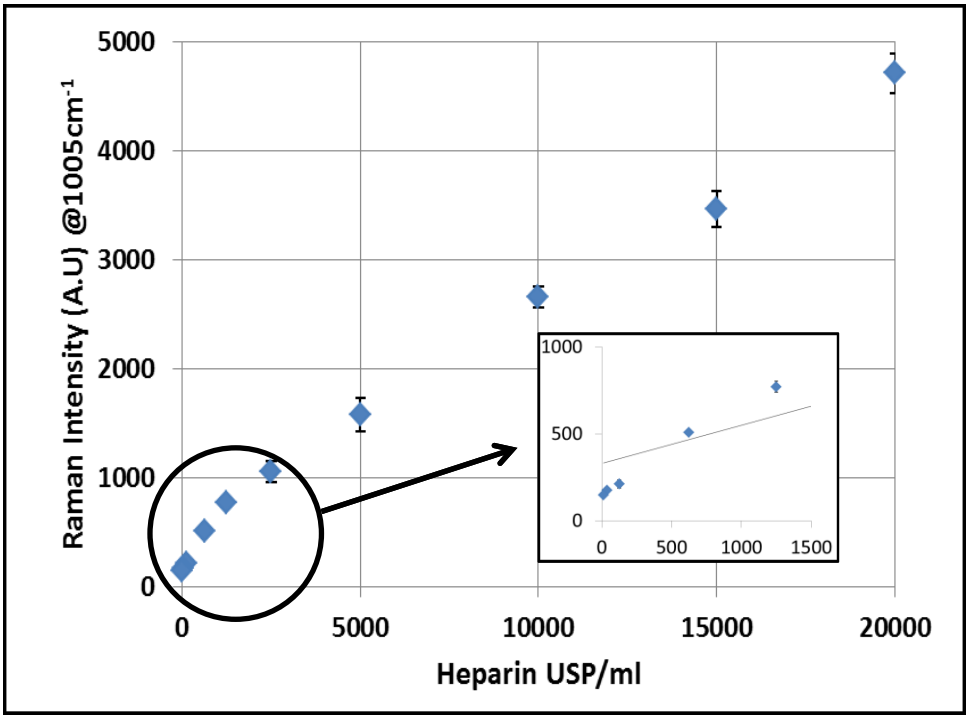

Figure 4-1 Raman peak intensity with heparin-serum concentrations with inset showing the lower concentration linear relationship

Heparin USP	PLS prediction USP
20000	**19316**
15000	**13141**
10000	**10523**

5000	**5246**
2500	**704**
1250	**1654**
625	**3566**
125	**563**

Table 4-1 PLS prediction of heparin concentration
without a differential pressure system

To address this issue, an integrated pressure-driven flow system that allows effective filling, draining and refilling of samples in an HC-PCF under identical optical conditions was developed. The device's detection capabilities were demonstrated by measuring various concentrations of aqueous ethanol and isopropanol, and different concentrations of heparin and adenosine in serum. The sensor's fluidic architecture includes two bypass channels on both ends of the HC-PCF, laid out in an 'H' configuration. The HC-PCF was connected to the bypass channels perpendicularly, and the sample flow was controlled by applying a pressure gradient. The HC-PCF and pressure-driven flow control system, enabled rapid injection and draining of sample solutions into the channels. This design configuration allows a high degree of control and reproducibility of the sample flow rate and direction, which facilitates multivariate analysis on the spectral data obtained from the sample in the HC-PCF for quantitative analysis.

The reservoir configuration is comprised of two parallel bypass flow channels: one for input/output of the interrogated samples and the other for input/output of the purging fluid (water). Tubing leading to each end of the bypass channel was immersed in the media (sample/purging liquid-water), which was contained in a glass vial. The other ends were connected to empty vials to collect the waste.

Each vial was pressurized at different pressures (P1, P2, P3, P4) to control the flow rates and direction, as shown in Figure 4-2.

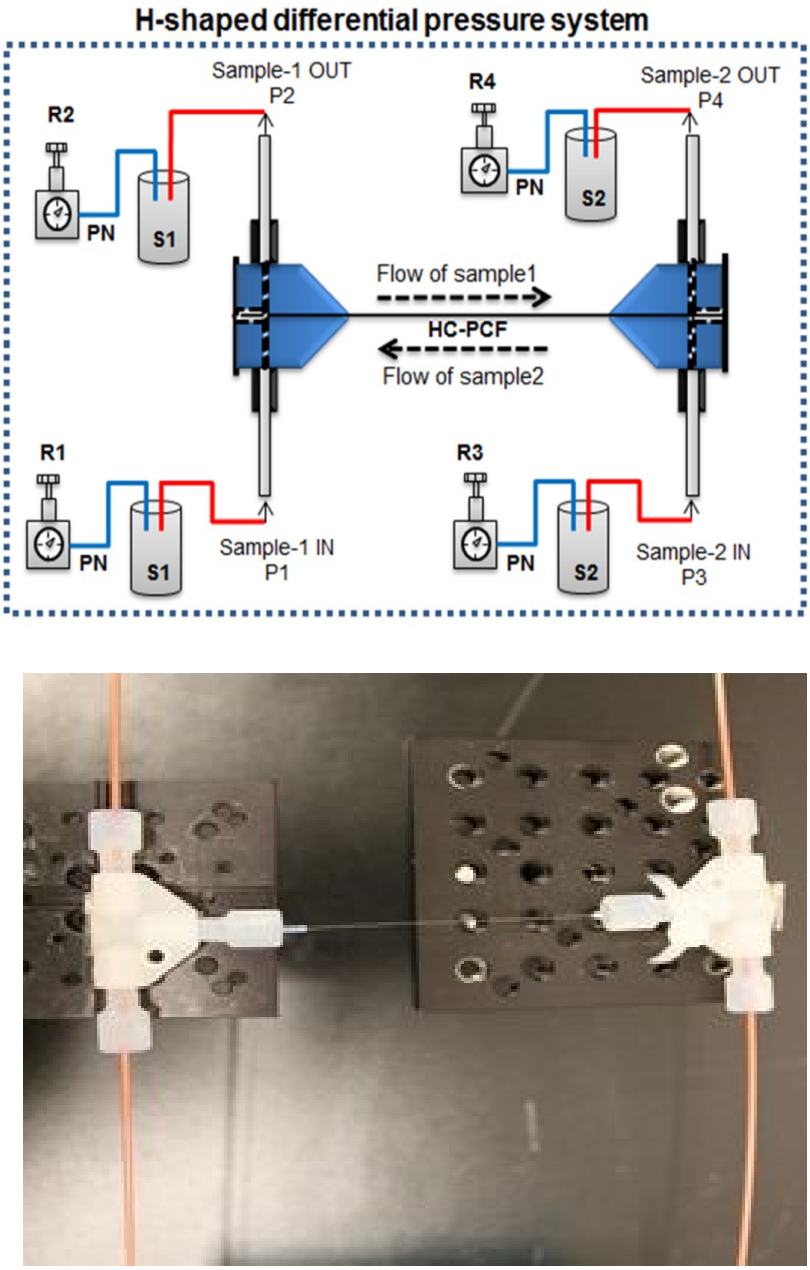

Figure 4-2 Integrated pressure driven reservoir for HC-PCF sensor platform

A 10 cm long HC-PCF was connected perpendicularly to each of the bypass channels, using a customized 4-way microfluidic cross mounted on a flexure stage (Thorlabs). The microfluidic cross was modified by removing one of its arms and

covering it with a glass cover slip to form an optical window for launching the laser light. The fiber tip was inserted into the center of each device, which exposed it to a strong perpendicular fluid flow. In preliminary testing, we found refilling was easier if the fiber entrance was at the center of this high-flow region, rather than near the chamber edge where the flow rate is less.

The perpendicular integration of the HC-PCF with two parallel fluidic channels formed an H-shaped structure, as shown in Figure 4-2. In order to introduce sample 1 (the sample mixture of interest) to the fiber channels, the average pressure of P1 and P2 was kept higher than that of P3 and P4, and for sample 2 (water) the pressures were reversed. The P1, P2, P3 and P4 values were varied to control the flow rate and direction of the samples into the HC-PCF. In each experiment, the HC-PCF sensor was filled with a fluid sample, and the corresponding Raman spectra was recorded at equilibrium. The HC-PCF was rinsed with deionized water before and after the introduction of a new sample.

4.3 Experimental details

4.3.1 Sample preparation

The ethanol and isopropanol for this research were purchased from Commercial Alcohol and Fisher Scientific Ltd. respectively, and concentrations of both in the range of 5% to 60% were independently prepared in deionized water. A 50 mM solution of HyClone Bovine Calf Serum from Thermo Scientific Ltd. and adenosine from Lancaster Synthesis was prepared, as well as five concentrations of adenosine in serum ranging from 5mM to 40mM, for recording Raman spectra using the HC-PCF sensor. MiniHep was purchased from Leo Pharmaceuticals in a vial of 25,000 United States Pharmacopeia (USP)/ml concentrations. USP indicates the potency of the drug in clinical applications. Seven concentrations of heparin in serum ranging from 25 USP/ml to 1,000 USP/ml were then prepared.

4.3.2 Experimental configuration

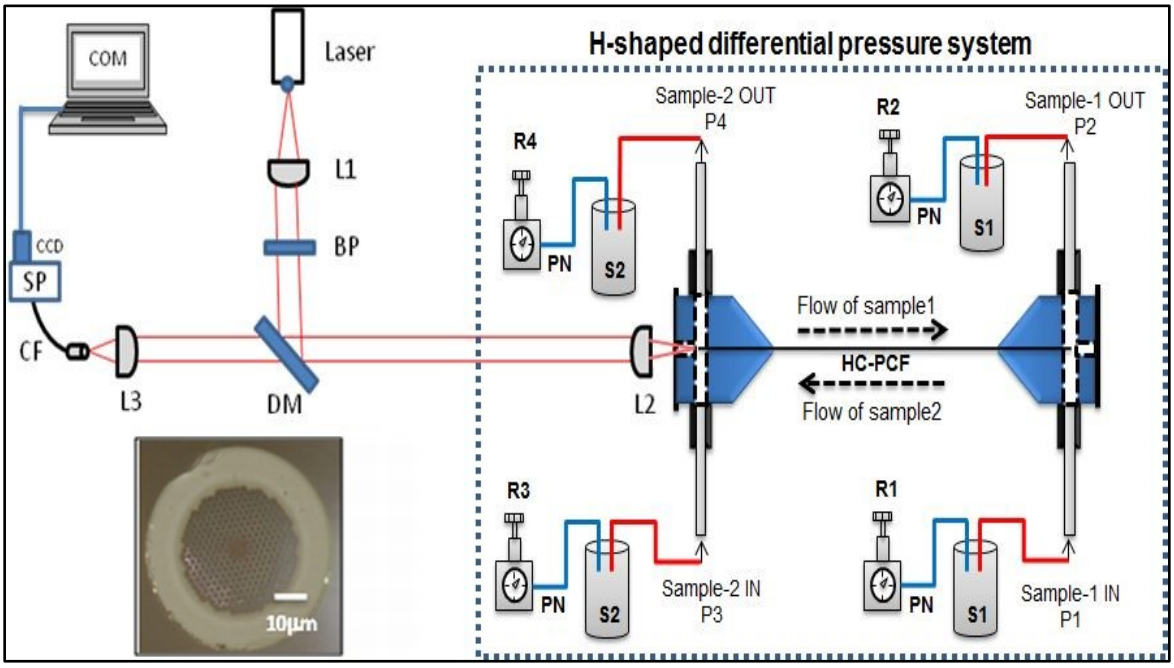

Figure 4-3 H- shaped differential pressure system experimental setup

Laser represents the Laser source; L1 the collimating lens; BP the band pass filter; DM the dichroic Mirror; L2 the microscope objective lens for light coupling; H-shaped differential pressure system with hollow core photonic crystal fiber (HC-PCF); S1 and S2 the samples in the vials; PN the pressurized nitrogen; R1-R4 the pressure regulators; L3 the microscope objective lens for backward light collection; CF the collection fiber; SP the spectrograph; CCD the CCD camera; and COM the computer.

The layout of the HC-PCF sensor consists of an optical Raman system and an H-shaped differential pressure system, as shown in Figure 4-3. The optical assembly employed a single mode 100 mW 14-pin butterfly pin laser (Photonic Solutions) with a central wavelength of 785 nm. The beam was first sent through a band pass filter (BP) centered at 785 nm (+/- 2 nm), then directed through a dichroic filter (R785RDC, Chroma Technologies Corp.) which reflected 785 nm (+/-5 nm) at an angle of 45º, and transmitted a 790 to 1,000 wide nm band. The dichroic filter acted as a reflector for the laser beam, which was further focused onto the tip of the HC-PCF by a 40X microscope objective lens (L1) with numerical aperture (NA)

of ~0.22. The dichroic filter also acted as a high pass filter for the back-scattered light from the sample-filled HC-PCF, allowing only the Raman wavelength to pass. The filtered Raman light was then imaged onto a 26 multimode NA=0.22 fiber bundle (Fiberoptic System Inc.) by a 6.3X microscope objective lens (L2) with an NA of ~0.22. The output of the fiber bundle was interfaced with a Kaiser f/18i Spectrograph with a TE-cooled Andor CCD camera, and Andor SOLIS software was used for spectral data acquisition. The other segment of the sensor is the H-shaped integrated pressure driven system with HC-PCF.

4.4 Results & Discussion

4.4.1 HC-PCF filling under different pressures

A fast sensor response time is necessary for practical applications, so we first investigated the effect of the pressure difference across the HC-PCF on the time required to fully load the sample into the HC-PCF. The sample filling time was determined by tracking the Raman signal as it reached maximum (equilibrium) from zero (baseline). Equation 4.1 allowed us to estimate the sample flow rate in the microchannels of the HC-PCF [114]. The viscosity of ethanol and water used to estimate the sample flow rate in 10 cm long HC-PCF was 1.09 and 1.00 centipoise (cP) respectively at 20^{o}C [115].

$$F = r^4 \frac{\pi \Delta P}{8 \mu l} \tag{4.1}$$

where r is the channel radius, l the channel length, ΔP the pressure difference across the HC-PCF and μ the sample's viscosity.

Figure 4-4 shows that the experimentally determined HC-PCF filling time is inversely proportional to the pressure difference across the fiber in the 15 to 60psi range; at 60psi, the sample filling time was reduced to approximately four minutes It should be noted that the maximum allowable pressure difference across the HC-PCF was limited by the pressure rating of the microfluidic cross fitting, which was approximately 60psi. Since there are multiple channels in the fiber (see Figure 4.3 inset), the flow rate is limited by the smallest channels in the fiber, which are those

in the cladding with diameters of 3.0 μm (+/- 0.1). Sample filling times (t) corresponding to various pressure differences (ΔP) were deduced from the calculated flow rates. The sample filling times experimentally determined are consistent with predictions, as shown in Figure 4-4.

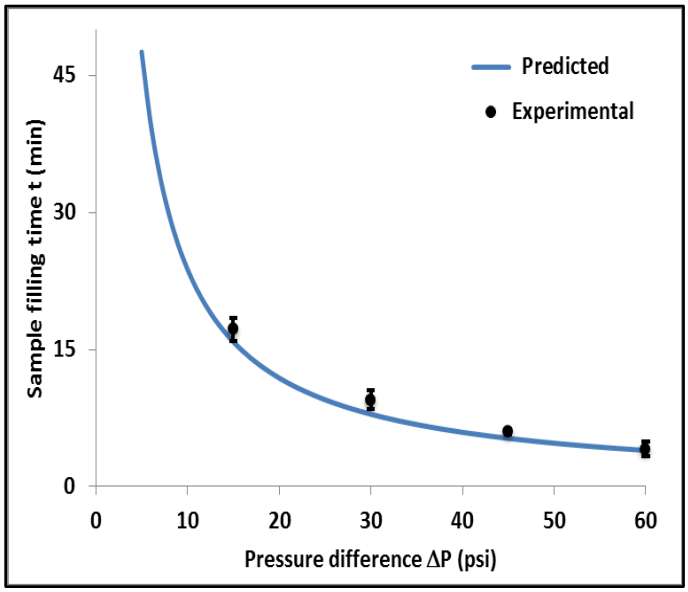

Figure 4-4 Experimental and predicted sample filling times (predicated obtained from Equation 4.1) for various pressure differences across the HC-PCF.

In Figure 4-4, the values used to estimate the filling times are a 1.5 μm microchannel radius, a 10 cm long fiber and a viscosity of ethanol and water of 1.09 and 1.00 centipoise (cP) respectively at 20^{o}C [115]).

4.4.2 Sample filling and Raman data

During this experiment, P1, P2, P3 and P4 were maintained at 62, 60, 2 and 0 psi, respectively. Before introducing samples in HC-PCF, precautions were taken to degas the samples to avoid any bubbles entering inside HC-PCF, cleaning the reservoir and the sample vials with acetone to remove any dust etc. The Raman spectrum of the sample was recorded in time intervals of one minute, with an integration time of 0.5 s when ethanol was introduced to the HC-PCF.

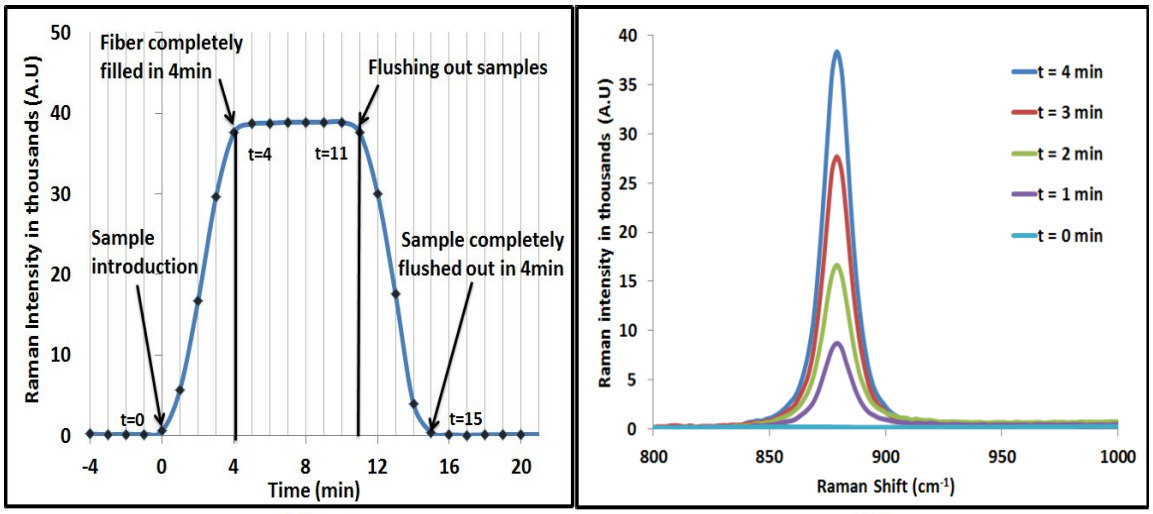

Figure 4-5 Sample filling time in HC-PCF

(a) Filling HC-PCF with ethanol and flushing out the ethanol (cycle) with time, and (b) increase in the Raman signal of the ethanol solution as it filled the microchannels of the HC-PCF

The Raman peak at ~880 cm^{-1} (C-O-C stretching) was monitored to track the sample filling time of the HC-PCF. Figure 4-5 (a) shows a complete fill/flush cycle. The experiment began by recording the Raman spectra of the HC-PCF filled with water, to obtain a baseline. At t = 0 min. the ethanol sample was introduced into the HC-PCF by reversing the pressure, which resulted in a gradual increase of the Raman peak intensity for ethanol as the sample mixtures entered the HC-PCF. At t = 4 min. the signal equilibrated, indicating the fiber was completely full. At t = 11 min. the pressure difference across the HC-PCF was reversed to rinse out the fiber channels with water. With the introduction of the water the Raman peak for ethanol gradual decreased, which confirmed that the water was displacing the ethanol from the other and pushing the sample mixture out of the HC-PCF. The time required to completely purge the sample solution from the HC-PCF was 4 min. as indicated by the complete attenuation of the Raman peak of ethanol around 880 cm^{-1} at t = 15 min. Figure 4-5 (b) shows the Raman peak of ethanol increased with time as it seeped into the HC-PCF microchannels.

4.4.3 Repeatability and stability tests

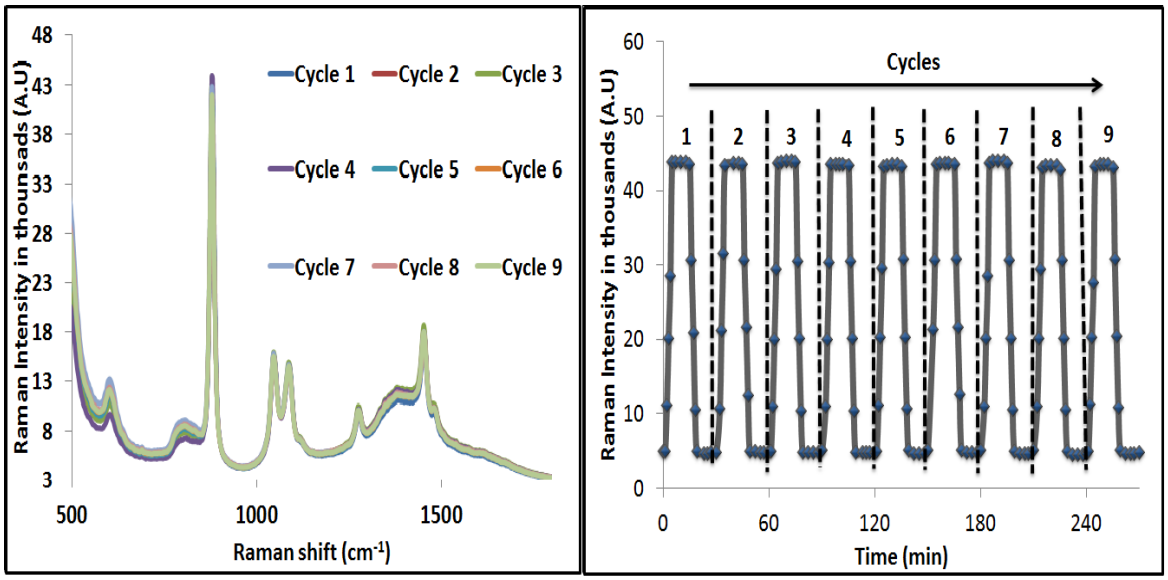

Figure 4-6 Repeatability and stability test

(a) Raman signal of HC-PCF filled with 50% ethanol concentration, and (b) cycle of filling and flushing out sample

The experimental procedure involved repeatedly filling the HC-PCF with fresh sample solution, then purging the system with water. The sample solution was completely flushed out by the water prior to the injection of another sample. To assess reproducibility, nine cycles were measured under identical conditions. The Raman signal was monitored in each cycle, and it was found to be almost identical, as shown in Figure 4-6 (a). The Raman signal-to-noise ratio for the band at 880cm^{-1} averaged approximately 40,000, with a deviation of 3%. Figure 4-6 (b) illustrates the reproducibility, as multiple cycles of filling using the same sample were performed using the fluidic control system. The results suggest that the filling and flushing times are consistent from one experiment to another. This reproducibility demonstrates that integrating the HC-PCF with a differential pressure system allows the sensor to be reused by introducing different samples sequentially.

4.4.4 HC-PCF for different concentration and PLS

The next phase of the investigation focused on applying partial least square (PLS) analysis, an important multivariate chemometric method, on the Raman spectrum of various samples that were injected into the HC-PCF.

Though PLS has been widely used with Raman spectroscopy for trace level detection of bulk samples (cuvette) [116], its application on the Raman spectral data collected from a sample loaded HC-PCF has not been reported to date. Different HC-PCFs are typically employed for different sample sets. However, replicating the exact light coupling condition for every HC-PCF is difficult, as different modes are excited depending on the alignment of HC-PCF tip with respect to the focusing optics. Moreover, the common technique of filling the HC-PCF with the sample by capillary action might not ensure complete filling of the core and cladding channels, or cause the sample distribution to vary from one HC-PCF to another. As a result, light guidance within the HC-PCF is severely affected while the spectral background fluctuates from one spectrum to another. In these cases, any kind of multivariate analysis tool, including PLS, will fail to establish a proper correlation of Raman signal to the species concentration, which ultimately leads to an inability to predict the sample constituents.

Different sample solutions of ethanol-water mixture (mass %) were injected into a single HC-PCF, and their respective Raman spectrum was recorded without altering the light coupling conditions. Between consecutive injections of any two sample solutions, the HC-PCF was rinsed with water to completely remove all traces of the preceding sample solution, thereby ensuring high quality Raman spectra. The high quality spectral data set exhibited little spectral background fluctuation, and was suitable for direct multivariate analysis without requiring spectral pre-processing.

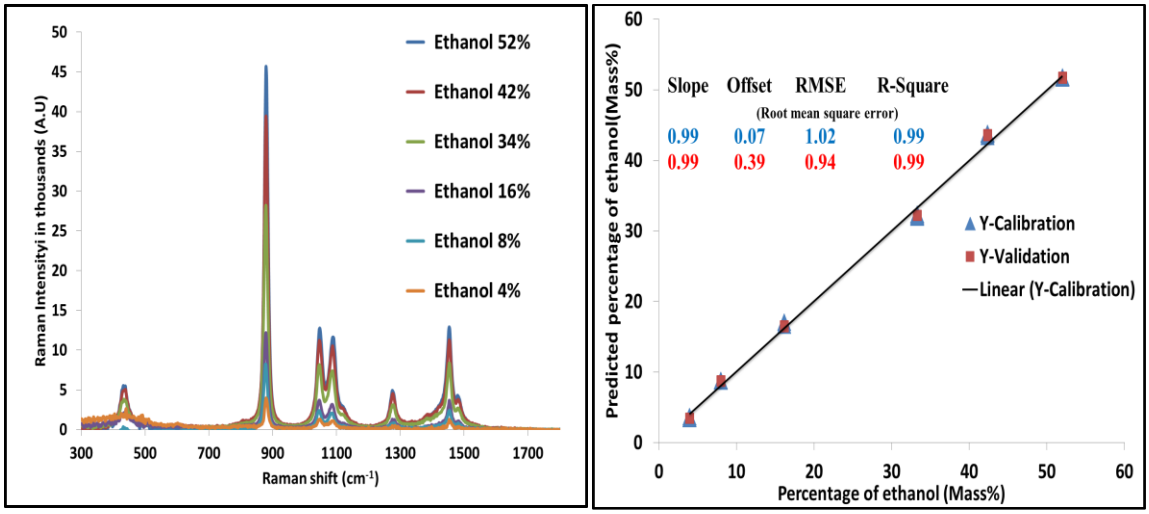

(a) (b)

Figure 4-7 HC-PCF for monitoring ethanol-water mixture

(a) Raman spectra of different concentrations of ethanol in a HC-PCF (mixture are represented in mass %) (b) PLS prediction (linear fit y=0.997x + 0.0598)

Figure 4-7 (a) shows the Raman spectrum of different sample solutions when the ethanol concentration varies with respect to water. PLS was applied to the spectral data to obtain a calibration curve, as shown in Figure 4-7 (b). The calibration model predicts the concentration of ethanol in the range of 4 to 52% (mass %), with a low root mean square of ~0.9%. The coefficient of determination (R_2) was ~0.997, which indicated that the Raman spectral data of different ethanol-water samples correlated well with the concentration of ethanol.

To further demonstrate the sensor's capabilities, we filled the HC-PCF with various concentrations of isopropanol in water and recorded the respective Raman spectra as shown in Figure 4-8 (a), then applied multivariate analysis to predict the concentration of isopropanol. We found that the calibration model predicted the isopropanol concentration accurately, with a low root mean square of ~0.1% and R2 of ~0.997, as shown in Figure 4-8 (b).

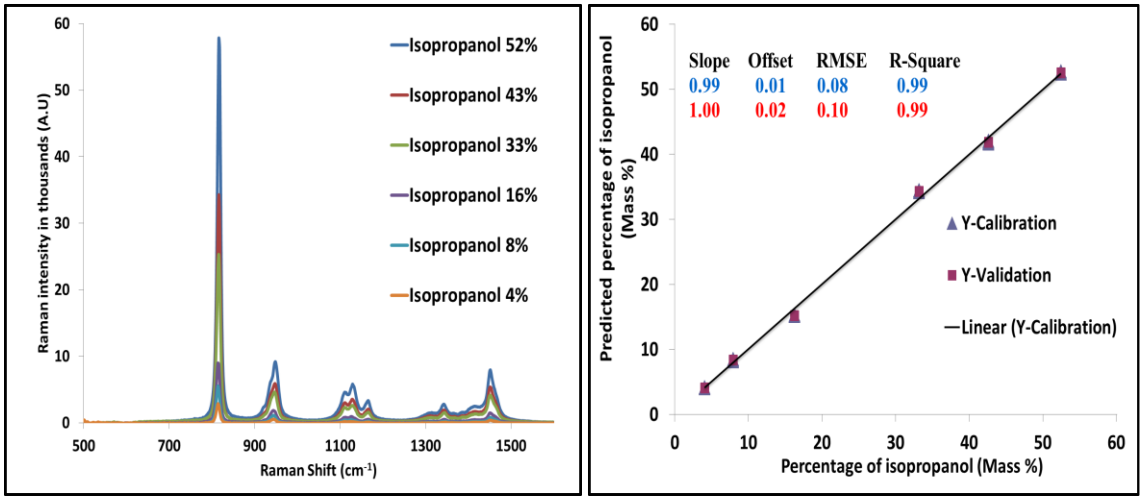

(a) (b)

Figure 4-8 HC-PCF for monitoring isopropanol-water mixture

(a) Raman spectra of different concentration of isopropanol filled in a HC-PCF (mixture are represented in mass %) (b) PLS prediction (linear fit y = 0.998x + 0.0495)

4.4.5 HC-PCF for monitoring clinically important molecules

In the final stage of the investigation we injected different clinically important samples, such as heparin and adenosine, into the HC-PCF with the pressure-driven flow system. Heparin is a vital blood anticoagulant that is commonly incorporated with a patient's blood during heart surgeries. In order to apply multivariate analysis to the spectral data, we prepared seven different concentrations of heparin in serum ranging from 25USP/ml to 1000USP/ml; then recorded the Raman spectra for each mixture.

Figure 4-9 (a) shows the Raman spectra for heparin in serum (without background subtracted as compared to Figure 3-12 (a)) at different concentrations, in the spectral range of 950 to 1100 cm^{-1}. Since the Raman spectra clearly overlapped and had low intensity Raman peaks of heparin, there was no explicit correlation between the Raman spectrum and the concentrations. Correlating the Raman bands of heparin with the concentrations was very difficult using a simple calibration model, so PLS was applied to the spectral data to determine the

concentrations. Figure 4-9 (b) shows the calibration curve with multivariate analysis. Compared to the results of the previous setup with no pressure differential system attached to the HC-PCF (this data is not shown here), the coefficient of determination (R^2) improved from 0.771 to 0.993, and the root mean square error (RMSE) decreased from 832 to 25 USP/ml. Based on the PLS analysis, the limit of detection (LOD) (defined as 3*RMSE) was calculated as 75 USP/ml. Although the LOD of HC-PCF sensor is slightly higher than the clinical level for heparin monitoring (0 - 20 USP/ml), the robust HC-PCF platform with further enhancement (increasing length of HC-PCF, integrating with nanoparticles) has the potential of attaining lower LOD.

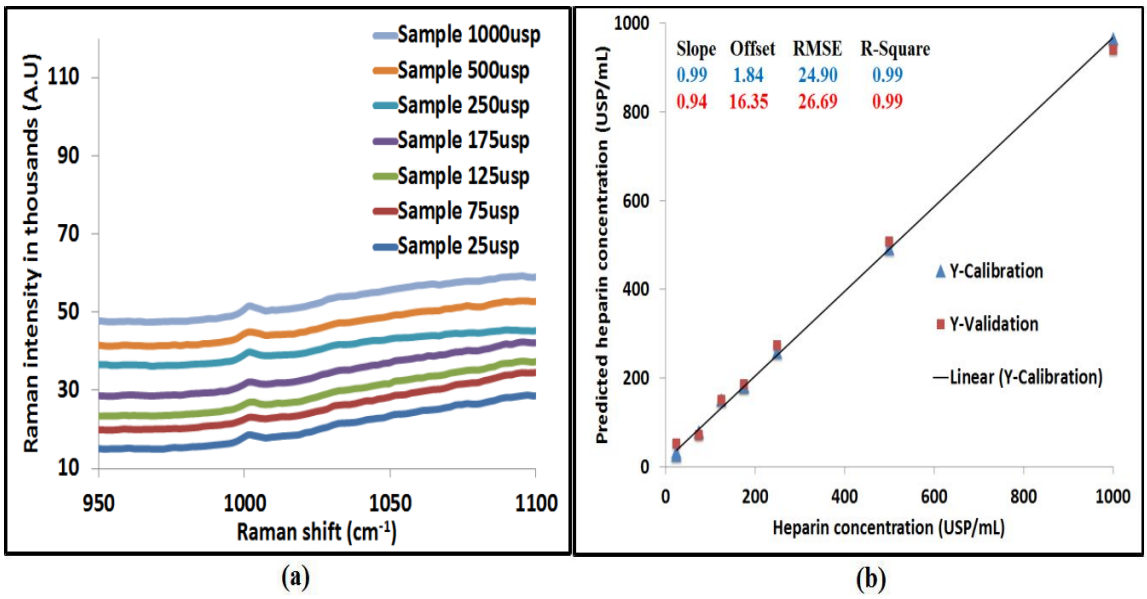

Figure 4-9 HC-PCF for monitoring heparin-serum mixtures

(a) Raman spectra of different concentrations of heparin in serum in an HC-PCF

(b) PLS prediction (linear fit y = 0.995x + 13.5)

The second clinically relevant molecule tested was adenosine, which is important in clinical environments as it regulates extra-cellular physiological activity. Monitoring adenosine is vital, due to its impact on pro-inflammatory and tissue destruction during bronchoconstriction in patients with asthma and chronic obstructive pulmonary disease (COPD) [117]. Sample solutions of adenosine in serum in the range of 5 to 40mM were prepared, and the Raman spectra were

recorded at different concentrations, as shown in Figure 4-10(a). Adenosine exhibited a weak Raman peak at 724 cm^{-1} due to the ring breathing of C_5N_7, as reported by Chen *et al.*[118]. A medium intensity Raman peak around 1000 cm^{-1} corresponding to serum (Phenylalanine, C-C stretching) decreased as the adenosine concentration increased, with respect to serum concentration. As with monitoring heparin in serum, no direct correlation existed between the Raman peak of adenosine and its concentration. Therefore, we applied PLS to determine the concentration of adenosine in serum. Figure 4-10 (b) shows the PLS calibration curve with an R^2 of ~0.995 and RMSE of ~1 mM (LOD ~3 mM). These results indicate that the HC-PCF interfaced with a pressure-driven flow system can be used as a biosensor to monitor clinically important molecules accurately and consistently.

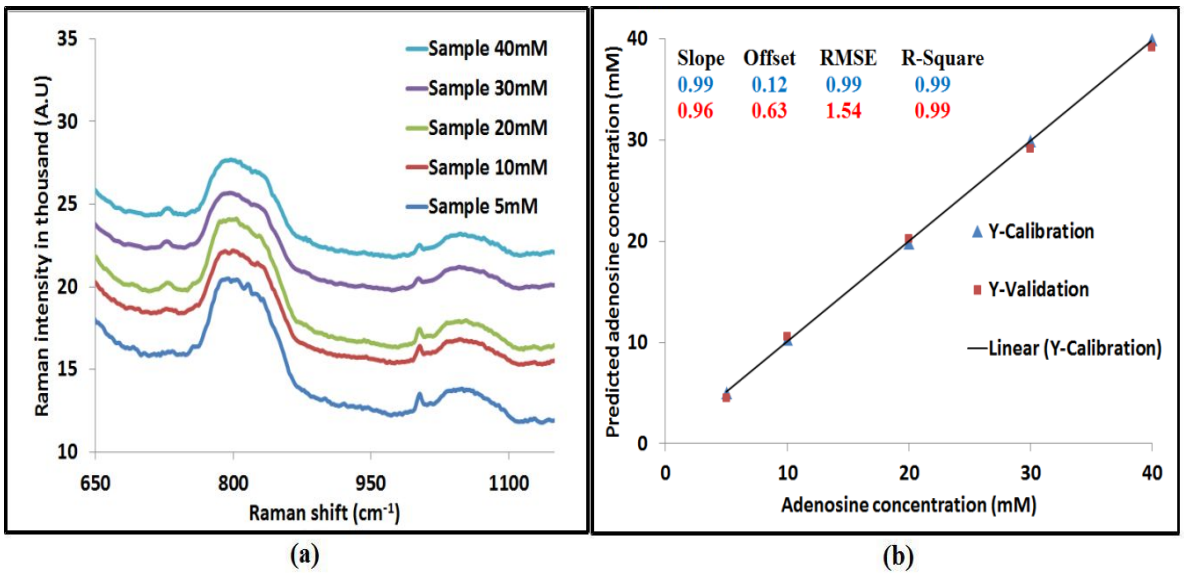

Figure 4-10 HC-PCF for monitoring adenosine-serum mixtures

(a) Raman spectra of different concentration of adenosine in serum in an HC-PCF

(b) PLS prediction (linear fit y = 0.994x + 0.118)

4.5 Conclusion

This work shows that integrating pressure-driven flow with an HC-PCF improves the stability, speed of filling and reusability of HC-PCFs, which could lead to an HC-PCF based Raman sensing platform for real-time monitoring and diagnostic

applications. A pressure difference of 60 psi across the HC-PCF enabled filling a 10cm HC-PCF with a sample within four minutes. The experimentally measured filling/draining times for samples into the HC-PCF corresponded closely to the expected values. The filling time could be further reduced by increasing the pressure difference, or decreasing the length of the fiber. The spectral reproducibility for various cycles of sample injection into an HC-PCF was also verified. Our experimental configuration allowed consistent filling of samples into an HC-PCF for all sets of sample mixtures, and for the first time stable operation of an HC-PCF based Raman sensor gave high quality spectral data. Achieving stability and reproducibility of the Raman spectra with an integrated HC-PCF pressure driven system demonstrated the capability of partial least square (PLS) analysis on the spectral data to accurately predict the concentrations of ethanol, isopropanol, heparin and adenosine in a sample mixture. This method has great potential for high sensitivity, rapid and real-time monitoring of various concentrations of chemicals that are of clinical and environmental importance.

Publications from this work:

P2.**A. Khetani**, A. Momenpour, J. Riordon, V. S. Tiwari, M. Godin and H. Anis: "Hollow core photonic crystal fiber as a re-usable Raman biosensor." Optics Express 21, 12340-12350 (2013).

Novelty: This paper demonstrates the integration of a fluidic control system that ensures the repeatability and reusability of an HC-PCF sensor. It provides a brief description of HC-PCF, and proposes an H-shaped differential pressure system layout common to microelectromechanical system (MEMS) microfluidic flow control. Ethanol was used to benchmark the performance of the device. Subsequent sections summarize the findings related to optimal pressure difference, sample filling time into the HC-PCF, and stability. An important achievement of this paper is applying a multivariate calibration model to accurately predict the response of the

sensor to other chemicals, including ethanol, isopropanol, heparin and adenosine. This was done using HC-PCF for the first time here.

P3. **A. Khetani**, A. Momenpour, J. Riordon, V. S. Tiwari, M. Godin and H. Anis: "Hollow core photonic crystal fiber as a robust Raman biosensor." SPIE Photonics West 8576-14 (2013).

Novelty: This paper reports our initial findings on the integration of HC-PCFs, microfluidics, and statistical analysis to monitor biomolecules using Raman spectroscopy. Using HC-PCF for practical applications could be challenging, due to limitations inherent in the coupling, stability, evaporation, clogging, consistent filling and reusing of the same fiber. These shortcomings reduce the potential of HC-PCF to detect low concentrations in liquid samples, which is why the method is not yet applied in the lab. The device is based on an H-design layout that uses the pressure difference between the two ends of the fiber for filling and flushing the samples. It addresses several issues related to device performance by enabling filling of the fiber with liquid samples consistently, rapidly and reproducibly.

Chapter 5. Surface enhanced Raman spectroscopy (SERS) in HC-PCF

5.1 Introduction

This chapter investigates the effect of the volume and size of silver nanoparticles (AgNP) on the surface enhanced Raman scattering (SERS) signal of rhodamine 6G (R6G) in a hollow core photonic crystal fiber (HC-PCF). The HC-PCF enhanced the Raman signal of R6G by a factor of ~90. In addition, the optimal size and volume of AgNP enhanced the Raman signal of R6G by a factor of ~40, resulting in a total enhancement of ~4,000 in the HC-PCF. A comparison of AgNP enhancement factors in HC-PCF and bulk (cuvette) samples at their optimal size and volume with respect to R6G, is presented. The SERS based HC-PCF sensing platform, optimized for R6G as a test molecule, was further applied to monitoring adenosine for clinical applications; the platform has also been used to detect leukemia cells. With the present scheme, we were able to detect up to 300 cells/ml of leukemia cells compared to flow cytometry, thus providing a novel alternative to existing clinical standards. Furthermore, we could accurately distinguish live, apoptotic and necrotic leukemic cells.

The chapter begins by describing the role of HC-PCF and nanoparticles for enhancing the Raman signal, and Section 5.2.1, focuses on nanoparticle characterizations. The following sections present the spectral data and calibration curves, and show the dependence of various enhancement factors on particle size. The optimum volume and size of the nanoparticles was further used to demonstrate the application of SERS based HC-PCF sensing platform in monitoring adenosine, as well as for the detection of leukemia cells.

5.2 Optimizing the size and volume of nanoparticles in HC-PCF

As discussed in Section 2.5, various groups have used a combination of HC-PCF and SERS to enhance the weak Raman signal in HC-PCF, but only limited work has been done to explore the contribution of HC-PCF and nanoparticles to overall enhancement of the Raman signal. Thus, there is a shortage of information on the role played by spatially confined NP in micro-structured media such as HC-PCF interacting with optically confined light. Moreover, the determination of optimal sizes and volumes of NP for achieving maximum SERS signals in an HC-PCF has not been investigated previously. For this reason, we focused on experimentally determining the optimal size and volume of spherical-shaped silver nanoparticles (AgNP) to achieve the maximum sensing potential of a SERS based HC-PCF platform. This study evaluates the contribution of HC-PCF and nanoparticles in the overall enhancement of the Raman signal of rhodamine 6G (R6G) as a test molecule. It builds on our previous work that established the role of HC-PCF's as Raman signal enhancers, due to their photonic band gap property [119,120].

A modal field analysis was required to confirm the single mode nature of an HC-PCF fiber filled with R6G and nanoparticles. The mode field pattern of the light emanating from the other end of an HC-PCF filled with R6G and AgNP was imaged using a CCD camera (Canon), and the pattern exhibited a Gaussian profile. The far-field pattern of light emitting from an HC-PCF filled with a solution of R6G and 60 nm AgNP is shown in Figure 5-1, and the modal field diameter depicted in the Figure 5.1 was found to be ~3.10 mm, which was quite close to the theoretically calculated value of 3 mm. We found similar mode field patterns for other sets of solutions, where R6G and AgNP volume ratios were maintained and only difference was the AgNP diameters. Thus, it was confirmed that propagation properties did not change appreciably with respect to nanoparticle size.

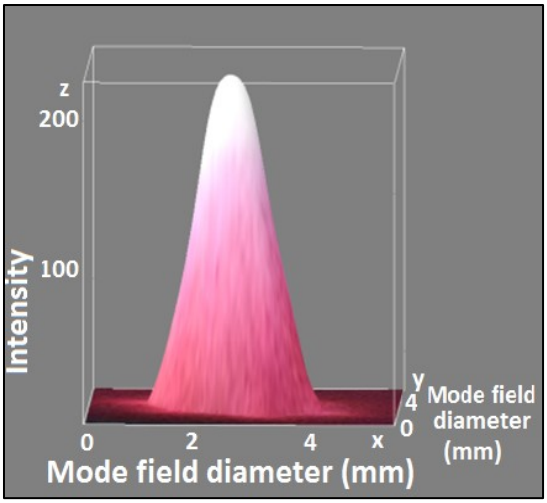

Figure 5-1 Spatial distribution of fiber modal field of sample solution filled HC-PCF imaged using a CCD camera (Canon)

5.2.1 Nanoparticle characterization

The spherical silver nanoparticles (AgNP) were purchased from NanoComposix Inc. The silver concentration was 0.02 mg/ml. The UV-Vis spectra were obtained using a CARY 50 UV-Vis spectrometer from Varian Inc. [121], and the spectra were recorded over a wavelength range of 300 to 700 nm, as shown in Figure 5-2 (a). It is clear that peak absorbance of AgNP is red-shifted with the increase in particles size. The sizes of nanoparticle were measured in the lab (shown in inset). The TEM images of different sizes of AgNP from NanoComposix are shown in Figure 5-2 (b).

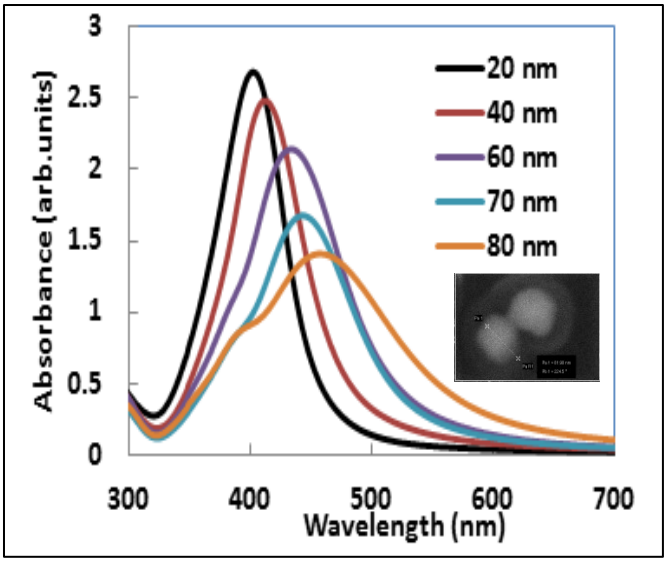

(a)

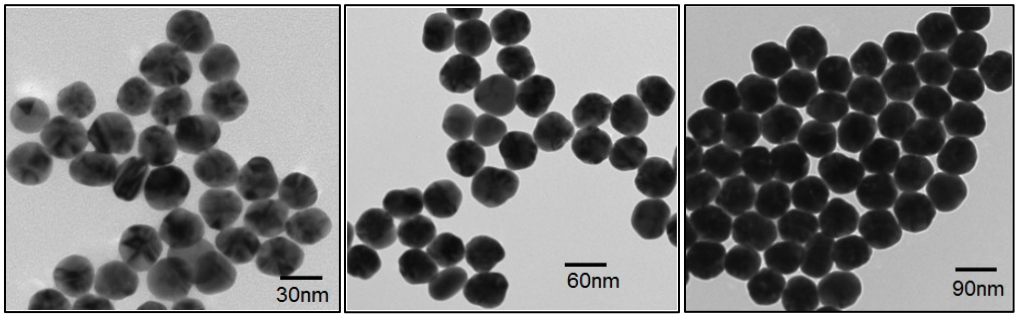

(b) (c) (d)

Figure 5-2 Nanoparticle characterization

(a) UV-vis absorption spectra of different sized Ag-NP (inset showing SEM of AgNP 80nm) (b)TEM images of different sized AgNP spheres of 30 nm (c) 60 nm (d) 90 nm (Courtesy: Nano Composix Inc.)

5.2.2 Results and discussions

5.2.2.1 Raman signal enhancement in HC-PCF

This research initially focused on recording the Raman spectrum of a pure rhodamine 6G (R6G) solution injected into the HC-PCF. The concentration of R6G was 10^{-3} M, and remained so throughout the study. The same R6G solution was also recorded in cuvette (bulk sample) under similar experimental conditions. The experimental setup was same as shown in Figure 4-2 and discussed in Chapter 4. The acquisition time for recording a spectrum was 2 s, and five spectra were

recorded for each measurement. The Raman peak intensities were measured for normal Raman and SERS spectra of R6G at a wave number of approximately 1,365 cm^{-1}, and their ratios were calculated to determine enhancement factors. Following similar calculations, the enhancement factors were calculated for various sample sets corresponding to R6G, and different sizes of nanoparticles. The experiments were repeated on different days, and the results were quite consistent.

The samples were prepared as follows: To determine an optimal ratio of nanoparticles and sample (R6G), different volumes of nanoparticles (0.02 mg/ml) were added to a fixed amount of 10^{-3} M R6G (1 ml) to prepare sets of sample solutions. The size of the nanoparticles was constant, while the total volume of the sample was different for each set of solutions. The sample sets were then injected into HC-PCF and cuvette, and the SERS spectrum of the sample solution in each was recorded. Similarly, to determine the optimal size of nanoparticles in HC-PCF for a maximum SERS signal, various sets of sample solutions of nanoparticles and samples (R6G) were prepared. In this case, the volume of both the R6G and nanoparticles was kept constant, while the size of the nanoparticles in each sample set varied. Also, the volume ratio of AgNP and R6G was kept as 1:2 for all the sample sets. The total sample volume was 1ml which was same for various sample sets of nanoparticles and R6G. Figure 5-3 shows that the Raman signal of R6G obtained from HC-PCF is enhanced, compared to that in the cuvette.

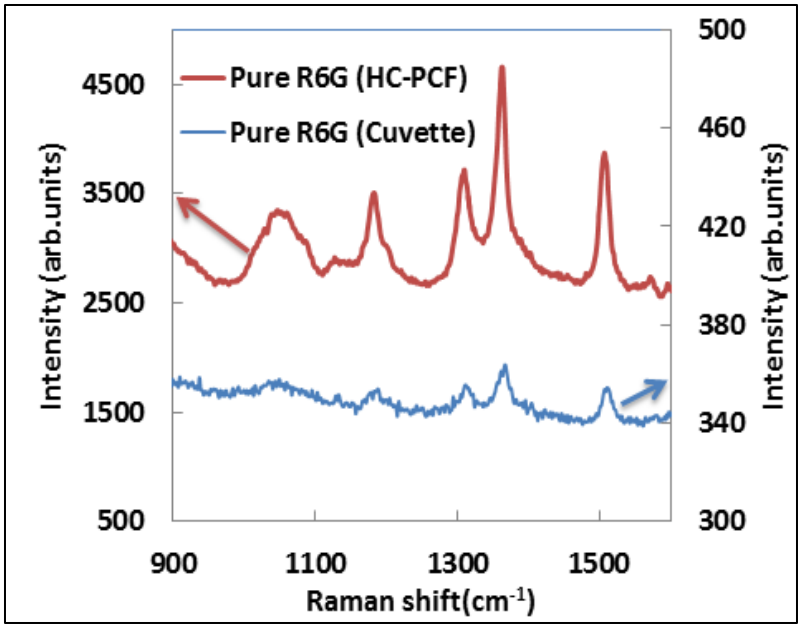

Figure 5-3 Raman spectrum of pure R6G in HC-PCF and cuvette

The HC-PCFs are known to enhance the Raman signal, as it supports strong modal field overlap with the sample due to its photonic band gap property (as discussed in section 2.4.1). The aim of this experiment was to determine the factor by which HC-PCF alone enhances the Raman signal, which we found as ~90. The signal enhancement factor of HC-PCF was calculated by dividing the Raman signal of R6G from HC-PCF by the Raman signal of R6G from cuvette. For the sake of comparison, the sample power of the cuvette was the same as the output power from the sample filled HC-PCF. Figure 5-3 shows the prominent Raman bands of R6G in the spectral range of 900 to 1,600 cm^{-1} (the details with respect to different vibrational modes are discussed elsewhere) [122]. To evaluate the various enhancement factors that correspond to nanoparticles and HC-PCF, we considered the SERS peak at 1,365 cm^{-1} (arom. C-C stretching). The enhancement factor calculated here only takes the ratio of the enhanced Raman peak intensity and the normal Raman peak intensity into account. It does not consider the ratio of the number of molecules sampled in bulk and those which are adsorbed on the NP surface (G factor), which is usually presented when evaluating Raman enhancement factor. Enhancement factors that only consider the ratio of the SERS signal and the normal Raman signal, without taking the exact

number of molecules sampled in the solution into account, is commonly defined as the analytical enhancement factor.

5.2.2.2 Optimal volume ratio of AgNP and R6G for maximum SERS signal enhancement

An optimal volume ratio of AgNP and R6G to achieve maximum enhancement of Raman signal in HC-PCF was then determined. We defined the enhancement factor of AgNP in HC-PCF (EF HC-PCF) as the ratio of the SERS peak intensity of R6G in HC-PCF and the normal Raman peak intensity. For comparison, the enhancement factor of AgNP in cuvette (EF CUV) was defined as the ratio of the SERS peak intensity of R6G in cuvette and the normal Raman peak intensity. The sample power in cuvette was the same as that of the sample solution (R6G and AgNP) filled HC-PCF (~2mW) during all the phases of the experiment. The Raman peak intensities were calculated at 1,365 cm^{-1}. Six different sample solutions of AgNP and R6G were prepared at volume ratios (AgNP/R6G) of 1:10, 1:3, 1:2, 2:1, 4:1 and 8:1 respectively. The 1ml volume of the 10^{-3} M R6G solution was constant throughout the study. We only varied the volume of nanoparticles with respect to a fixed volume of R6G to determine an optimum volume ratio of nanoparticles and R6G which would give maximum enhancement of Raman signal in HC-PCF. Samples were filled into HC-PCF followed by filling into cuvette, then the SERS spectra of the sample solutions were recorded and enhancement factors of AgNP calculated for each. Figure 5-4 shows that EF HC-PCF increases with higher volume ratios of AgNP and R6G. It reaches a maximum (~40) when the volume of AgNP is half of that of R6G, then tends to decline. The cuvette EF also increases with higher volume ratios of AgNP and R6G. It reaches maximum when the volume of AgNP is twice that of R6G, then almost saturates with increases in the volume of AgNP because SERS reaches a maximum intensity at complete monolayer coverage of the NP surface by R6G. The further increase of AgNP creates multilayers of adsorbate (R6G) on the surface, consequently saturating the SERS intensity.

Figure 5-4 clearly shows that the optimal volume ratio of AgNP and R6G for maximum signal enhancement in HC-PCF is different than that for cuvette. Figure 5-4 also indicates that the maximum enhancement factor of AgNP in HC-PCF was less than that of cuvette by a factor of ~2. This is largely because AgNP tends to scatter more light in the microliter volume of HC-PCF when the amount increases beyond a certain threshold with respect to R6G, which means that the absolute enhancement capability of nanoparticles is somewhat compromised in HC-PCF compared to cuvette. However, subsequent sections will show that the enhancement factor of a Raman signal due to the cumulative enhancement effects of AgNP and HC-PCF, is greater than the maximum enhancement factor of AgNP in cuvette.

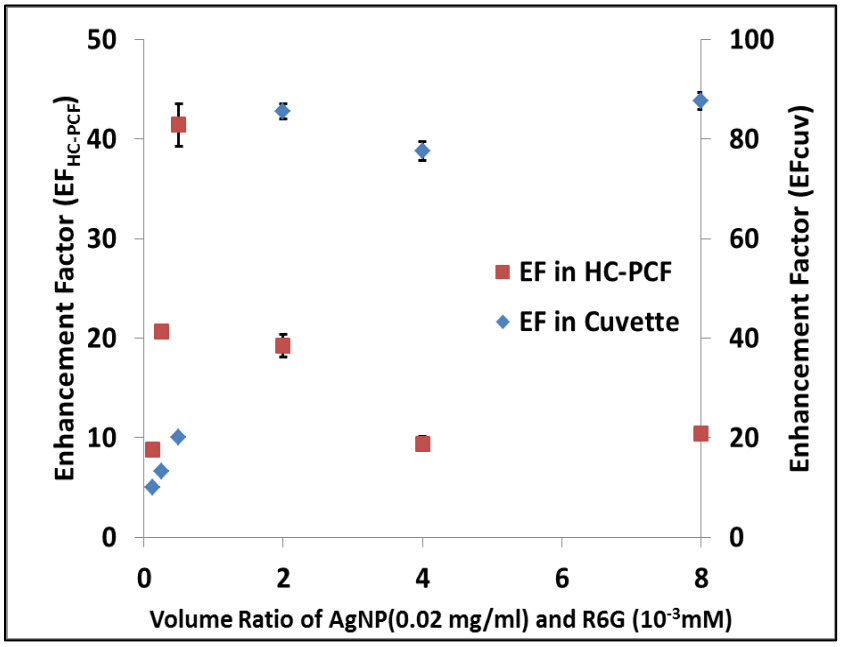

Figure 5-4 Enhancement factor (EF) vs relative volume of AgNP/R6G in cuvette and HC-PCF

5.2.2.3 Optimal size of AgNP for maximum SERS signal enhancement

The next step was to determine the optimal size of AgNP to achieve a maximum SERS signal of R6G in HC-PCF. The volume ratio of AgNP and R6G was 1:2 as established in the previous section, and was kept constant for all measurements

with different sizes of AgNP. Thus, seven sample sets were prepared with identical volume ratios of np and R6G, while the AgNP diameter was set at 20 nm, 30 nm, 40 nm, 50 nm, 60 nm, 70 nm and 80 nm.

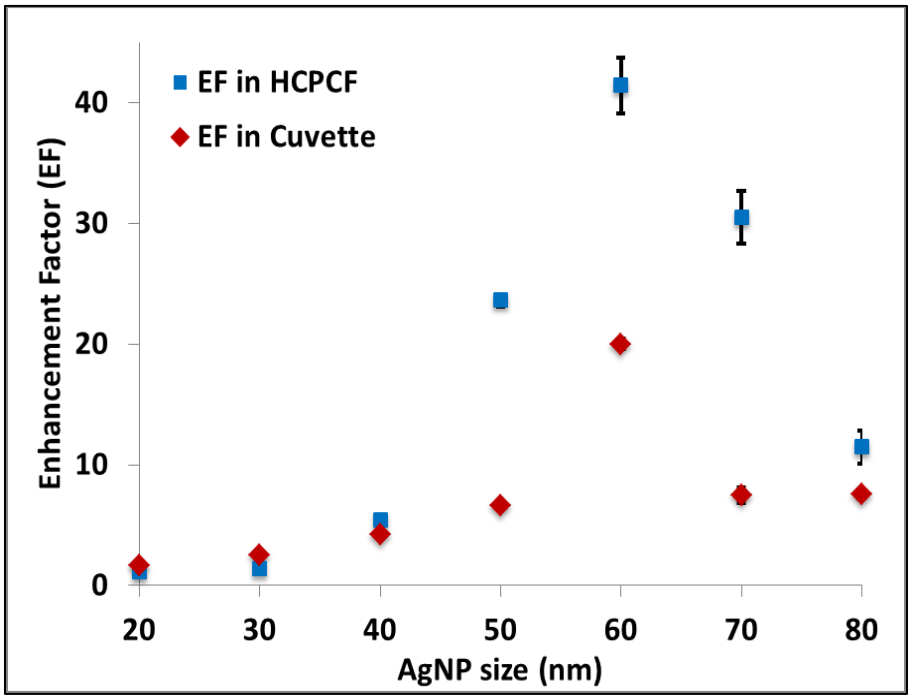

Figure 5-5 Enhancement factor vs AgNP size in HC-PCF and cuvette

Figure 5-5 shows that the EF HC-PCF values gradually increased with the increase of the AgNP size, and was maximum at the diameter of ~60 nm. With increases of the AgNP size beyond 60 nm, the EF HC-PCF decreased. A similar trend was observed when the same sets of samples were observed in a cuvette. The optimal size of AgNP for a maximum SERS signal for bulk samples (cuvette) was found to be 60 nm, which is consistent with our previous report [121]. The field enhancement in the vicinity of the nanoparticle surface is dependent on various parameters, including the dielectric constant and size (radius) of the NP, etc. However, it tends to fall after reaching a certain particle size, as observed here. This phenomenon is due to the 'particle plasmon model' of SERS, which is as follows: In the case of large particles, damping of the dipolar electric field occurs at the NP surface due to radiative losses, which results in a broadening of the plasmon resonance and a decrease in the magnitude of field enhancement for

larger particles. For smaller particles, the material damping term in the dipolar field is negligible and can be disregarded. Consequently, the dipolar field, which is related to the induced polarization, increases with particle size until the damping term reaches a significant value. Thus, an initial increase in the magnitude of enhancement owing to NP size is due to dynamic depolarization, which is limited by the radiative damping of higher sizes of NP. In addition, enhancement produced by smaller particles (whose size can become smaller than the electron mean free path) is limited by the surface scattering effect. All these factors determine the optimal size of nanoparticles to achieve a maximum SERS signal [123-124].

Based on these results, it is concluded that 60 nm is the optimal size of AgNP for the maximum SERS signal in both HC-PCF and as cuvette. Furthermore, the similarity in the trend of EF HC-PCF and EF CUV curve against AgNP size suggests that the competition between radiation damping with respect to surface scattering and dynamic depolarization, which determines an optimal np size for SERS, exist in both micro-liter volumes of HC-PCF and in cuvette (bulk sample). Thus, the optimal size for maximum EF HC-PCF is ~60 nm, a finding which has not been established previously.

Another interesting point to note is that EF HC-PCF and EF CUV values are almost coinciding for AgNP sizes below 40 nm, and diverge for equal or greater sizes. As well, the enhancement factor of AgNP in HC-PCF (EF HC-PCF) exceeds the value of AgNP in cuvette by a factor of ~2 for the 60 nm optimal size. This because HC-PCF has a higher interaction length for the modal field to overlap with the sample. We also speculate the formation of additional ‘hot spots’ which might have been created within the assembly of the AgNP and R6G molecules, due to the laser light induced aggregation/agglomeration of AgNPs within the HC-PCF core volume [125]. Also, surface effects governed by nanoparticle size play an equally important role in the enhancement of Raman signals within the HC-PCF.

5.2.2.4 Overall enhancement and individual contributions of NP and HC-PCF toward SERS signal enhancement

The next phase involved measuring the total contribution of HC-PCF and nanoparticles in the overall enhancement of the Raman signal of R6G in HC-PCF. To do this, we defined another parameter (EF_{Total}) as the ratio of the SERS signal of R6G in HC-PCF and the normal Raman signal of R6G in cuvette. The EF_{Total} was calculated for different AgNP sizes while keeping the optimal volume ratio of AgNP and R6G (1:2), as discussed in Section 5.2.2.2.

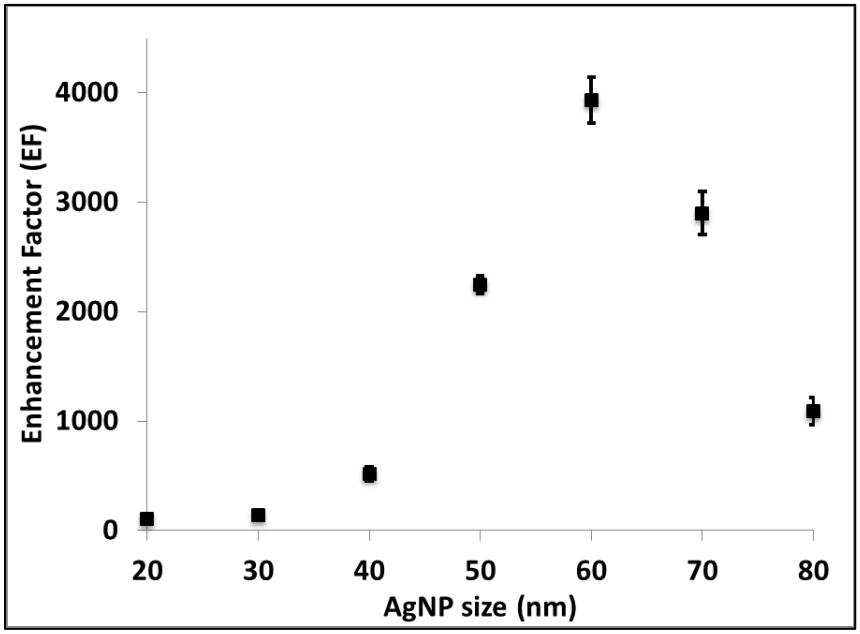

Figure 5-6 Enhancement factor vs AgNP size in HC-PCF and cuvette

Figure 5-6 shows the variation of EF_{Total} against the size (diameter) of AgNP. The trend of the curve is similar to that in Figure 5-5, the only difference being that the EF_{Total} is greater than EF HC-PCF or EFCUV corresponding to each AgNP size, which is expected as it is the measure of enhancement of the Raman signal of both AgNP and HC-PCF. The maximum overall enhancement factor was at an AgNP size of 60 nm, and calculated as ~4,000. The other point of observation is that the maximum value of EF_{Total} (~4000) is several times greater than the maximum value of EF CUV (~88) found earlier. The EF HC-PCF as calculated in

the previous section was ~43, while the HC-PCF alone (without nanoparticles) enhanced the Raman signal of any sample by a factor of ~90, as established in section 5.2.2. It is interesting that the experimentally calculated EF_{Total} values correlated well with the multiplicative product of EF HC-PCF and the normal enhancement factor of HC-PCF, for the pure R6G sample. This correlation applies to all AgNP sizes, with some deviation that can be attributed to factors such as light scattering by np or fluctuation in the sample throughput power in the HC-PCF. Thus, it can be concluded that 60 nm is the optimal size to achieve maximum enhancement of the Raman signal of R6G with nanoparticles in HC-PCF. These results also suggest that HC-PCF could support additional hot spots in the assembly of AgNP within HC-PCF, since the experimental value of EF_{Total} (~4000) for 60 nm AgNP is greater than expected value of EF Total (~3600), which is the multiplicative product of EF HC-PCF (~40) and enhancement factor of HC-PCF without AgNP (~90).

Figure 5-6 also shows that the error bar values for particles with diameters greater than 40 nm are, with an accuracy of 4 to 6%, relatively higher than those with diameters smaller or equal to 40 nm. This is mainly because the higher scattering of light by larger diameter AgNP, which affects light guidance in the HC-PCF. There is also the possibility of light induced agglomeration of nanoparticles that could have affected the light transmission within the HC-PCF, as reported earlier [124].

In summary, this study shows that an optimal size and volume of AgNP with respect to R6G, can achieve the maximum enhancement of a Raman signal in HC-PCF. In both HC-PCF and cuvette, the enhancing ability of AgNP depends on the volume and size, and reaches maximum when these factors exceed the amount of R6G by a factor of 2, then saturate in the bulk solution (cuvette). Our results indicate that it may not be possible to tap all the signal enhancing potential of AgNP, proportional to the volume, in HC-PCF. This is due to the low volume of AgNP in HC-PCF, beyond which the light scattering by AgNP dominates and limits the enhancement of the Raman signal. However, the cumulative effect of HC-PCF

and nanoparticles is much greater than their individual contributions to enhancing the Raman signal of test molecule (R6G). Therefore, the SERS based HC-PCF platform has the potential for trace-level detection of molecular species, if used with controlled volume and size of nanoparticles, as indicated here. The SERS based HC-PCF sensing platform for monitoring adenosine concentration and leukemia cells are tested in the next section.

5.3 Applications of the integrated biosensor (SERS and HC-PCF)

5.3.1 Monitoring adenosine

The optimum volume and size of nanoparticles was also used to demonstrate the application of the SERS based HC-PCF sensing platform for monitoring adenosine. Adenosine is considered an important molecule in clinical environments [117], owing to the role it plays in regulating extra-cellular physiological activity as discussed in section 4.4.5.

Adenosine was purchased from Lancaster Synthesis, and a 50mM stock solution was produced and used to prepare various sets of adenosine concentrations in the range of 1-25 mM. This range was chosen because it is the clinical level concentration of adenosine which is monitored in patients suffering from chronic obstructive pulmonary disease (COPD). Nanoparticles ~60$\pm$10 nm and their volume was kept half of the adenosine volume, for achieving maximum enhancement in the Raman signal of adenosine in HC-PCF. This AgNP size and volume ratio was made according to the results obtained with the test molecule (R6G), as described in the previous section. The silver nanoparticles were prepared according to the conventional citrate reduction method reported by Lee and Meisel [126]. The SERS spectrum of adenosine that was put into the HC-PCF and cuvette is shown in Figure 5-7.

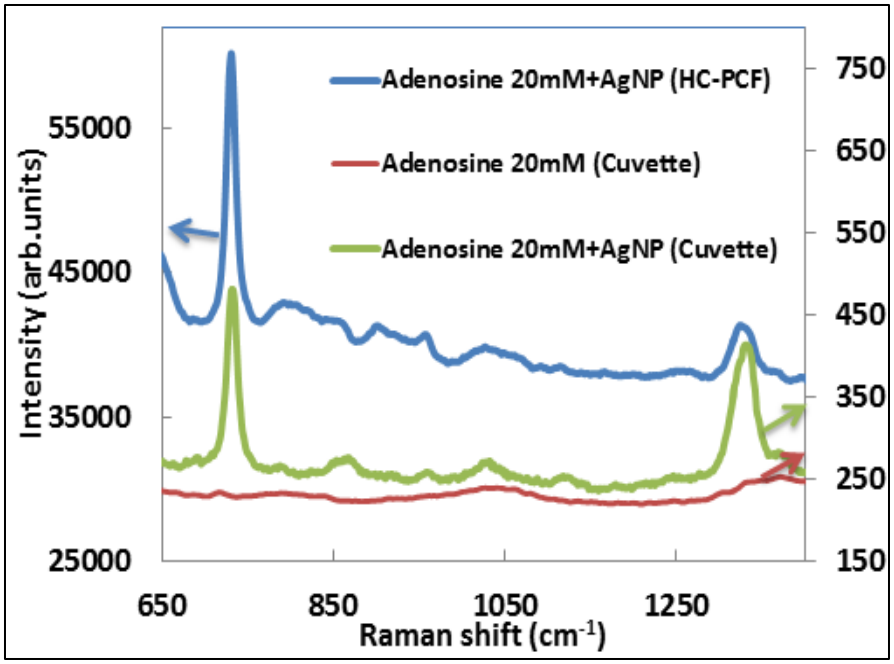

Figure 5-7 SERS spectrum of adenosine in HC-PCF and cuvette. Raman spectrum of adenosine in cuvette

The SERS spectrum of adenosine mixture showed prominent Raman peaks within the spectral range of 700 to 1,600 cm^{-1}, and was well correlated to the Raman bands of adenosine shown by Chen *et al*. and Sanches-Cortes *et al*. [118, 127]. Nanoparticles enhanced the Raman signal of adenosine in the HC-PCF by a factor of ~3,700, which is close to the enhancement factor calculated for the R6G molecule in the previous section.

We then inserted various concentrations of adenosine and nanoparticles into the HC-PCF, and recorded the Raman signals for quantitative measurement of adenosine in sample mixtures of adenosine and nanoparticles. The intensity Raman peak of ~733 cm^{-1} was considered the parameter to evaluate the quantity of adenosine in the sample mixture. The spectral band intensity of Raman peak of adenosine ~733 cm^{-1} was calculated. Such calculations were performed for all spectra corresponding to a particular concentration of adenosine in water, and then averaged to obtain a single data point. As a result, errors due to fluctuations of Raman peak intensity was minimized. Finally, a calibration curve of the

averaged spectral band intensity of Raman peak as a function of the corresponding percentage composition of adenosine in the sample mixture was produced, as shown in Figure 5-8.

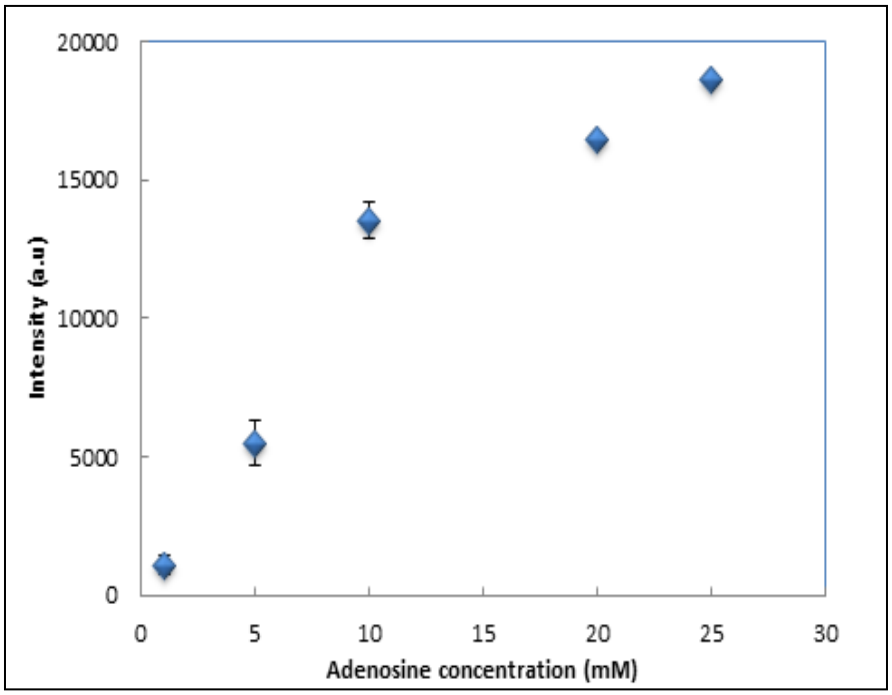

Figure 5-8 SERS peak intensity varying with different concentrations of adenosine in HC-PCF

We established that the SERS based HC-PCF sensing platform is highly sensitive when the nanoparticles size is ~60 nm. Further, we demonstrated the application of HC-PCF sensing platform (with the optimal size and volume of nanoparticles) to detect adenosine concentration in the range of 2 to 25 mM. The physiological level of adenosine monitored in clinical environments is approximately in the millimolar (mM) range. Hence it is important that the optimized SERS based HC-PCF sensing platform, as reported in this work, must able to detect adenosine concentration in the millimolar range in order to meet this requirement of adenosine monitoring in real clinical environment [128-129]. Reversed-phase high performance liquid chromatography (HPLC), coupled with UV-absorbance or fluorescence detection, is a popular and sensitive method of detecting adenosine. Though it has better detection sensitivity than our proposed approach (i.e. less

than nanomolar), HPLC is quite expensive and prone to low temporal resolution and tissue damage [130]. With further research, our proposed method has the potential of detecting adenosine at the level required in clinical environments.

5.3.2 Monitoring leukemia cells

The SERS based HC-PCF platform was also used to detect malignant cells, such as HL60 acute myeloid leukemia (AML), one of the most repetitive pediatric cancers and the leading cause of disease-related morbidity in children and adolescents [131-132]. AML causes abnormal production of blast cells in bone marrow, and if untreated it suppresses normal production of platelets and white blood cells within weeks, leading to life threatening bleeding and microbial infections. Thus, early detection of AML [133], and evaluation of minimal residual diseases (MRD) after treatment, can extend a patient's life expectancy. The current standard techniques, including flow cytometry [134], polymerase chain reaction [135], immunohistochemistry [136], microarray [137] and fluorescence based assays [138] are relatively difficult, time-consuming and costly to implement. Accordingly, developing cheaper and faster technologies for AML detection remains a major challenge.

5.3.2.1 Enhancement of Raman signal with HC-PCF and nanoparticles

HL60 acute promyelocytic leukemia cells (ATCC® CCL-240) were cultured in Iscove's Modified Dulbecco's Medium (Sigma), and supplemented with 20% fetal bovine serum, 1% antibiotics (streptomycin and penicillin) and 0.1% gentamicin. The cells were incubated at 37ºC, with 5.0% CO2 and 100% humidity, and cell density was maintained at 0.1 to $1.0x10^6$ cells/ml. Apoptosis was induced by incubating the cells with 5.0 µM (S)-(+)-Camptothecin (CPT) (a topoisomerase I inhibitor) [139-141] for three hours in Hanks Buffer (Sigma) with a $1x10^5$ cells/ml density. The cells were centrifuged at 1,000 rpm for 5 minutes and the pellet was re-suspended in 100 µL ($1x10^6$ cells/ml cell density) of Annexin binding buffer (Life Technologies), then 1.0 µL of 50 µg/mL propidium iodide (PI) and 5.0 µL Annexin V-FITC were added. The mixture was incubated at room temperature for 15

minutes, and another 400 µL of Annexin buffer was added to the mixture prior to sorting in a BD FACS-Aria flow cytometer. Cell sorting was carried out by gating non-stained cells (live), PI and annexin V positive staining (necrotic λ_{exc}= 488 nm, λ_{em}= 585±21 nm), and Annexin V positive (apoptotic λ_{exc}= 488 nm, λ_{em}= 530±15 nm). In all cases, cell numbers were measured with a Vi-Cell (Beckman Coulter). Additional experiments were carried out for the non-stained cells, following the scattering profile in the flow cytometer. In those experiments, the total number of cells varied between 25,000 and 310 cells/mL, when using serial dilution in the cell culture medium without phenol red. Control experiments were also performed without cells, following the same dilution procedure of the cell culture medium.

We focused on recording Raman spectra from HL60 cells $1x10^6$ cells/ml in cuvette and mixture of nanoparticle in HC-PCF. The Raman spectra of leukemia cells in cuvette is shown in Figure 5-9 which has peaks at 1032 cm^{-1}(C-N stretching mode of phenylalanine) and 1318 cm^{-1} (protein). The mixture of leukemia cells and nanoparticles in HC-PCF produced a rich spectrum with obvious features are around 650 cm^{-1} (protein:C-S stretching, tryptophan: C-N stretching), 722 cm^{-1} (C-H rocking of CH2 methylene group in lipids), 789 cm^{-1} (O-P-O ring breathing modes of DNA/RNA bases), 1003 cm^{-1} (symmetric ring breathing mode of phenylalanine), 1032 cm^{-1} (C-N stretching mode of phenylalanine), 1318 cm^{-1} (protein), 1436 cm^{-1} (C-H bending of lipids) [132, 142]. In this experiment our aim was to determine the factor by which HC-PCF and nanoparticles enhance the Raman signal, which we found to be 2,700 which is close to the range we reported with other biomoelcuels. The HC-PCFs are known to enhance the Raman signal as it supports strong modal field overlap with the sample due to its photonic band gap property. The enhancement factor of the sensor was calculated by dividing the Raman signal of leukemia cells and nanoparticles from HC-PCF by the Raman signal of leukemia cells from cuvette.

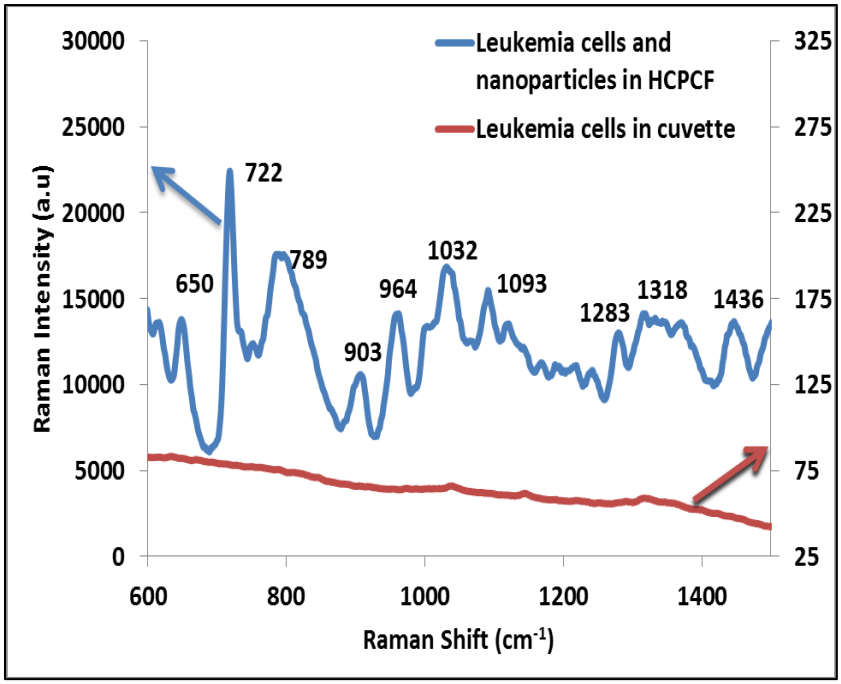

Figure 5-9 Enhancement of Raman signal of HL60 cells in HC-PCF using silver nanoparticles

5.3.2.2 Distinguishing different leukemia cell cycle stages

In the next phase, statistical analysis was used to distinguish the cell cycle states. Principal component analysis (PCA) and partial least squares (PLS) are very important aspects of multivariate data analysis, and are used to verify and detect classification and minimum levels of different leukemia cells. The Unscrambler version 10.3 (CAMO, Corvallis, OR, USA) was used to perform the multivariate data analysis. In PCA analysis the variations in the data set were used for identification and interpretation. The projection of X-variables (spectral wavelength) and Y-variables (analytical data) to a new space of so-called principal components (PC) is the basis of PCA. The first PC is defined as the direction of the most variations in the Y-variable, and the second PC, which is orthogonal to the first, is defined as the direction of the second-most variance (that not described by the first PC), and so on. The scores show the similarities or differences among the samples, with similar samples having close scores in the same PC. The plotting of PCs against one another can be used to interpret the structure of observation, and

reveal the hidden structure of the spectra. The score plot of PC1 and PC2, shown in Figure 5-10, shows the different groups in the samples. PCA analysis on the different cycle stages of live, necrotic and apoptotic HL60 cells yields a distinct Raman signature which is clearly distinguishable.

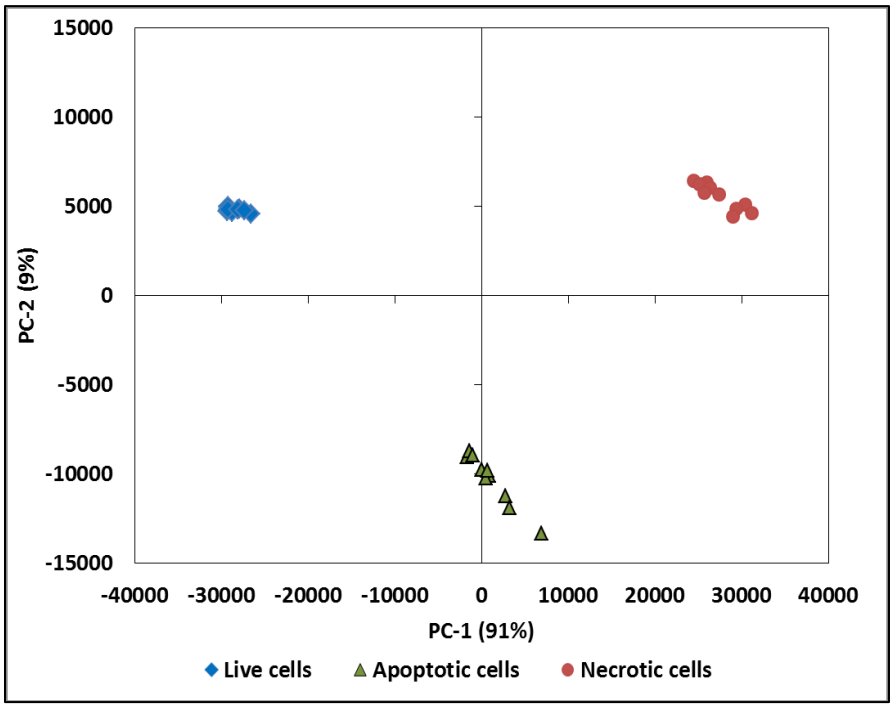

Figure 5-10 Plots of principal component analysis (PCA) of Raman spectra of different leukemia cell stages, showing distinct live, apoptotic and necrotic cell stages.

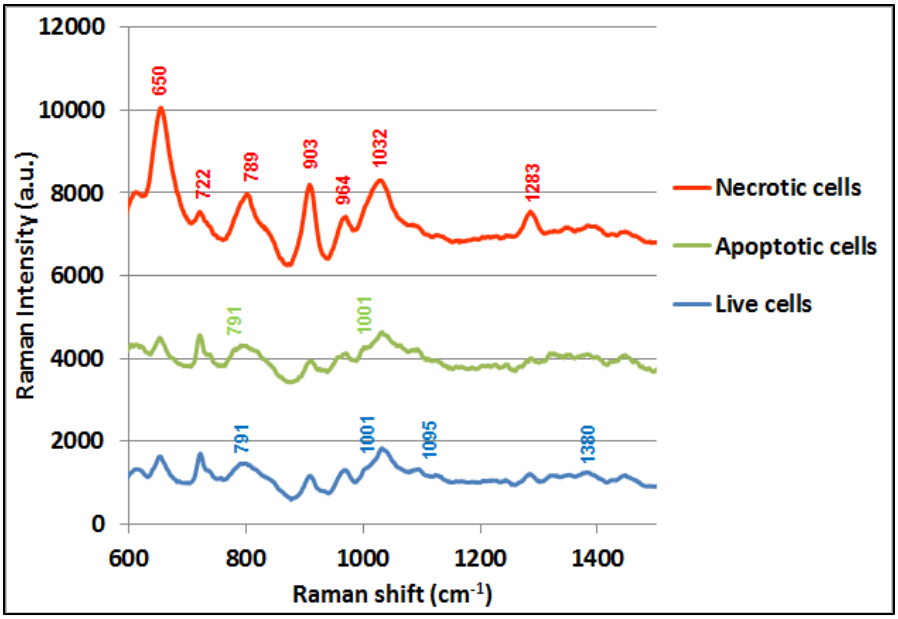

Figure 5-11 Raman spectra of leukemia cells cycle stages with distinct Raman peaks in live, apoptotic and necrotic cells.

Figure 5-11 shows the Raman spectra of different cell cycle stages, and indicates the variation of Raman intensity at key wavenumbers. Most of the necrotic Raman bands show higher intensity than the live and apoptotic cells, except at 722 cm^{-1} and 1001 cm^{-1}. As well, the average intensity of bands in apoptotic cells is higher than in live cells. These spectra, along with the score plot of PCA, allows us to distinguish these cells from each other.

5.3.2.3 SERS in HCPCF for different Leukemia cells concentrations

We next recorded the Raman spectra of different concentration of leukemia cells and nanoparticles in HC-PCF. Figure 5-12 shows the SERS spectra at six different concentrations of leukemia cells. As discussed earlier, the Raman peaks at 650 cm^{-1} (protein C-S stretching, tryptophan C-N stretching), 722 cm^{-1} (C-H rocking of CH_2 methylene group in lipids), 789 cm^{-1} (O-P-O ring breathing modes of DNA/RNA bases), 1,003 cm^{-1} (symmetric ring breathing mode of phenylalanine), 1,032 cm^{-1} (C-N stretching mode of phenylalanine), 1,093 cm^{-1} (O-P-O symmetric stretching mode of protein), 1,119 cm^{-1} (C-N stretching mode of protein), 1,318 cm^{-1} (protein) and 1,436 cm^{-1} (C-H bending of lipids) were the prominent peaks of

different concentrations of the samples. Once the Raman spectra of different concentrations of HL60 cells were recorded, we applied multivariate analysis to correlate the Raman signal with the sample concentrations.

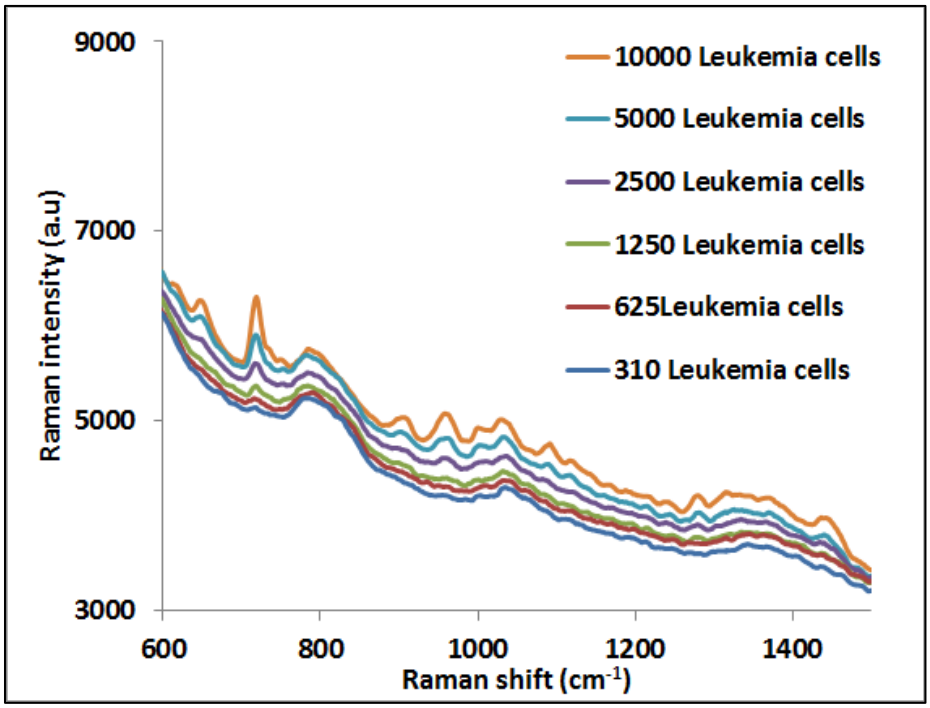

Figure 5-12 SERS spectra of different concentrations of live HL60 cells, expressed as cells/ml

In PLS analysis, the spectral data are used to generate a calibration model, which is then used to predict the dependent variables, such as analyte concentrations, by using the spectral response of the analyte. Validation of the PLS model is an essential requirement of data processing, as it in turn verifies the generated model. Full cross validation (FCV) and test set validation (TSV) are two techniques used to validate a model. With FCV, one spectral dataset is left out of the validation, while the remaining datasets are used to develop the calibration model. FCV is then repeated for every sample in the dataset. With TSV, the spectral data is split into two parts. One part is the spectral data used to make a model, and the other is the spectral data to fit into the model to compare the computed value with the observed value for the samples.

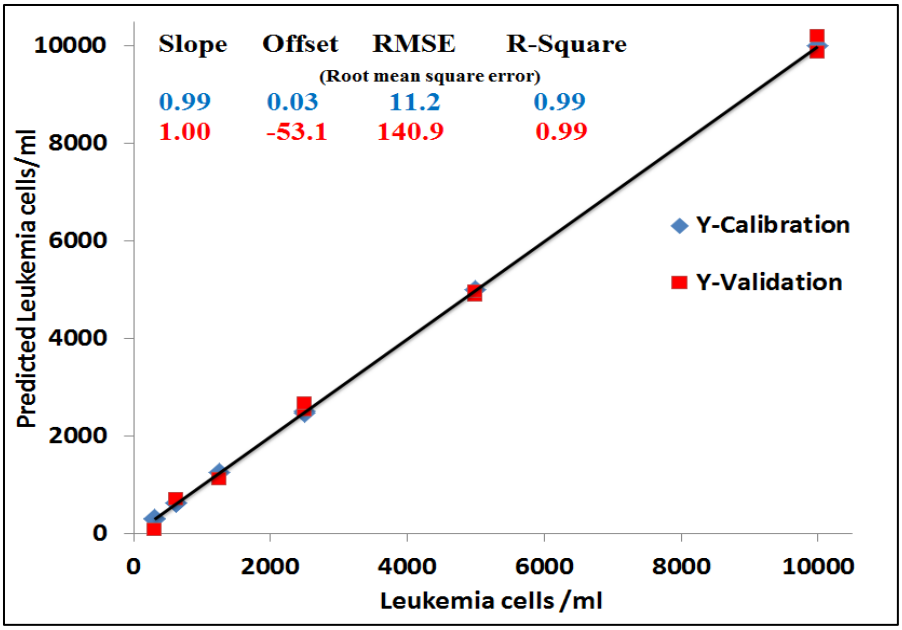

Figure 5-13 PLS prediction of different concentrations of leukemia cells/ml showing excellent correlation between calibrated and predicted samples with R^2 = 0.99 (linear fit y = 0.999x + 0.0366) and RMSEC and RMSEP of 11 and 140 cells/ml respectively.

Model performance can be expressed in terms of statistical parameters, including root mean square error of calibration (RMSEC), root mean square error of prediction (RMSEP) and coefficient of determination (R^2). The Raman spectra of six samples were recorded, and to ensure repeatability of measurement for each sample ten Raman spectra were also recorded. The Raman spectra of the six samples were divided into three subsets: calibration, validation and test. The calibration and validation subsets were used to make the model, while the test subset was independent data used to evaluate the model. Three of recorded spectra were identified as outliers, and were not used by the Unscrambler software to make the model. According to the PLS model of 45 records of samples in the calibration and validation sets, R^2 (for calibration and validation) was 0.99 and 0.99 respectively, RMSEC was 11 and RMSEP was 140. The calibration curve of this model is shown in Figure 5-13.

5.3.2.4 Comparing HC-PCF sensor with flow cytometry

Flow cytometry experiments using non-stained cells were also performed in order to compare the technique with our HC-PCF method. Figure 5-14 clearly shows the lack of linearity between the number of events detected by systems and the total number of cells in the solution. Indeed, compared to solutions without cells, the lower limit of detection was from 500 to 2,500 cells/mL. The red region in the bottom inset indicates the 500 cells/ml limit we consistently found as background under our experimental conditions (see right hand panels), and the upper inset shows the point where the 2,500 cells/mL limit does not correlate with the total number of events detected by the equipment. Furthermore, the Figure 5-14 plot has an upward curvature, which also indicates poor correlation between the actual number of cells in the sample and those detected by the system.

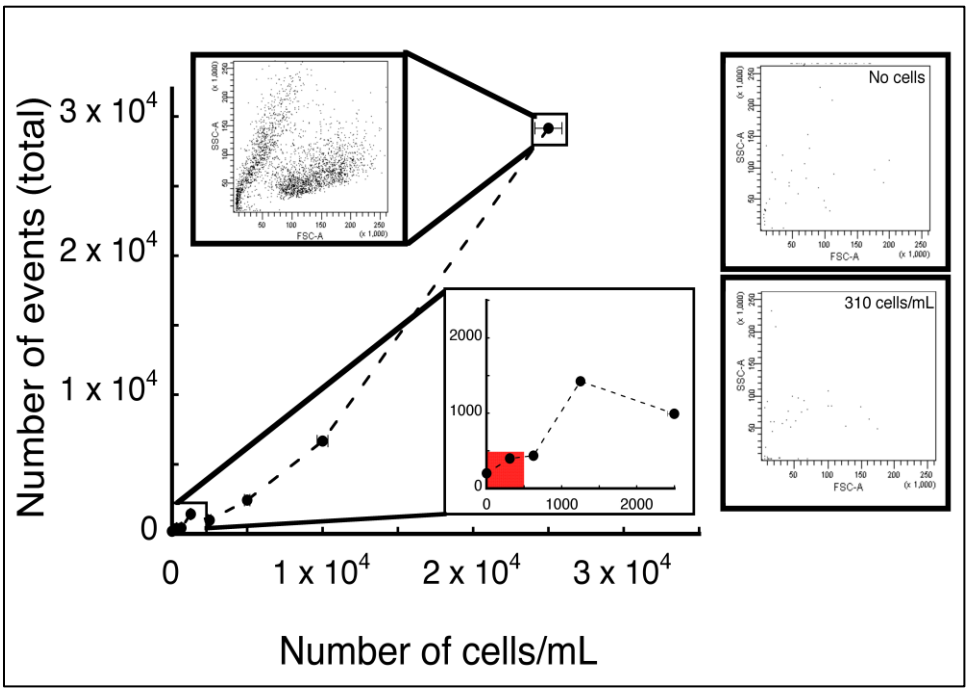

Figure 5-14 Number of events vs. total number of cells/mL for HL60 cells

The number of events was quantified by using the scattering upon 488 nm excitation of a non-stained cell suspension. The top inset shows the scattering profile for the sample containing 25,000 cells/mL, and the bottom inset shows the magnification for the lower cell numbers, with the red area indicating the noise

region or lower limit of detection for the system. The panels on the right include the scattering profile for the sample with 310 cells/mL, and a control solution without any cells, which clearly shows the close similarity between the two plots.

5.4 Conclusion

This research experimentally determines an optimal volume and size of silver nanoparticles to achieve maximum enhancement of the Raman signal in HC-PCF for rhodamine 6G (R6G) as a test molecule. It suggest that a volume ratio of spherical silver nanoparticles (AgNP) and R6G of 1:2, and an AgNP diameter of approximately 60 nm makes a SERS based HC-PCF the most sensitive sensing platform. We demonstrated the robustness of the platform for monitoring clinically important molecules such as adenosine, and leukemia cells.

Publications from this work:

P4. V. S. Tiwari, **A. Khetani**, A. Momenpour, and H. Anis: “Optimum size and volume of nanoparticles within hollow core photonic crystal fiber.” IEEE Journal of Selected Topics in Quantum Electronics 20, 7300608 (2014).

Novelty: This paper investigates the effect of the volume and size of silver nanoparticles (AgNP) on a surface enhanced Raman scattering (SERS) signal of rhodamine 6G (R6G) in a hollow core photonic crystal fiber (HC-PCF). Though other studies enhanced the weak Raman signal in HC-PCF and nanoparticles, the degree of enhancement was inadequate to understand the actual contribution of HC-PCF and nanoparticles to the overall enhancement of a Raman signal. Moreover, determination of the optimal size and volume of np to achieve the maximum SERS signal in HC-PCF has not been previously investigated, which has limited the capability of the SERS-based HC-PCF sensing platform to be used in practical diagnostic applications. Thus, this paper focused on experimentally

determining the optimal size and volume of spherical-shaped silver nanoparticles (AgNP) to achieve the maximum sensing potential of a SERS based HC-PCF platform. The study evaluates the contribution of HC-PCF and nanoparticles to the overall enhancement of the Raman signal of rhodamine 6G (R6G) as a test molecule. The optimum volume and size of the nanoparticles were used to demonstrate the ability of a SERS based HC-PCF sensing platform to monitor adenosine, a clinically important molecule.

P5. V. S. Tiwari, **A. Khetani**, A. Momenpour, H. Anis and V. Trudeau: "Detection of neurotransmitters by surface enhanced Raman scattering (SERS) within hollow-core photonic crystal fiber." SPIE Photonics West 8233-28 (2012).

Novelty: The work in this paper explores the feasibility of using surface enhanced Raman scattering (SERS) for detecting neurotransmitters such as glutamate (GLU) and gamma-amino butyric acid (GABA). These amino acid neurotransmitters mediate fast excitatory and inhibitory neurotransmission in the brain which is important for neuroendocrine control, and disturbances in their synthesis has been linked to epilepsy. The paper is driven by a need to rapidly monitor these neurotransmitters in micro-litre solutions, as required in clinical environments. Our experimental procedure involved matching excitation wavelengths to those of the band-gap shifted transmission band maxima of the non-selectively sample filled HC-PCF. The light remained strongly guided within the fiber, which resulted in major enhancement of the Raman signal from the analyte. This detection technique is particularly relevant in clinical environments, where the extraction of minimal biological fluids, such as cerebrospinal fluid, saliva and blood, is critical. Using HC-PCF to measure the amount of neurotransmitters (GABA, GLU) is an extension of our previous work, the non-selective filling of HC-PCF to detect a clinically important molecule (heparin) in serum.

P6.**A. Khetani**, A. Momenpour, E. Alarcon and H. Anis: “Hollow core photonic crystal fiber for monitoring leukemia cells using surface enhanced Raman scattering (SERS)”, Biomedical Optics Express 6, 4599-4609 (2015)

Novelty: The novelty of this work is the development of a sensor platform for the detection of leukemia cells that is antibody-free, robust, fast and portable, using Raman spectroscopy with a 785 nm laser diode and a hollow core photonic crystal (HC-PCF) containing silver nanoparticles. Acute myeloid leukemia is one of the most common bone marrow cancers in children and youths, and clinical studies suggest that early diagnosis and remission evaluation of myoblasts in the bone marrow is key to improving patient survival rates. However, the current protocols for leukemic cell detection involve the use of antibodies and flow cytometers, which is expensive. We have developed a new method for detecting leukemia cells up to 300 cells/ml using a compact fiber HC-PCF, which is a novel and cheaper alternative to existing clinical standards. We were also able to accurately distinguish live, apoptotic and necrotic leukemic cells.

P7.**A. Khetani**, V. S. Tiwari, A. Momenpour and H. Anis: “Monitoring of adenosine within hollow core photonic crystal fiber by surface enhanced Raman scattering (SERS).” In: 2011 11th IEEE Conference on Nanotechnology (IEEE-NANO), 973 (2011).

Novelty: The novelty of this work is interfacing SERS with HC-PCF while exploiting the photonic band gap property of a non-selectively filled HC-PCF with adenosine and silver nanoparticles. The high sensitivity, accuracy along with a minimal test sample (micro-litre) requirement makes the presented optical sensing scheme an attractive candidate for adenosine monitoring in clinical settings. Furthermore, SERS has the inherent advantage of molecular specificity and high detection sensitivity, making it relevant in clinical environments. SERS spectrums of various concentrations of adenosine and water were recorded in cuvette. Prior to

filling the sample solution in HC-PCF, simulation with COMSOL were performed to ensure that the modal field in a sample filled HC-PCF is strictly confined within the core volume of HC-PCF. Finally, we then compared the SERS signal of adenosine in HC-PCF to that obtained in cuvette.

P8. V. S. Tiwari, **A. Khetani,** M. Naji and H. Anis: "Study of Surface Enhanced Raman Scattering (SERS) within hollow core photonic crystal fiber." IEEE Sensors Conference, 5404 (2009).

Novelty: This work aims to realize the surface enhanced Raman scattering (SERS) signal of the rhodamine 6G (Rh 6G) molecule, by non-selectively filling all the holes of a hollow core photonic crystal fiber (HC-PCF) and exploiting its bandgap property. A strong mode field overlap with the analyte solution was achieved, resulting in an amplified Raman signal with only a few milliwatts of sample energy in the fiber core. The actual enhancement by HC-PCF was deconvolved from that of the nanoparticles in the overall Raman signal enhancement of Rh 6G. Finally, the paper reported the enhancement factor of Raman signal of Rh 6G in different lengths of HC-PCF.

Chapter 6. HC-PCF for efficient two-photon induced photochemistry

6.1 Introduction

This chapter demonstrates that a hollow core photonic crystal fiber (HC-PCF) significantly enhances the efficiency of two-photon photochemistry. Two photon induced photochemistry not only presents interesting photochemical phenomena, but it can also can be useful in applications such as two-photon microscopy and photodynamic therapy. Although two-photon photochemical reactions are difficult to achieve in small volumes, we addressed this limitation by using a novel HC-PCF platform, to efficiently perform the two-photon induced photodecarbonylation reaction of a cyclopropenone and its conversion to the corresponding acetylene (as shown in Scheme 6-1). The simple optical design configuration involves an 800-nm tsunami laser, where light is coupled into a short piece of HC-PCF filled with the sample. With this approach, we were able to increase the efficiency of two-photon induced photochemistry by a factor of 80, compared to a conventional spectrophotometer cuvette. Thus, this work will lead to the inclusion of HC-PCFs in researching two-photon induced photochemistry processes, which was previously limited by the difficulty to detect photochemical events at small excitation volumes.

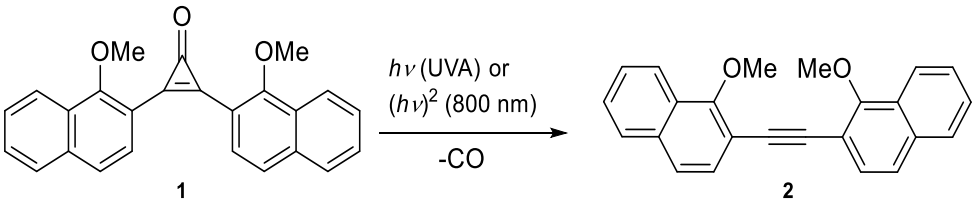

Scheme 6-1: Photoconversion of 1 into alkyne 2

In this chapter we first discuss two-photon mechanisms and applications, followed by the challenges to achieving two-photon molecules and processes. In Section 6.3, we examine the experimental details for performing two photon experiments, and describe the preparation of Cyclopropenone. The next sections present the data and HPLC analysis of the photo conversion process, which indicate the increased efficiency of two-photon induced photochemical process with HC-PCF.

6.2 Two-photon process theory and applications

Experimental observations of multi-photon absorption (MPA) [143], second harmonic generation [144], stimulated Raman scattering [145] and other similar phenomena in the early 1960's marked the beginning of nonlinear optics. Molecules with multi-photon induced optical properties interest researchers, due to the underlying scientific principles and their potential for industrial applications. Two-photon absorption (TPA) is a multi-photon process in which a molecule absorbs two photons simultaneously. The main advantages of two-photon over one-photon processes are the prospect of excitation of materials with high three-dimensional spatial resolution, and deep light-penetration into absorbing materials. TPA was quickly established as a particularly useful spectroscopic technique, and it eventually became a unique source of information about atomic and molecular structure [146-148]. Due to the rapid development of powerful lasers, both TPA and MPA (i.e. n>2) have been studied in a wide variety of materials. Over the past two decades, nonlinear absorption in organic molecules, semiconductor bulk materials, semiconductors and metal nano-materials has been investigated significantly, both experimentally and theoretically.

TPA is a nonlinear optical process in which two photons are absorbed simultaneously, such that the energy of the photons adds up to the energy of the excited atom or molecule:

$$h\nu_1 + h\nu_2 = E \tag{6.1}$$

where *h* is the Planck constant, ν_i is the frequency of the i-th absorbed photon, and *E* is the transition energy [149]. The absorption of all the photons is simultaneous in the sense that there are no real intermediate energy levels involved in the process. The absorption takes place through so-called virtual levels (see Figure 6-1), the existence of which has been verified by quantum mechanics.

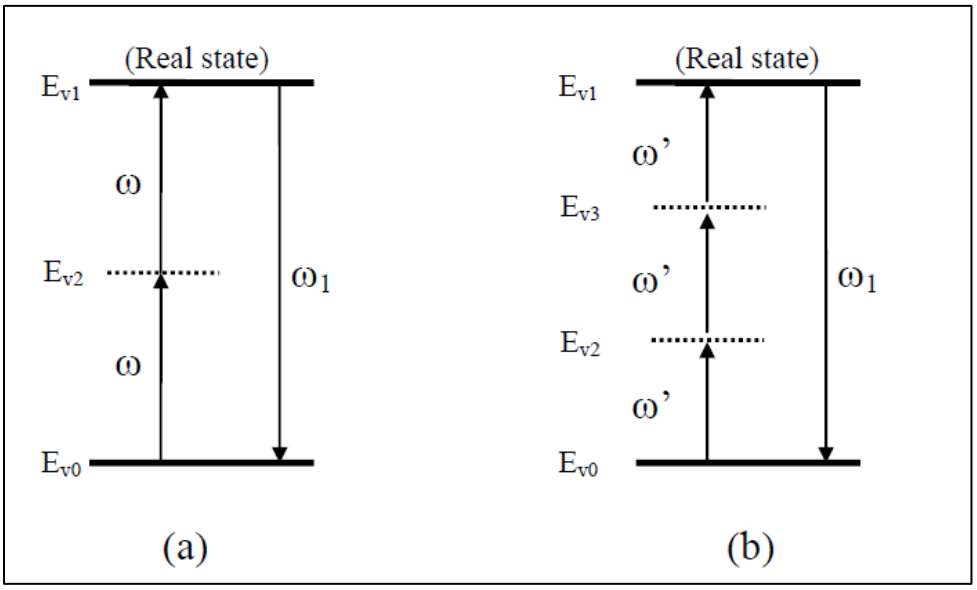

Figure 6-1 Schematic diagrams showing two-photon absorption and three-photon absorption in a two-energy-level system

Currently, two main factors have steered two-photon processes in a new direction. The first is the development of mode-locked ultrafast lasers in the 1990s, which provided a source of extremely high peak intensity light pulses that facilitate instantaneous two-photon processes. In addition, there is an increasing demand for efficient two-photon absorbers, particularly chromophores that are compatible with new technological and biological applications. Several practical applications of TPA have been put forward, such as ultra-short pulse characterization [150-151],

frequency upconversion lasing [152], two-photon excitation microscopy [153], three-dimensional (3D) ultra-high density optical data storage [154], 3D microfabrication [155], optical power limiting [156] and photodynamic therapy (PDT) [157,158]. There are many other unique properties that make TPA attractive for several practical applications, including:

- quadratic dependence of absorption rate on the excitation intensity ($\sim I^2$);
- instantaneous response time;
- the possibility to selectively excite molecules in a small volume $\sim \lambda^3$;
- the substantial difference between excitation wavelengths and fluorescence wavelengths; and,
- deeper penetration of near-IR light, typically used for two-photon excitation into tissues.

6.2.1 Challenges

The success of two-photon-based applications is critically dependent on the efficiency of TPA, particularly the value of the intrinsic nonlinear cross section σ^2. In addition, two-photon excitation (TPE) depends on the square of the laser beam power density; thus the efficiency of TPE is greatest at the focus of a highly focused beam. The miniscule excitation area in a conventional cuvette-based setup makes studying two-photon-induced processes very challenging. The minute quantity of photoproducts generated in the reaction cannot be analyzed in situ by conventional spectroscopic or analytical techniques, as it is effectively diluted in the macroscopic sample, which is usually milliliters. Moreover, TPA experiments in free space must contend with self-focusing effects at high laser powers and unavoidable diffraction, which cause the beam to spread out and reduce its intensity as it propagates. As a result, the effective length of interaction of the beam with the medium (known as the Rayleigh length), gets shorter when attempting to enhance the nonlinearity in the medium by focusing the beam more tightly. HC-PCF's have also been used to study single-photon photochemistry processes. In an earlier attempt, we showed the laser flash photolysis process

using HC-PCF by detecting triplet state decay for samples such as xanthone in toluene and acetonitrile, and benzoin soluble in water in the presence of methyl viologen. The experiments resulted in bringing down the sample volume to 10^{-4} μl with signal improvements of at least one order of magnitude [108]. Williams *et al*., demonstrated the potential of photonic crystal fibers as optofluidic elements in lab-on-a-chip devices for photochemical applications, by measuring the kinetics of the photochemical and thermal cis-trans isomerisation of sub-picomole samples of two azo dyes [159]. Cubillaus *et al*., studied the well-known photoaquation of the metal complex vitamin B12 (cyanocobalamin, CNCbl), as well as photocatalytic system, the photo-Fenton chemistry [160]. Stawska *et al*., theoretically demonstrated that double clad hollow core fiber (DCHCF) significantly affects the efficiency of collecting a two-photon fluorescence signal. With the sample 10 mm from the face of the fiber, the minimum enhancement of collection efficiency is three times that of commercially available fibers [161].

Recently, TPA was demonstrated in a Kagome lattice HC-PCF for the liquids fluorescein and R6G, at concentrations as low as 10^{-9} M at an irradiance of 9×10^{8} W cm^{-2} (average power of 30 mW) [162]. However, in this study two-photon absorption was achieved using a Kagome lattice fiber, which transmits a broader wavelength but is not readily available and is difficult to fabricate. In our research, we used HC-PCF from NKT Photonics and integrated it with a robust pressure driven microfluidic system to study ultrasensitive photochemical events in a small excitation volumes have been studied, and it represents a step further than TPA through induced photochemistry reactions.

6.3 Experiment

6.3.1 Experimental setup

A schematic of the experimental setup is shown in Fig. 6-2. Light from a tunable (between 700 and 1000 nm) Ti:sapphire laser producing ~65 fs pulses at an 80 MHz repetition rate was passed through a Faraday isolator (Electro-Optics Technology, Inc., Traverse City, MI) to reduce back reflections into the laser. The

dichroic mirror acted as a reflector for the laser beam, which was further focused onto the tip of the HC-PCF by a 40x microscopic objective lens (L1) with a numerical aperture (NA) of ~0.65. The HC-PCF was filled with a differential pressure system of parallel channels (tubing) for sample input/output. The perpendicular integration of HC-PCF with the parallel fluidic channels resembled a ├ shaped structure, as shown in the figure.

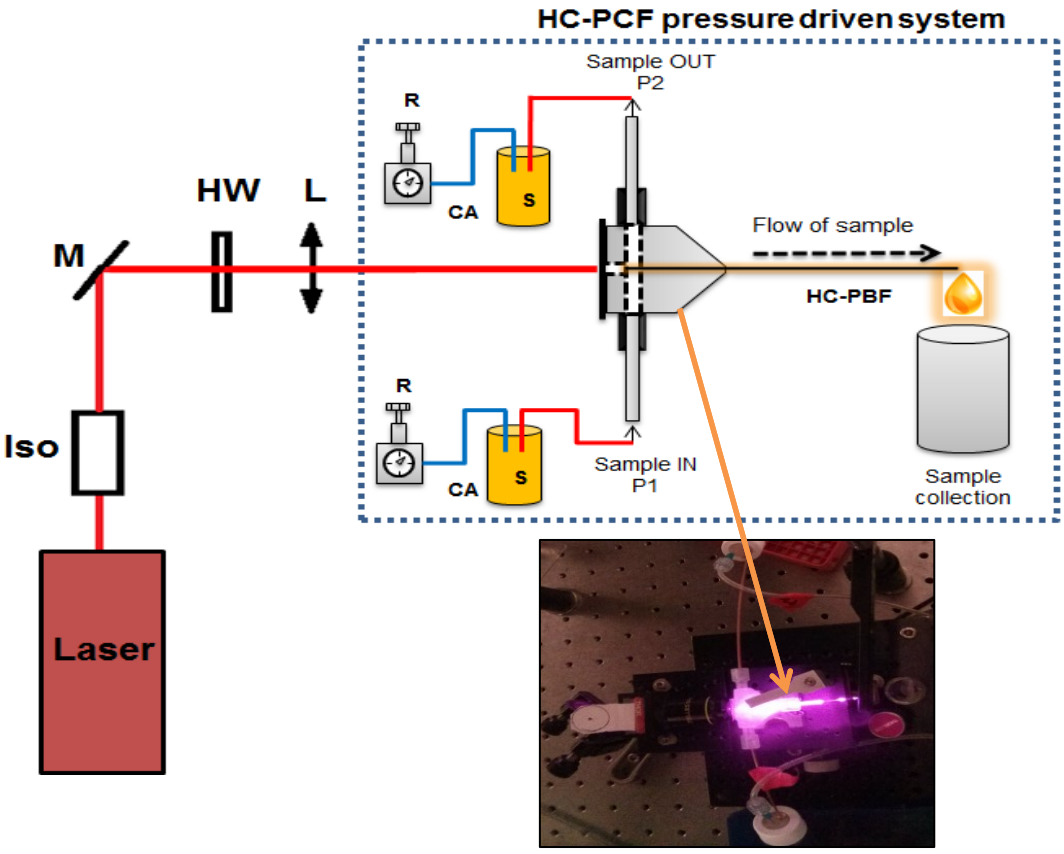

Figure 6-2 Schematic of the two photon photochemistry with HC-PCF setup. Laser – Ti:sapphire tsunami laser; Iso – Faraday Isolator; M – Dichroic mirror; HW – Half wave plate; L – Objective lens; S – Samples in the vials; CA – Compressed air; R – Regulators; HC-PCF – Hollow core photonic crystal fiber

6.3.2 Materials and methods

Methylene chloride (CH_2Cl_2) and acetonitrile (MeCN) were purified with a LC Technology Solutions Inc. SPBT-1 Bench Top Solvent Purification System, and

Milli-Q water (resistivity 18.2 MΩ cm^{-1} at 25 °C; 0.22 μm filter) was used for HPLC analysis. Chemicals were purchased from Sigma-Aldrich. All the reactions were monitored by thin-layer chromatography, using aluminum sheets coated with silica (60, F254). NMR spectra were recorded at room temperature with a Bruker Avance 300 spectrometer. High resolution ESI mass spectra in positive mode were acquired with a Micromass Q-TOF I in the John L. Holmes Mass Spectrometry Facility at the Department of Chemistry and Biomolecular Sciences, University of Ottawa. Absorbance spectra were recorded using a Cary 50 UV−visible spectrophotometer. HPLC analysis was performed with a Waters Integrity HPLC system coupled to a Waters 996 photodiode array detector, using a reverse phase Zorbax C18 column and an eluent mixture of MeCN and H_2O (95:5) with a flow rate of 0.25 mL/min in the presence of a standard (Coumarin 153). Retention times were 16.2 min (1), 19 min (Coumarin 153) and 23.6 min (2).

The synthesis of cyclopropenone 1: A solution of tetrachlorocyclopropene (69 μl, 0.56mmol) in CH_2Cl_2 (5 ml) was added in drops over the course of 30 min to a solution of and anhydrous AlC_{l3} (300 mg, 2.25 mmol) in CH_2Cl_2 (10 ml) at -78 °C. 2-methoxynaphtalene (178 mg, 1.125 mmol) in CH_2Cl_2 (5 ml) was then added in drops over the course of 30 min, and the mixture was stirred for 2 h at -78 °C. The solution was allowed to warm to room temperature, then stirred for an additional 3 h. The suspension was quenched with saturated ammonium chloride, extracted with water (3 x 15 ml) and brine (3 x 15 ml), and dried over $MgSO_4$. Upon removal of the solvent under reduced pressure, the solid product was recrystallized from a 20:1 hexanes CH_2Cl_2 mixture to yield 110 mg (53 %) of 1 as a solid. ESI-MS: 389.1 [M+Na]+. 1H NMR (300 MHz, $CDCl_3$): δ 8.2 (2H, d, 8.4 Hz), 7.95 (2H, d, 9 Hz), 7.75 (2H, d, 8 Hz), 7.5 (2H, m), 7.35 (2H, m), 7.18 (2H, d, 9 Hz), 3. 56 (6H, s). 13C NMR ($CDCl_3$): δ 158.5, 157.9, 144.9, 134.7, 133.4, 128.2, 125.2, 124.3, 112.1, 108.8 and 55.8.

The synthesis of 2: A 10^{-2} M solution of 1 in EtOH was irradiated in a Luzchem LZC-4 photoreactor equipped with UVA bulbs to obtain 2 in quantitative yield. ESI-MS: 361.4 [M+Na]+. 1H NMR (300 MHz, CDCl3): δ 8.6 (2H, d, 8.7 Hz), 7.8 (4H,

m), 7.6 (2H, m), 7.4 (2H, m), 7. 3 (2H, d, 9 Hz), 4.13 (6H, s). 13C NMR (CDCl3): δ 159.2, 134.8, 130.3, 129, 128.4, 127.7, 126.2, 124.6, 113.3, 81.5 and 57.3.

6.3.3 Refractive index of the samples

Table 6.1 shows the refractive indices of the cyclopropenone sample in ethanol. Based on the refractive indices and the equation, we determined that HC-1550 would be ideal for two-photon experiments. We used a variant of HC-1550 fiber (HC-19-1550), formed by removing 19 cells from the cladding so the core diameter becomes 20 μm. Figure 6-3 shows a cross-section view of the HC19-1550 fiber, and the mode-field pattern of the HC-PCF filled with the sample.

Sample	**Refractive Index @588nm**	**HC19-1550 band (nm)**
Air	1.00	1530 - 1610
Cyclopropenone in ethanol	1.36	781-822

Table 6-1 Refractive index of samples and the transmission band of HC-PCF

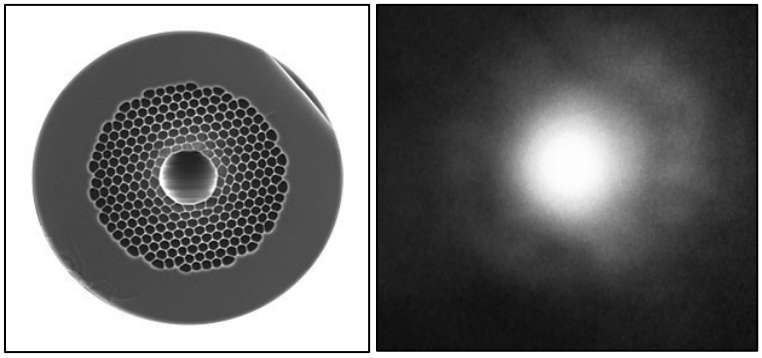

Figure 6-3 Hollow core Photonic Crystal fiber (HC19-1550 NKT Photonics)

6.4 Results and Discussions

Decarbonylation of cyclopropenone 1 (Scheme 6-1), is usually induced by UV irradiation [163-165]. Though the thermal decomposition of this compound requires temperatures above 150°C, 350 nm irradiation results in efficient decarbonylation and the quantitative conversion into the corresponding acetylene 2. In 2006, Urdabayev *et al*. showed the successful two-photon induced formation of acetylene 2 by irradiation of cyclopropenone 1 with 800 nm ultrashort pulses from a Ti-Sapphire laser [166] for the first time. We consider this reaction to be a reliable model for evaluating the efficiency of our photonic crystal fiber for two-photon induced photochemistry. The one photon absorption spectrum is illustrated in Figure 6-5. The maximum of absorption of 1 is at 390 nm.

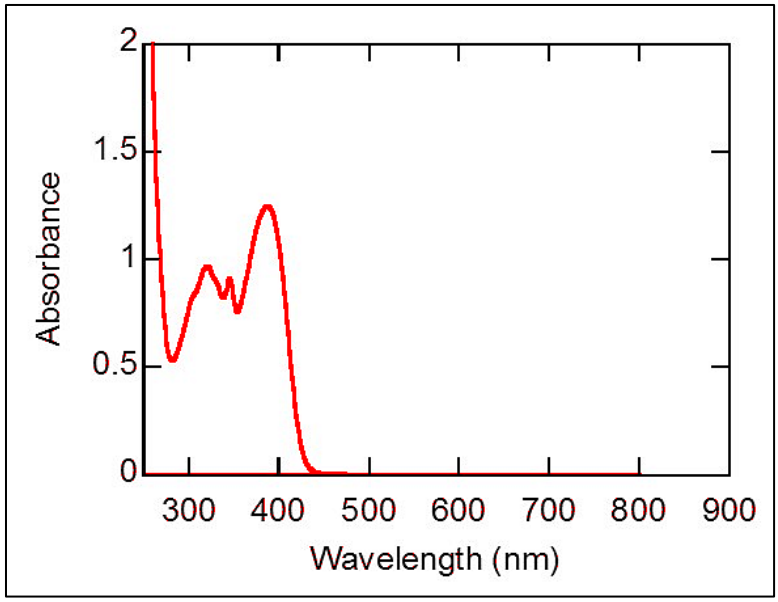

Figure 6-4 Absorption spectrum of a 10^{-4} M solution of 1 (EtOH, 25°C)

In order to perform two-photon induced photochemistry, a spectrometer cuvette of 10 mm path length was filled with 3 ml of 10^{-2} M in ethanol. The light from the tsunami laser was guided onto the cuvette with an M40X microscope objective lens. The sample was exposed to the laser for one minute, then removed and stirred well; this process was for repeated for 30, 60 and 90 minutes. The solutions were then analyzed for conversion of 1 $\rightarrow$ 2, using High Pressure Liquid

Chromatography (HPLC) in the presence of a standard. In the next step, TP induced photochemistry was performed using photonic crystal fiber. First, the fiber was filled with ethanol using a pressure driven system, and laser from fs pulsed laser was coupled with the fiber with 30% efficiency. The ethanol was then purged out of the fiber with water, and a 3 ml sample was loaded into a vial connected to a 10 cm photonic crystal fiber using a pressure driven system as described in the experimental section. The laser light was then coupled to the fiber with a coupling efficiency 5 to 10%. The average pressure applied to the fiber was 30 psi, which yielded a flow rate of 0.3 μl/min. Samples were collected every minute for 30 minutes to yield 10 μl volumes, which were analyzed for conversion efficiency using HPLC. The sample preparation and the synthesis and characterization of compounds 1 and 2 are described in the Experimental Section. The results are shown in Table 6-2.

Entry	Irradiation Time (min)	Volume(ml)	% yield of 2
A	30	3	1.28
B	30	0.01	79.2

Table 6-2 Percentage yields of 2 obtained by irradiating 10^{-2} M solutions of 1 with a 800 nm tsunami laser
(a) in quartz cuvettes (normalized) and (b) coupled with HC-PCF

The HPLC chromatogram for irradiation performed with the photonic crystal fiber is illustrated in Figure 6-5. Yield calculations show an increase of two-photon induced conversion efficiency by a factor of 80 compared to cuvette based geometry.

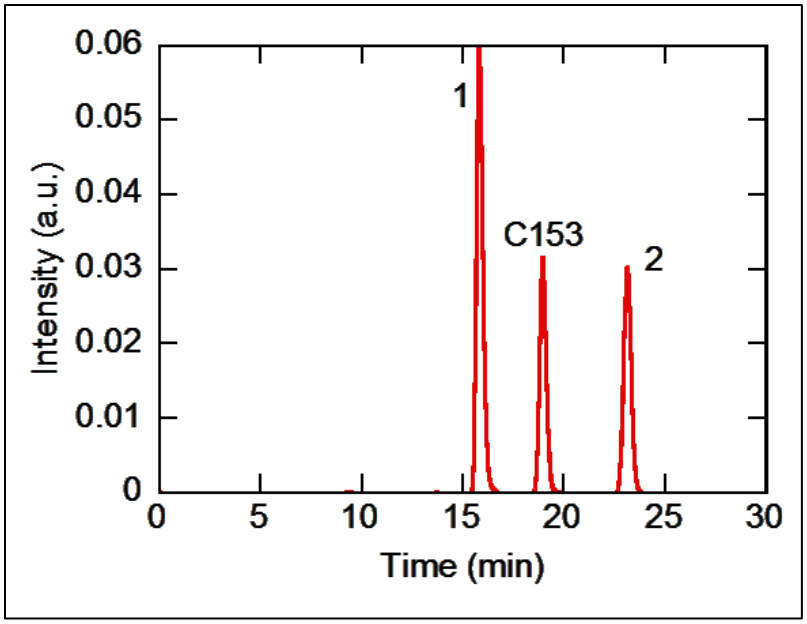

Figure 6-5 HPLC chromatogram with HC-PCF

390 μl of MeCN added to the irradiated sample Total volume = 10 μl. 200 μl of the mixture were then added to 200 μl of a 10^{-4} M solution of coumarin 153 standard. Area (2) = 827995; Area (C153) = 768663)

6.5 Conclusion

This work demonstrated, for the first time, that using a short piece of photonic crystal fiber can increase the efficiency of two-photon induced photochemistry. We compared the two-photon induced photodecarbonylation reaction of a cyclopropenone in both HC-PCF and cuvette, and found HC-PCF increased the yield efficiency by two orders of magnitude. This should lead to further study of two-photon induced photochemistry, as well as other applications such as photodynamic therapy.

Publications from this work:

P12. **A. Khetani,** S. Impellizzeri, J. C. Scaiano and H. Anis: Hollow core Photonic Bandgap Fiber for efficient two-photon induced photochemistry, ACS Photonics (to be submitted).

Novelty: The novelty of this paper is the use of hollow core crystal fibers (HC-PCF) to significantly enhance the efficiency of two-photon photochemistry. Although two-photon photochemical reactions are difficult to achieve in a small volume, this was overcome by using a novel platform of HC-PCF to perform the two-photon induced photodecarbonylation reaction of a cyclopropenone, and its conversion to the corresponding acetylene. The optical design configuration was simply an 800-nm tsunami laser with the light coupled to a short piece of HC-PCF filled with the sample. With this approach, we were able to increase the efficiency of two-photon induced photochemistry by a factor of 80, compared to a conventional spectrophotometer cuvette. Thus, HC-PCF provides a way to study two-photon induced photochemistry processes which was, until now, limited by the difficulty to detect photochemical events at a small excitation volume.

Chapter 7. Summary and Future work

7.1 Summary

The main objective of this thesis was to implement a novel, hollow core photonic crystal fiber (HC-PCF) to enhance a Raman signal, thereby providing a label-free, unique, robust and repeatable platform for biosensing applications. Two-photon photochemistry was one of the earlier attempts to implement HC-PCF to monitor photochemical reactions. A summary of the research and findings follows.

7.1.1 HC-PCF as a robust biosensing tool for monitoring chemicals

- In Chapter 2, I theoretically assessed the figure of merit (FOM), which is useful for evaluating different hollow core optical fibers. The chapter discussed hollow core photonic crystal fiber, including its bandgap and different filling techniques, and various reservoir configurations for filling HC-PCF. Using Surface Enhanced Raman Scattering (SERS) to enhance Raman signals by combing nanoparticles and HC-PCF was also reviewed in this chapter.

- In Chapter 3, I experimentally evaluated how different hollow core optical fiber configurations enhance the Raman signal of an analyte. Of the hollow core optical fibers considered, HC-PCF enhancement was superior; thus, it was chosen as the 'Raman signal enhancer.' I also evaluated Raman signals from different chemicals, and selected heparin, a highly important clinical molecule for surgery, as the sample of interest. HC-PCF sensor capabilities were found to be better in terms of accuracy, response time and sample volume, compared to existing clinical procedures.

- In Chapter 4, I demonstrated a method to use HC-PCF for repetitive characterization of multiple samples by Raman spectroscopy. This was achieved by integrating the HC-PCF with a differential pressure system that allowed effective filling, draining and refilling of samples to a HC-PCF under identical optical conditions. This proved that high-quality, reliable spectral data suitable for multivariate analysis (partial least squares) could be acquired, and I was able to accurately predict different concentrations of heparin and adenosine in serum. This detection scheme leads to the use of HC-PCFs in point-of-care technologies and environmental monitoring, where rapid sample characterization is critical

7.1.2 Integrating HC-PCF with nanoparticles

- In order to further improve the sensitivity of the HC-PCF based Raman sensor, I focused on implementing surface enhanced Raman scattering (SERS) by integrating nanoparticles in HC-PCF fibers. In Chapter 5, I investigated the effects of the volume and size of silver nanoparticles (AgNP) on the surface enhanced Raman scattering (SERS) signal of rhodamine 6G (R6G) in HC-PCF. The HC-PCF enhanced the Raman signal of R6G approximately 90-fold. In addition, the optimal size and volume of AgNP enhanced the Raman signal of R6G approximately 40-fold, resulting in a total enhancement of approximately 4,000 in HC-PCF. A comparison of AgNP enhancement factors in HC-PCF and bulk samples (cuvette) is presented at their optimal size and volume, with respect to R6G. The SERS based HC-PCF sensing platform was further utilized to monitor adenosine, a clinically relevant molecule, and the platform was also applied to detect leukemia cells. Compared to flow cytometry, this scheme detected as low as 300 leukemia cells/ml, thereby offering a novel alternative to existing clinical standards. Furthermore, I was able to accurately distinguish live, apoptotic and necrotic leukemic cells.

7.1.3 Two-photon induced photochemistry using HC-PCF

- In chapter 6, I demonstrated that HC-PCF significantly enhances the efficiency of two-photon photochemistry. Although two-photon photochemical reactions are difficult to achieve in a small volume, I was able to apply HC-PCF to efficiently induce two-photon photodecarbonylation reaction of a cyclopropenone, and its conversion to the corresponding acetylene. This simple optical design configuration involves coupling an 800-nm femtosecond tsunami laser into a short piece of HC-PCF filled with the sample. With this scheme, I was able to increase the efficiency of two-photon induced photochemistry by 80-fold, compared to a conventional spectrophotometer cuvette. This paves the way for an HC-PCF sensing platform for monitoring two-photon related processes in small volumes.

7.2 Future Work:

Here, we discuss the prospects of using HC-PCF based sensors in future work.

7.2.1 PDMS lab-on-chip system for the HC-PCF Raman sensor

In order to build a miniaturized reservoir and make the HC-PCF Raman sensor compact and portable, future work can concentrate on designing a lab-on-chip system. The integrated pressure-driven reservoir described in Section 4.2, uses a sample volume of approximately 70 μL, including all tubing, the cross and the HC-PCF itself (excluding the dead volume of the sample to maintain the differential pressure across the HC-PCF). This is far larger than the HC-PCF 50 nL volume. To achieve nL sample consumption and eliminate dead-volumes, future work could focus on building a microfluidic Polydimethylsiloxane (PDMS) on-chip solution for the HC-PCF sensor platform, as shown in Figure 7-1.

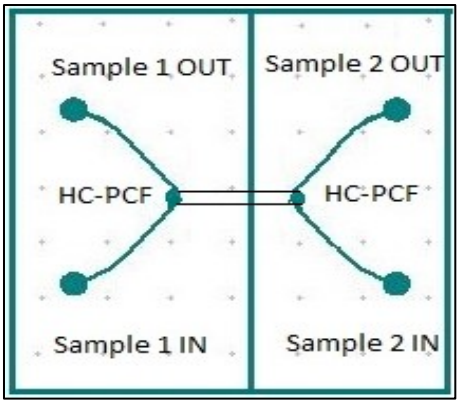

Figure 7-1 Microfluidic PDMS chip for HC-PCF sensor platform

7.2.2 Parallel sensing using HC-PCF

Parallel sensing is significant for continuous monitoring of chemical parameters in complex samples, including blood serum, food samples and bioreactor fluids used in the chemical industry [167]. Such sensors can provide sensitive and rapid online monitoring. One of the future applications of HC-PCF could be to fill each microchannel with different samples, through integration with a microfluidic system. Figure 7-2 demonstrates filling HC-PCF with two liquids that can be extended for multi-analyte sensing. One of the challenges to implementing this approach is preventing the two liquids from diffusing into each other.

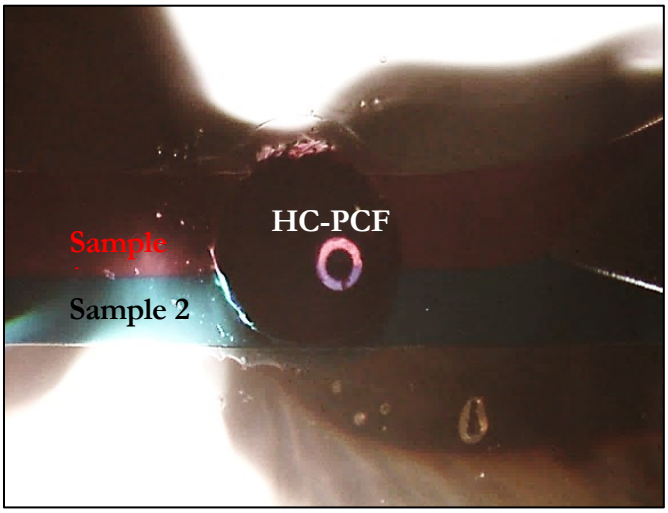

Figure 7-2 Parallel sensing using HC-PCF

7.2.3 Single molecule detection and optimizing SERS

As discussed in Chapter 2, significant advances have been made in the use of SERS over the past 35 years. Single molecule SERS (SMSERS) has been applied to some biomolecules, and researchers find its potential to compete with fluorescence very interesting. SMSERS has significant advantages over single molecule fluorescence, due to particular to decreased sample bleaching and richer, fingerprint-like chemical information [168]. There is also substantial research in enhancing SERS with Resonant Raman by using tunable lasers, and tuning the properties of the nanoparticles [169]. Investigation of new plasmonic materials, such as graphene semiconductors, is another promising area [170-172].

The extent of SERS enhancement is due to a variety of factors, including nanoparticle size, shape, material and configuration [173]. Optimum nanoparticle size and volume ratio for enhancing SERS signals in HC-PCF was discussed in Chapter 5. However, the impact of the shape of nanoparticles in HC-PCF with SERS enhancement has not yet been studied. The optical properties of nanoparticles are tunable throughout the visible and near-infrared spectral regions, as a function of shape and local environment [174]. A wide variety of silver nanoparticle shapes, such as spherical, rod, cube, triangular, hexagonal and many others, have been studied in cuvette [175]. Future work can focus on understanding the full potential of nanoparticles to obtain maximum enhancement of SERS signals in HC-PCF for biosensing applications. For example, different kinds of nanoparticles with various morphologies can be prepared with seed-mediated techniques, to study enhancement of SERS signals in HC-PCF compared to cuvette [176].

7.2.4 Ultrafast nonlinear spectroscopy in HC-PCF for sensing applications

This thesis demonstrates that many HC-PCF applications exploit the possibility of filling the hollow micron size HC-PCF core, in order to create strong interaction between the laser light and the sample analyte. The possibility of controlling the nonlinearity in HC-PCF by simply changing the pressure or creating well-defined

pressure profiles of the liquid, gives it a unique position with regard to coherent sample-laser interaction. Indeed, it has been reported that changing the pressure can create an optimal condition for efficiently generating anti-Stokes waves, and coherently shift the pump laser to higher frequencies [177]. The generation of anti-Stokes components is significant, as it not only coherently shifts the spectrum of the pump to the blue side of the spectral region, but also provides a mechanism for optically cooling the system [178-179].

Efficient generation of anti-Stokes components is of great interest for CARS spectroscopy. However, signals generated in CARS are typically weak. HC-PCF could potentially provide new ways to increase the efficiency of this powerful spectroscopic technique. Although efficient generation of anti-Stokes components in early experiments was attributed to phase-locking the anti-Stokes field to the pump, the possibility of phase matching via the dispersion properties of HC-PCF is a new and promising means of achieving this, and it should be studied in more detail [180].

Recently, femtosecond laser pulses were used to generate SRS from organic liquids, and to demonstrate spectroscopy in the terahertz (THZ) region. This allows investigation of various phenomena, such as hydrogen-bond dynamics in ionic liquids [181]. The great intensity in the HC-PCF core eliminates the need to use high power and high energy lasers to study stimulated Raman scattering (SRS). HC-PCF significantly reduces the complications of self-phase modulation, self-focusing, spectral broadening and continuum generation arising due to high peak power and ultrashort pules. Moreover, the long interaction length between the laser and the sample analyte results in photon conversion efficiencies of more than 90%. To date, no attempts at nonlinear spectroscopy have used femtosecond lasers in conjunction with HC-PCF, and future work could accomplish this.

References

1. S. Krishnan and R. K. Shankar, “Raman Effect: History of the Discovery,” *J. Raman Spectrosc.*, 10, 1-8 (1981).

2. J. Motz, M. Fitzmaurice, A. Miller, S. Gandhi, A. Haka, L. Galindo, R. R. Dasari, J. Kramer, and M. Feld, “In vivo Raman spectral pathology of human therosclerosis and vulnerable plaque,” *J. Biomed. Opt.*, 11, 021003-9 (2006).

3. D. Long, “The Raman Effect: a unified treatment of the theory of Raman scattering by molecules,” *New York: John Wiley and Sons* (2002).

4. R. McCreery, “Raman spectroscopy for chemical analysis,” *New York: John Wiley and Sons* (2000).

5. E. Hanlon, R. Manoharan, T. Koo, K. Shafer, J.T. Motz, M. Fitzmaurice, J. Kramer, I. Itzkan, R. Dasari and M. Feld, “Prospects for in vivo Raman spectroscopy,” *Phys. Med. Biol.,* 45, R1-R59 (2000).

6. P. Taylor, O. Vinn, A. Kudryavtsev, and J. Schopf, “Raman spectroscopic study of the mineral composition of cirratulid tubes (Annelida, Polychaeta),” *J. Struct. Biol.*, 171, 402-405 (2010).

7. K. Kneipp, H. Kneipp, I. Itzkan, R. Dasari, and M. Feld, “Surface-enhanced Raman scattering and biophysics,” *J. Phys. Condens. Matter.*, 14, R597-R624 (2002).

8. B. Chen, “Raman spectroscopy studies of carbon nanotube-polymer composites,” *Dekker Encyclopedia of Nanoscience and Nanotechnology*, (2004).

9. L. Choo-Smith, H. Edwards, H. Endtz, J. Kros, F. Heule, H. Barr, J. Robinson, Jr., H. Bruining, and G. Puppels, “Medical applications of Raman spectroscopy: from proof of principal to clinical implementation,” *Biopolymers*, 67, 1-9 (2002).

10. A. Paudel, D. Raijada, and J. Rantanen, “Raman spectroscopy in pharmaceutical product design,” *Adv. Drug Deliv. Rev.,* 89, 3-20 (2015).

11. U. Neugebauer, P. Rösch, and J. Popp, “Raman spectroscopy towards clinical application: drug monitoring and pathogen identification*,” Int. J. Antimicrob*., 46, S35-S39 (2015).

12. K. Birmingham and G. Kenyon, “Bioterrorism threat becomes reality,” *Nature,* 71, 1167-1167 (2001).

13. O. Stevens, I. Petterson, J. Day, and N. Stone, “Developing fibre optic Raman probes for applications in clinical spectroscopy,” *Chem. Soc. Rev.,* 45, 1919-1934 (2016).

14. T. Frosch, D. Yan, and J. Popp, J., “Ultrasensitive fiber enhanced UV resonance Raman sensing of drugs,” *Anal. Chem.,* 85, 6264-6271 (2013).

15. H. Butler, L. Ashton, B. Bird, G. Cinque, K. Curtis, J. Dorney, K. Esmonde-White, N. Fullwood, B. Gardner, P. Martin-Hirsch, and M. Walsh, “Using Raman spectroscopy to characterize biological materials,” *Nat Protoc.,* 11, 664-687 (2016).

16. “The top 10 causes of death", *the world health report* accessed on July 2nd 2015 (2012).

17. J. Ferraro, K. Nakamoto, and C. Brown, “Introductory Raman Spectroscopy”, *2nd edition, Elsevier* (2003).

18. A. Smekal, “Zur quantentheorie der dispersion,” *Naturwiss.,* 11, 873-875 (1923).

19. C. Raman and K. Krishnan, “A new type of secondary radiation,” *Nature*, 121, 501-502 (1928).

20. M.J. Pelletier, “Introduction to Applied Raman Spectroscopy,” *Blackwell Science Ltd, Oxford,* 1-52 (1999).

21. M. Buric, “Gas phase Raman spectroscopy using hollow waveguides,” *Diss. University of Pittsburgh* (2011).

22. M. Buric, K. Chen, J. Falk and S. Woodruff, “Enhanced spontaneous Raman scattering and gas composition analysis using a photonic bandgap fiber,” *Appl. Opt.*, 47, 4255-4261 (2008).

23. R. Altkorn, I. Koev, R. Van Duyne, and M. Litorja, "Low-loss liquid-core optical fiber for low-refractive-index liquids: fabrication, characterization, and application in Raman spectroscopy," *Appl. Opt.*, 36, 8992-8998 (1997).

24. M. Holtz, P. Dasgupta, and G. Zhang. "Small-volume raman spectroscopy with a liquid core waveguide," *Anal. Chem.,* 71, 2934-2938 (1999).

25. A. Zheltikov, “Ultrashort light pulses in hollow waveguides,” *Physics-Uspekhi,* 45, 687 (2002).

26. S. Sensarn, S. Goda, G. Yin, S. Harris, “Molecular modulation in a hollow fiber,” *Opt. Lett.*, 31, 2836-2838 (2006).

27. R. Miles, G. Laufer, G. Bjorklund, “Coherent anti-stokes Raman scattering in a hollow dielectric waveguide,” *Appl. Phys. Lett.,* 30, 417-419 (1977).

28. S. Howdle, K. Stanley, V. Popov, V. Bagratashvili, “Can high-pressure Raman spectroscopy be simplified? A microscale optical-fiber capillary cell for the study of supercritical fluids*,” Appl. Spectrosc.*, 48, 214-218 (1994).

29. F. Benabid, J. Knight, G. Antonopoulos, and P. Russell, “Stimulated Raman scattering in hydrogen-filled hollow-core photonic crystal fiber,” *Science*, 298, 399-402 (2002).

30. B. Saleh, M. Teich, “Fundamentals of Photonics,” *2nd edition Wiley-Interscience* (2007).

31. M. Naji, “Raman Signal Enhancement and CARS Microscopy,” *Diss. University of Ottawa* (2014).

32. P. Russell, “Photonic-crystal fibers,” *J. Lightwave Technol.*, 24, 4729-4749 (2006).

33. Joseph Fraunhofer Award / Robert M. Burley Prize, *Optical Society of America* accessed on July 2nd 2015 (2000).

34. N. Thang, “Stimulated Raman Scattering in Gas Filled Hollow-Core Photonic Crystal Fiber,” *Diss. Max Plack Institute* (2013).

35. F. Cox, A. Argyros, and M. Large, "Liquid-filled hollow core microstructured polymer optical fiber," *Opt. Express*, 14, 4135-4140 (2006).

36. A. Khetani, “Photonic Crystal Fiber as a Biosensor,” *Diss.Univ. Ottawa* (2008).

37. J. Joannopoulos, S. Johnson, J. Winn, R. Meade, “Photonic Crystals, molding the flow of light,” *Princeton* (2008).

38. K. Nielsen, D. Noordegraaf, T. Sørensen, A. Bjarklev and T. Hansen, “Selective filling of Photonic Crystal Fibres,” *J. Opt. A: Pure Appl. Opt.* 7, L13-L20 (2005).

39. Y. Huang, Y. Xu, and A. Yariv, “Fabrication of functional microstructured optical fibers through a selective-filling technique,” *Appl. Phys. Lett.,* 85, 5182–5184 (2004).

40. Y. Zhang, C. Shi, C. Gu, L. Seballos, J. Zhang, “Liquid core photonic crystal fiber sensor based on surface enhanced Raman scattering,” *Appl. Phys. Lett.,* 90,193504 (2007).

41. W. Wang, X. Yin, J. Wu, Y. Geng, X. Tan, Y. Yu, X. Hong, Y. Du, and X. Li, “Realization of All-in-Fiber Liquid-Core Microstructured Optical Fiber,” *IEEE Photon. Technol. Lett*., 28,609-612 (2016).

42. B. Zhang, Y. Lai, W. Yuan, Y. Seah, P. Shum, X. Yu, and H. Wei, “Laser-assisted lateral optical fiber processing for selective infiltration,” *Opt. Express*, 22, 2675-2680 (2014).

43. Y. Hoo, S. Liu, H. L. Ho, and W. Jin, "Fast response microstructured optical fiber methane sensor with multiple side-openings." *IEEE Photon. Technol. Lett*., 22, 296-298 (2010).

44. G. Antonopoulos, F. Benabid, T. Birks, D. Bird, J. Knight and P. Russell “Experimental demonstration of the frequency shift of bandgaps in photonic crystal fibers due to refractive index scaling,” *Opt. Express*, 14, 3000-3006 (2006).

45. NKT Photonics, “Hollow core fibers” accessed on May 12, 2015.

46. COMSOL Multiphysics and Modeling http://www.comsol.com/.

47. K. Esbensen, “An introduction to multivariate data analysis and experimental design,” Multivariate Data Analysis–In Practice, *5th edn. Camo Inc., Oslo* (2004).

48. A. Campion and P. Kambhampati, “Surface-enhanced Raman scattering,” *Chem. Soc. Rev.*, 27, 241-250 (1998).

49. S. Abalde-Cela, P. Aldeanueva-Potel, C. Mateo-Mateo, L. Rodrı´guez-Lorenzo, R. Alvarez-Puebl and L. Liz-Marzan, “Surface-enhanced Raman scattering biomedical applications of plasmonic colloidal particles,” *J. R. Soc. Interface*, 7, S435-S450, (2010).

50. X. Qian and S.Nie, “Single-molecule and single-nanoparticle SERS: from fundamental mechanisms to biomedical applications,” *Chem Soc Rev.,* 37, 912-920, (2008).

51. Y. Oh, S. Park , M. Kang , J. H. Choi, Y. Nam and K. Jeong, “Beyond the SERS: Raman enhancement of small molecules using nanofluidic channels with localized surface plasmon resonance,” *Small,* 7, 184-188 (2011).

52. C. Choi, Z. Xu, H. Wu, G. Liu and B. Cunningham, “Surface–enhanced nano domes,” *Nanotechnology*, 21, 415301-415307 (2010).

53. G. Schatz and R. Van Duyne, “Electromagnetic Mechanism of Surface-Enhanced Raman Spectroscopy,” *Handbook of Vibrational Spectroscopy,* (2006).

54. K. Faulds, R. Littleford, D. Graham, G. Dent, and W. Smith, “Comparison of surface-enhanced resonance Raman scattering from unaggregated and aggregated nanoparticles,” *Anal. Chem.,* 76, 592-598 (2004).

55. C. McHugh, R. Keir, D. Graham, and W. Smith, “Selective functionalisation of TNT for sensitive detection by SERRS,” *Chem. Commun.,* 6, 580-581 (2002).

56. G. McNay, D. Eustace, W. Smith, K. Faulds, and D. Graham, “Surface-enhanced Raman scattering (SERS) and surface-enhanced resonance Raman scattering (SERRS): a review of applications,” *Appl. Spectrosc.,* 65, 825-837 (2011).

57. D. Graham, and R. Goodacre, “Chemical and bioanalytical applications of surface enhanced Raman scattering spectroscopy,” *Chem. Soc. Rev.,* 37, 883-884 (2008).

58. B. Sharma, R. Frontiera, A-I. Henry, E. Ringe, and R. Van Duyne, “SERS: Materials, applications, and the future,” *Mater. Today,* 15, 16-25 (2012).

59. D. Li, S. Feng, H. Huang, W. Chen, H. Shi, N. Liu, L. Chen, W. Chen, Y. Yu, and R. Chen, “Label-free detection of blood plasma using silver nanoparticle based surface-enhanced Raman spectroscopy for esophageal cancer screening,” *J Biomed Nanotechnol.,* 10, 478-484 (2014).

60. C. Girish, S. Iyer, K. Thankappan, V. Rani, G. Gowd, D. Menon D, S. Nair, and M. Koyakutty, “Rapid detection of oral cancer using Ag-TiO2 nanostructured surface-enhanced Raman spectroscopic substrates,” *J. Mater. Chem. B*, 2, 989-98 (2014).

61. W. Pearman, and A. Fountain, “Classification of chemical and biological warfare agent simulants by surface-enhanced Raman spectroscopy and multivariate statistical techniques,” *Appl Spectrosc*., 60, 356-65 (2006).

62. J. Granger, N. Schlotter, A. Crawford, and M. Porter, "Prospects for point-of-care pathogen diagnostics using surface-enhanced Raman scattering (SERS)," *Chem. Soc. Rev.,* 45, 3865-3882 (2016).

63. H. Zhou, D. Yang, N. Ivleva, N. Mircescu, R. Niessner, and C. Haisch, “SERS detection of bacteria in water by in situ coating with Ag nanoparticles,” *Anal. Chem.,* 86, 1525-1533 (2014).

64. D. Cowcher, Y. Xu, and R. Goodacre, “Portable, Quantitative Detection of Bacillus Bacterial Spores Using Surface-Enhanced Raman Scattering,” *Anal. Chem.,* 85, 3297-3302 (2013).

65. K. Kneipp, Y. Wang, H. Kneipp, L. Perelman, I. Itzkan, R. Dasari, and M. Feld, “Single Molecule Detection Using Surface-Enhanced Raman Scattering (SERS),” *Phys. Rev. Lett.,* 78, 1667-70 (1997).

66. H. Xu, E. Bjerneld, M. Käll, and L. Börjesson, “Spectroscopy of Single Hemoglobin Molecules by Surface Enhanced Raman Scattering,” *Phys. Rev. Lett.*, 83, 4357-60 (1999).

67. H. Chen, J. Luo, T. Zeng, L. Jiang, Y. Sun, Z. Jiao, Y. Jin, and X. Sun, “Investigation of the synthesis, SERS performance and application in glucose sensing of hierarchical 3D silver nanostructures,” *New J. Chem.,* 38, 3907-16 (2014).

68. Y. Huh, A. Chung, and D. Erickson, “Surface enhanced Raman spectroscopy and its application to molecular and cellular analysis,” *Microfluid Nanofluid*., 6, 285-97 (2009).

69. M. Fleischman, P. Hendra, and A. McQuillan, "Raman spectra of pyridine adsorbed at a silver electrode." *Chem. Phys. Lett.,* 26, 163-166 (1974)

70. D. Jeanmaire, and R. Van Duyne, "Surface Raman spectroelectrochemistry: Part I. Heterocyclic, aromatic, and aliphatic amines adsorbed on the anodized silver electrode." *J. Electro anal, Chem.,* 84, 1-20. (1977).

71. M.G. Albrecht, and J.A. Creighton, "Anomalously intense Raman spectra of pyridine at a silver electrode." *J. Am. Chem. Soc.*, 99, 5215-5217 (1977).

72. J. Sanchez-Gil, J. Garcia-Ramos, and E. Mendez, "Electromagnetic mechanism in surface-enhanced Raman scattering from Gaussian-

correlated randomly rough metal substrates," *Opt. Express*, 10, 879-886 (2002).

73. A. Sadrolhosseini, A. Noor, and M. Moksin, “Application of surface plasmon resonance based on a metal nanoparticle,” *Kim KY, Plsmonics-Principles and Applications,* 253-282 (2012).

74. M. Stewart, C. Anderton, L. Thompson, J. Maria, S. Gray, J. Rogers, and R. Nuzzo “Nanostructured Plasmonic Sensors”, *Chem. Rev.,* 108, 494-521 (2008).

75. S. Morton, and L. Jensen, “Understanding the Molecule− Surface Chemical Coupling in SERS,” *J. Am. Chem. Soc.,* 131, 4090-4098 (2009).

76. N. Israelsen, C. Hanson, and E. Vargis, “Nanoparticle Properties and Synthesis Effects on Surface-Enhanced Raman Scattering Enhancement Factor: an introduction,” *The Scientific World Journal* (2015).

77. L. Jensen, C. Aikens, and G. Schatz, “Electronic structure methods for studying surface enhanced Raman scattering,” *Chem. Soc. Rev.,* 37, 1061–1073 (2008).

78. A. Pinto, and M. Lopez-Amo, “Photonic crystal fibers for sensing applications,” *Journal of Sensors*, 598178 (2012).

79. H. Yan, C. Gu, C. Yang, J. Liu, G. Jin, J. Zhang, L. Hou, and Y. Yao, “Hollow core photonic crystal fiber surface-enhanced Raman probe,” *Appl. Phys. Lett.,* 89, 204101 (2006).

80. X. Yang, T. Bond, J. Zhang, Y. Li, and C. Gu, “Photonics crystal fiber Raman sensors,” *Proc. SPIE,* 8559 (2012).

81. C. Shi, C. Lu, C. Gu, L. Tian, R. Newhouse, S. Chen, and J. Zhang, “Inner wall coated hollow core waveguide sensor based on double substrate surface enhanced Raman scattering,” *Appl. Phys. Lett.*, 93, 153101 (2008).

82. Y. Han, S. Tan, M. Oo, D. Pristinski, S. Sukhishvili, and H. Du, “Towards Full-Length Accumulative Surface-Enhanced Raman Scattering-Active Photonic Crystal Fibers,” *Adv. Mater.,* 22, 2647-51 (2010).

83. J. Irizar, J. Dinglasan, J. Goh, A. Khetani, H. Anis, D.Anderson, C. Goh, A. Helmy, “Raman Spectroscopy of Nanoparticles Using Hollow-Core Photonic Crystal Fibers,” *IEEE J. Sel. Topics Quantum Electron.*, 14, 1214-22 (2008).

84. X. Yang, C. Shi, R. Newhouse, J. Zhang, and C. Gu, “Hollow-Core Photonic Crystal Fibers for Surface-Enhanced Raman Scattering Probes,” *Int. J. Opt.,* 2011:11 (2011).

85. F. M. Cox, A. Argyros, and M. C. J. Large, "Liquid-filled hollow core microstructured polymer optical fiber," *Opt. Express*, 14, 4135-4140 (2006).

86. U. Dinish, G. Balasundaram, Y. Chang, and M. Olivo, “Sensitive multiplex detection of serological liver cancer biomarkers using SERS-active photonic crystal fiber probe,” *J. Biophotonics*., 7, 956-965 (2014).

87. M. Calcerrada, C. García-Ruiz, and M. González-Herráez, "Chemical and biochemical sensing applications of microstructured optical fiber-based systems," *Laser Photon. Rev.*, 9, 604-627 (2015).

88. T. Gong, Y. Cui, D. Goh, K. Voon, P. Shum, G. Humbert, J. Auguste, X. Dinh, K. Yong, and M. Olivo, “Highly sensitive SERS detection and quantification of sialic acid on single cell using photonic-crystal fiber with gold nanoparticles,” *Biosens. Bioelectron*, 64, 227-233 (2015).

89. J. Mammone, S. Sharma, and M. Nicol, “Raman spectra of methanol and ethanol at pressures up to 100 kbar*,” J. Phys. Chem.,* 84, 3130-3134 (1980).

90. F. Eftekhari, J. Irizar, L. Hulbert, and A. Helmy, “A comparative study of Raman enhancement in capillaries,” *J. Appl. Phys.*, 109, 113104 (2011).

91. M. Midrio, M. Singh, and C. Someda, “The space filling mode of holey fibers: an analytical vectorial solution” *J. Lightwave Technol.,* 18, 10311037 (2000).

92. S. Pilotto, M. Pacheco, L. Silveira Jr, A. Villaverde, and R. Zangaro, “Analysis of near-infrared Raman spectroscopy as a new technique for a transcutaneous non-invasive diagnosis of blood components,” *Lasers Med. Sci.,* 16, 2-9 (2001).

93. D. Qi, and A. Berger, “Chemical concentration measurement in blood serum and urine samples using liquid-core optical fiber Raman spectroscopy,” *Appl. Opt.,* 46, 1726-1734 (2007).

94. R. Berg, “Investigation of L (+)-Ascorbic acid with Raman spectroscopy in visible and UV light,” *Appl. Spectrosc. Rev.,* 50, 193-239 (2015).

95. A. Monfared, V. Tiwari, M. Tripathi, and H. Anis, “Raman spectroscopy for clinical-level detection of heparin in serum by partial least-squares analysis,” *J. Biomed. Opt.,* 18, 027010-027010 (2013).

96. S. Spinler, A. Wittkowsky, E. Nutescu, and M. Smythe, “Anticoagulation Monitoring Part 2: Unfractionated Heparin and Low-Molecular-Weight Heparin”, *Ann. Pharmacother.*, 39, 1275-1285 (2005).

97. F. Newall, "Anti-factor Xa (Anti-Xa) Assay." *Haemostasis. Method and Protocols, Springer*, 265-272 (2013).

98. M. Smythe, J. Koerber, S. Westley, S. Nowak, R. Begle, M. Balasubramaniam, and J. Mattson, “Use of the activated partial thromboplastin time for heparin monitoring,” *Am. J. Clin. Pathol.,* 115, 148-155 (2001).

99. M. Makris, R. Hough, and S. Kitchen, “Poor reversal of low molecular weight heparin by protamine,” *Br. J. Haematol.,* 108: 884–885 (2000).

100. Y. Nose, “Hemodialysis patients deaths in the USA by contaminant suspected heparin originating from China”, *Artif. Organs,* 32, 425-426 (2008).

101. H. Szelke, J. Harenberg, and R. Krämer, “Detection and neutralisation of heparin by a fluorescent ruthenium compound”, *Thromb. Haemost.,* 102, 859–864 (2009).

102. U. Warttinger, C. Giese, J. Harenberg, E. Holmer, and R. Krämer, “A fluorescent probe assay (Heparin Red) for direct detection of heparins in human plasma,” *Anal. Bioanal. Chem.,* 1-11 (2016).

103. K. Gaus and E. Hall, “Evaluation of Surface Plasmon Resonance (SPR) for Heparin Assay”, *J. Colloid Interface Sci.,* 194, 364–372 (1997).

104. N. Milovic, J. Behr, M. Godin, C. Hou, K.Payer, A. Chandrasekaran, P.Russo, R. Sasisekharan, and S. Manalis, “Monitoring of heparin and its low-molecular-weight analogs by silicon field effect”, *Proc. Natl. Acad. Sci. U S A*, 103, 13374-13379 (2006).

105. N. Ramamurthy, N. Baliga, J. Wahr, U. Schaller, V. Yang, and M. Meyerhoff, “Improved protamine-sensitive membrane electrode for monitoring heparin concentrations in whole blood via protamine titration,” *Clin. Chem.,* 44, 606-613 (1998).

106. J. Wang, F. Chen, S. Arconada-Alvarez, J. Hartanto, L. Yap, R. Park, F. Wang, I. Vorobyova, G. Dagliyan, P. Conti, and J. Jokerst, “A Nanoscale Tool for Photoacoustic-based Measurements of Clotting Time and Therapeutic Drug Monitoring of Heparin,” Nano Lett. 16, 6265–6271 (2016).

107. M. Naji, A. Khetani, N. Lagali, R. Munger and H. Anis, “A novel method of using hollow-core photonic crystal fiber as a Raman biosensor”, *Proc. SPIE*, 6865, 68650E-1 (2008).

108. A. Khetani, M. Laferrière, H. Anis and J. C. Scaiano, “Laser flash photolysis with nanoliter samples: photonic crystal fibers as ultrasmall smart test tubes”, *J. Mater. Chem.,* 18, 4769–4774 (2008).

109. D. Atha, A. Gaigalas, and V. Reipa, “Structural analysis of heparin by Raman spectroscopy”, *J. Pharm. Sci.,* 85, 52–56 (1996).

110. Food and Drug Administration, “International conference on harmonisation. Guideline on validation of analytical procedures: definitions and terminology,” *Federal Register,* 60, 11259–11262 (1995).

111. Y.Shevchenko, “Chemical and Biological Sensing with a Fiber Optic Surface Plasmon Resonance Device,” *Diss., Carleton University* (2013)..

112. C. Herrmann, C. Vrancic, A. Fomichova, N. Gretz, S. Hoecker, A. Pucci, and W. Petrich, “In vitro characteristics of a mid-infrared continuous glucose sensor”, *Proc. SPIE*, 7560, 75600E (2010).

113. J. Riordon, M. Mirzaei, and M. Godin, “Microfluidic cell volume sensor with tunable sensitivity,” *Lab Chip* 12, 3016–3019 (2012).

114. C. Schaschke “Fluid Mechanics: Worked Example for Engineers Chapter 3” *Rugby, Warwickshire, UK: IChemE* (2005).

115. G. Kaye, T. Laby, “Viscosities Tables of physical and chemical constants Chapter 2” *Harlow, Essex: Longman* 1999.

116. C. McGoverin, A. Clark, S. Holroyd, and K. Gordon, “Raman spectroscopic quantification of milk powder constituents,” *Anal. Chim. Acta.* 673, 26-32 (2010).

117. D. Johnston, P. Scanlon, D. Hodge, R. Glynn, J. Hung, and R. Gibbons, "Pulmonary function monitoring during adenosine myocardial perfusion scintigraphy in patients with chronic obstructive pulmonary disease," *Mayo Clinic Proc.,* 74, 339 (1999).

118. J. Chen, X. Liu, K. Feng, Y. Liang, J. Jiang, G. Shen, R. Yu, "Detection of adenosine using surface enhanced Raman scattering based on structure-switching signaling aptamer," *Biosens. Bioelectron*., 24, 66 (2008).

119. A. Khetani, V. S. Tiwari, A. Harb and H. Anis, “Monitoring of heparin concentration in serum by Raman spectroscopy within hollow core photonic crystal fiber,” *Opt. Exp.,* 19, 15244-15254, (2011).

120. A. Khetani, M. Naji, N. Lagali, R. Munger, and H. Anis, “A method for using Photonic Crystal Fiber as a Raman biosensor,” *US Patent*, 2010/0014077 (2010).

121. K. G. Stamplecoskie, J. C. Scaiano, V. S. Tiwari and H. Anis, “Optimal size of silver nanoparticles for surface enhanced Raman spectroscopy,” *J. Phys. Chem. C,* 115, 1403-1409 (2011).

122. P.Hildebrandt, and M. Stockburger, “Surface-enhanced resonance Raman spectroscopy of rhodamine 6G adsorbed on colloidal silver,” *J. Phys. Chem.,* 88, 5935-5944 (1984).

123. M. Meier and A. Wokaun, “Enhanced fields on large metal particles:dynamic depolarization,” *Opt. Lett.,* 89, 581-583, (1983).

124. A. Wokaun, J. Gordon and P. Liao, “Radiation damping in surface-enhanced Raman scattering,” *Phys. Rev. Lett.,* 48, 957-960, (1982).

125. Y. Zhang, C. Gu, A. Schwartzberg, S. Chen, and J. Zhang, “Optical trapping and light-induced agglomeration of gold nanoparticles aggregates,” *Phys. Rev. B,* 73, 165405 1-9 (2006).

126. P. Lee, and D. Meisel, “Adsorption and surface-enhanced Raman of dyes on silver and gold sols,” *J. Phys. Chem.,* 86, 3391-3395 (1982).

127. S. Sanches-Cortes and J. V. Garcia-Ramos, “Surface-enhanced Raman spectroscopy of adenosine and 5'AMP: evolution in time,” *Proc. SPIE,* 1403, 142-145 (1991).

128. P. Huang and J. Liu, “Flow Cytometry-Assisted Detection of Adenosine in Serum with an Immobilized Aptamer Sensor”, *Anal. Chem.,* 82, 4020-4026 (2010).

129. L. Li, P. Ge, P. Selvin, and Y. Lu, “Direct Detection of Adenosine in Undiluted Serum Using a Luminescent Aptamer Sensor Attached to a Terbium Complex” *Anal. Chem.,* 84, 7852-7856 (2012).

130. R. Marin, K. Franchini, and S. Rocco, “Analysis of adenosine by RP-HPLC method and its application to the study of adenosine kinase kinetics”, *J. Sep. Sci.,* 30, 2473-2479 (2007).

131. D. Graham, D. Salzberg, J. Kurtzberg, S. Sather, G. Matsushima, A. Keating, L. X. Liang, M. Lovell, S. Williams, T. Dawson, M. Schell, A. Anwar, H. Snodgrass, and H. Earp, “Ectopic expression of the proto-oncogene Mer in pediatric T-cell acute lymphoblastic leukemia,” *Clin. Cancer Res.,* 12, 2662-2669 (2006).

132. K. Zhang, T. Tan, J. Fu, T. Zheng, and J. Zhu, “A novel aptamer-based competition strategy for ultrasensitive electrochemical detection of leukemia cells,” *Analyst*, 138, 6323-6330 (2013).

133. C. Brown, S. Larsen, H. Iland, D. Joshua and J. Gibson, “Leukaemias into the 21st century: part 1: the acute leukaemias,” *Intern. Med. J,* 42, 1179-1186 (2012).

134. Z. Darzynkiewicz, and H. Zhao, “Cell cycle analysis by flow cytometry,” *eLS* (2014).

135. H. Goh, M. Lin, T. Fukushima, G. Saglio, D. Kim, S. Choi, , S. Kim, J. Lee, Y. Lee, S. Oh and D. Kim, “Sensitive quantitation of minimal residual disease in chronic myeloid leukemia using nanofluidic digital polymerase chain reaction assay,” *Leuk. Lymphoma.,* 52, 896-904 (2011).

136. R. Olsen, H. Jennifer, and E. Aamir, "Acute leukemia immunohistochemistry: a systematic diagnostic approach," *Arch. Pathol. Lab. Med.,* 132, 462 (2008).

137. C. Righeschi, E. Tolga, K. Anastasia, B. Anna, and E. Thomas , "Microarray-based mRNA expression profiling of leukemia cells treated with the flavonoid, casticin," *Cancer Genomics-Proteomics*., 9, 143-151 (2012).

138. R. Li, Y. Tan, X. Chen, F. Ren, Y. Zhang, Z. Xu, and H. Wang, “Fluorescence probe analysis of leukemia cells by modified graphene oxide,” *Carbon,* 85, 446 (2015) .

139. T. Shimizu, and Y. Pommier, “Camptothecin-induced apoptosis in p53-null human leukemia HL60 cells and their isolated nuclei: effects of the protease inhibitors Z-VAD-fmk and dichloroisocoumarin suggest an involvement of both caspases and serine proteases,” *Leukemia*., 11 1238-1244 (1997).

140. M. Gupta, A. Fujimori, and Y. Pommier, “Eukaryotic DNA topoisomerases I,” *BBA-Gene Struct. Expr.*, 1262, 1-14 (1995).

141. Y. Pommier, “Eukaryotic DNA topoisomerase I: genome gatekeeper and its intruders, camptothecins,” *Semin Oncol.*, 23 3-10 (1996).

142. Y. Oshima, H. Shinzawa, T. Takenaka, C. Furihata, , and H. Sato, “Discrimination analysis of human lung cancer cells associated with histological type and malignancy using Raman spectroscopy,” *J. Bio. Opt.,* 15, 017009-017009 (2010).

143. W. Kaiser and C. Garrett, “Two-Photon Excitation in CaF2:Eu2+,” *Phys. Rev. Lett.,* 7, 229-231 (1961).

144. P. Franken, A. Hill, C. W. Peters, and G. Weinreich, “Generation of Optical Harmonics,” *Phys. Rev. Lett.,* 7, pp. 118-119 (1961).

145. G. Eckhardt, R. Hellwarth, F. McClung, S. Schwarz, D. Weiner, and E. Woodbury, “Stimulated Raman Scattering From Organic Liquids,” *Phys. Rev. Lett.,* 9, 455-457 (1962).

146. V. Bredikhin, M. Galanin, and V. Genkin, “Two-photon absorption and Spectroscopy,” *Sov. Phys.-Usp.* 16, 299-321 (1973).

147. D. Friedrich and W. McClain, “Two-Photon Molecular Electronic Spectroscopy,” *Annu. Rev. Phys. Chem.* 31, 559-577 (1980).

148. P. Callis, “Two-Photon-Induced Fluorescence,” *Ann. Rev. Phys. Chem.* 48, 271-297 (1997).

149. R. Boyd, “Nonlinear Optics,” *Academic Press, New York* (1992).

150. M. Rasmusson, A. N. Tarnovsky, E. Åkesson, and V. Sundström, “On the Use of Two-Photon Absorption for Determination of Femtosecondcond

Pump-Probe Cross- Correlation Functions," *Chem. Phys. Lett.* 335, 201-208 (2001).

151. I. Cormack, W. Sibbett, and D. Reid, "Practical measurement of femtosecond optical pulses using time-resolved optical gating," *Opt. Commun.*, 194, 415-424 (2001).

152. G. He, R. Signorini, and P. Prasad, "Two-Photon-Pumped Frequency-Upconverted Blue Lasing in Coumarin dye solution," *Appl. Opt.,* 37, 5720-5726 (1998).

153. W. Denk, J. Strickler, and W. Webb, "Two-photon laser scanning fluorescence microscopy," *Science,* 248, 73-76 (1990).

154. A. Dvornikov, C. Taylor, Y. Liang, and P. Rentzepis, "Photorearrangement mechanism of 1-nitro-naphthaldehyde and application to three-dimensional optical storage devices," *J. Photochem. Photobiol.*, 112, 39-46 (1998).

155. S. Maruo and S. Kawata, "Two-Photon-Absorbed Near-Infrared Photopolymerization for Three-Dimensional Microfabrication*," J. Microelectromech. Syst.* 7, 411-415 (1998).

156. C. Spangler, "Recent development in the design of organic materials for optical power limiting," *J. Mater. Chem.*, 9, 2013-2020 (1999).

157. J. Liu, Y. Zhao, J. Zhao, A. Xia, L. Jiang, S. Wu, L. Ma, Y. Dong, and Y. Gu, "Two-Photon Excitation Studies of Hypocrellins for Photodynamic Therapy," J*. Photoch. Photob. B: Biol.* 68, 156-164 (2002).

158. P. K. Frederiksen and O. P. R. Jørgensen, "Two-Photon Photosensitized Production of Singlet Oxygen," *J. Am. Chem. Soc.* 123, 1215-1221 (2001).

159. G. Williams, J. Chen, T. Euser, P. Russell, and A. Jones, “Photonic crystal fibre as an optofluidic reactor for the measurement of photochemical kinetics with sub-picomole sensitivity,” *Lab Chip*, 12, 3356-3361 (2012).

160. A. Cubillas, S. Unterkofler, T. Euser, B. Etzold, A. Jones, P. Sadler, W. Peter and P. Russell, “Photonic crystal fibres for chemical sensing and photochemistry,” *Chem. Soc. Rev.,* 42, 8629-8648 (2013).

161. H. Stawska, and E. Bereś-Pawlik, “Enhancement of two photon fluorescence collection by using effectively single mode double clad hollow core fiber with low dispersion at 800 nm” *Opt. Quan Electron.,* 47, 67-76 (2015).

162. G. Williams, T. Euser, J. Arlt, P. Russell, and A. Jones, “Taking Two-Photon Excitation to Exceptional Path-Lengths in Photonic Crystal Fiber,” *ACS Photonics* 1, 790-793 (2014).

163. I. Agranat, A. Barak, and M. Pick, “Fulvenes and thermochromic ethylenes. 80. Di (phenyl-d5) cyclopropenone,” *J. Org. Chem.,* 38, 3064-3065 (1973).

164. C. Weidner, D. Wadsworth, C. Knop, A. Oyefesso, B. Hafer, R. Hartman, R. Mehlenbacher, and S. Hogan, S.; Convenient and general synthesis of 2-alkoxy-3-arylcyclopropenones,” *J. Org. Chem.,* 1994, 59, 4319-4322.

165. A. Poloukhtine, and V. Popik, “Highly Efficient Photochemical Gen-eration of a Triple Bond: Synthesis, Properties, and Photodecar-bonylation of Cyclopropenones,” *J. Org. Chem.,* 68, 7833-7840 (2013).

166. N. Urdabayev, A. Poloukhtine, and V. Popik, “Two-photon induced photodecarbonylation reaction of cyclopropenones,” *Chem. Commun.,* 4, 454-456 (2006).

167. M. Stich, L. Fischer, and O. Wolfbeis, “Multiple fluorescent chemical sensing and imaging,” *Chem. Soc. Rev.,* 39, 3102-3114 (2010).

168. P. Etchegoin, and E. Le Ru, “A perspective on single molecule SERS: current status and future challenges,” *Phys. Chem. Chem. Phys.*, 10, 6079-6089 (2008).

169. S. Basu, S. Jana, S. Pande, and T. Pal, “Interaction of DNA bases with silver nanoparticles: assembly quantified through SPRS and SERS,” *J. Colloid Interface Sci.*, 321, 288-293 (2008).

170. M. Harper, K. McKeating, and K. Faulds, “Recent developments and future directions in SERS for bioanalysis,” *Phys. Chem. Chem. Phys.*, 15, 5312-5328 (2013).

171. W. Xu, N. Mao, and J. Zhang, “Graphene: A Platform for Surface-Enhanced Raman Spectroscopy,” *Small,* 9, 1206-1224 (2013).

172. X. Wang, W. Shi, G. She, and L. Mu, “Surface-enhanced Raman scattering (SERS) on transition metal and semiconductor nanostructures,” *Phys. Chem. Chem. Phys.*, 14(17), 5891-5901 (2012).

173. N. Israelsen, C. Hanson, and E. Vargis, “Nanoparticle Properties and Synthesis Effects on Surface-Enhanced Raman Scattering Enhancement Factor: An Introduction,” *Scientific World J.* 124582 (2015).

174. Radha Narayanan, “Nanoparticles of Different Shapes for Biosensor Applications in Functional Nanoparticles for Bioanalysis, Nanomedicine, and Bioelectronic Devices” *ACS Symposium Series*, 1, 281-292 (2012).

175. B. Khodashenasa, H. Ghorbanib, “Synthesis of silver nanoparticles with different shapes*”, Arabian J. Chem.* (2015).

176. V. Tiwari, T. Oleg, G. Darbha, W. Hardy, J. Singh, P. Ray, “Non-resonance SERS Effects of Silver Colloids with Different Shapes,” *Chem. Phys. Lett.,* 446, 77 (2007)

177. B. Trabold, A. Abdolvand, T. Euser, and P. Russell, "Efficient anti-Stokes generation via intermodal stimulated Raman scattering in gas-filled hollow-core PCF," *Opt. Express*, 21, 29711-29718 (2013).

178. A. Goncharov, “Raman Spectroscopy at High Pressures,” *Spectrosc. Int. J.,* 617528, 16 (2012).

179. A. Nazarkin, A. Abdolvand, and P. Russell, “Raman amplifiers without quantum-defect heating,” *European Conference and Exhibition on Optical Communication (ECOC),* Tu.4.E.4, 1-3 (2010).

180. M. Ziemienczuk, A. Walser, A. Abdolvand, A. Nazarkin, C. Kaminski, and P.Russell, “Three-wave stimulated Raman scattering in hydrogen-filled photonic crystal fiber,” *CLEO,* CD8.1 (2011).

181. P. Russell, P. Hölzer, W. Chang, A. Abdolvand, and J. Travers, “Hollow-core photonic crystal fibres for gas-based nonlinear optics,” *Nat. Photonics,* 8, 278-286 (2014).

182. C. Saatkamp, M. de Almeida, J. Bispo, A. Pinheiro, A. Fernandes, and L. Silveira, “Quantifying creatinine and urea in human urine through Raman spectroscopy aiming at diagnosis of kidney disease,” *J. Biomed. Opt.,* 21, 037001-037001 (2016).